Investigation of Particle Trajectories for Wall Bounded Turbulent Two-Phase Flows

Nicholas D. Cardwell

Dissertation submitted to the Faculty of
Virginia Polytechnic Institute and State University
in partial fulfillment of the requirements for the degree of

Doctor of Philosophy
in
Mechanical Engineering

Karen A. Thole, Co-Advisor
Pavlos P. Vlachos, Co-Advisor
Clinton L. Dancey
Thomas E. Diller
Roger L. Simpson

April 2, 2010
Blacksburg, Virginia

Keywords: Multi-Phase Flows, Gas Turbines, Internal Cooling, Particle Tracking Velocimetry

Investigation of Particle Trajectories for Wall Bounded Turbulent Two-Phase Flows

Nicholas D. Cardwell

Abstract

The analysis of turbulent flows provides a unique scientific challenge whose solution remains central to unraveling the fundamental nature of all fluid dynamics. Measuring and predicting turbulent flows becomes even more difficult when considering a two-phase flow, which is a commonly encountered engineering problem across many disciplines. One such example, the ingestion of foreign debris into a gas turbine engine, provided the impetus for this study. Despite more than 40 years of research, operation with a particle-laden inlet flow remains a significant problem for modern turbomachines. The purpose, therefore, is to develop experimental methods for investigating multi-phase flows relevant to the cooling of gas turbine components.

Initially, several generic components representing turbine cooling designs were evaluated with a particle-laden flow using a special high temperature test facility. The results of this investigation revealed that blockage was highly sensitive to the carrier flowfield as defined by the cooling geometry. A second group of experiments were conducted in one commonly used cooling design using a Time Resolved Digital Particle Image Velocimetry (TRDPIV) system that directly investigated both the carrier flowfield and particle trajectories. Traditional PIV processing algorithms, however, were unable to resolve the particle motions of the two-phase flow with sufficient fidelity. To address this issue, a new Particle Tracking Velocimetry (PTV) algorithm was developed and validated for both single-phase and two-phase flows. The newly developed PTV algorithm was shown to outperform other published algorithms as well as possessing a unique ability to handle particle laden two-phase flows.

Overall, this work demonstrates several experimental methods that are well suited for the investigation of wall-bounded turbulent two-phase flows, with a special emphasis on a turbine cooling method. The studies contained herein provide valuable information regarding the previously unknown fluid and particle dynamics within the turbine cooling system.

Preface

The dissertation is organized in a manuscript form that includes four individual research papers documenting the focus and progression of this work. All manuscripts are either currently in press or will be submitted to an appropriate technical journal, as indicated on the first page of each article. The first two works were previously presented at international conferences; the 2008 and 2009 International Gas Turbine Institute (IGTI) Turbo Expo in Berlin, Germany and Orlando, FL, respectively. Paper one and two have also been accepted to the Journal of Turbomachinery and are currently in press.

The first paper investigates the effects of a sand-laden cooling flow with four double-wall cooling liner designs. A TRDPIV study of a particle-laden rib-channel flow is presented in the second paper, with an emphasis on benchmarking the fluid measurements as well as a qualitative treatment of the particle trajectories. The third paper presents an in-depth study of the fluid dynamics of the rib-channel flowfield for multiple Reynolds numbers and channel positions. The fourth paper provides a new PTV methodology that utilizes particle related parameters and displacement conditioning for the tracking of particles. All works were conducted in either the Experimental and Computational Convection Laboratory (ExCCL), under the direction of Dr. Karen Thole, or the Advanced Experimental Thermofluid Engineering Research Laboratory (AEThER), under the direction of Dr. Pavlos Vlachos.

Acknowledgements

My journey through graduate school has truly been blessed and I am eternally grateful to all who have helped me along the way. The culmination of my research, as contained in this dissertation, would not have been possible without everyone's help and the complete expression of my gratitude could never be contained in a single page!

I would like to thank my advisors, Dr. Karen Thole and Dr. Pavlos Vlachos: for molding me into the researcher that I am today. You are the examples of success that I will continually measure myself against. I am very grateful to have known you both and appreciate all that you have done for me. Many thanks to my committee members, Dr. Clint Dancey, Dr. Tom Diller, and Dr. Roger Simpson, who graciously offered their time and support. Although space prohibits me from naming them all, I would like to acknowledge my friends and lab-mates (past and present) from the VT ExCCL, AEThER, and PSU ExCCL. You toiled with me; we shared each other's successes and failures; from late night technical conversations to early morning tailgates – I could not have asked for better compatriots. And to all the staff at Virginia Tech; thank you for making my experience in southwest Virginia richer. I will miss you all.

I'd also like to thank my family for cheering me on and putting up with me living so far from home. Wes, you're an awesome brother and I cherish the time we had at Virginia Tech living together and cheering on the Hokies. Mom, you have always been my greatest advocate and willing to sacrifice anything so I could have the chance to succeed. Who would have thought encouraging me to join the high school engineering team would have taken me so far!

To my beloved Robyn: words cannot express the depth of my gratitude for the love and support you have given to me. Together we have celebrated the highs and endured the lows of graduate student life. Thank you for being the person I had always hoped to find, and for knowing me better than I know myself even from the start. You are the ocean; I am the shore.

Table of Contents

List of Tables

List of Figures

Paper 1: Investigation of Sand Blocking Within Impingement and Film-Cooling Holes

Cardwell, N.D., Thole, K.A., Burd, S.W., 2008, "Considerations of a Double-Wall Cooling Design to Reduce Sand Blockage," International Gas Turbine and Aeroengine Congress and Exposition, Berlin, Germany, ASME Paper GT2008-50160.*

Cardwell, N.D., Thole, K.A., Burd, S.W., 2010, "Investigation of Sand Blocking within Impingement and Film-Cooling Holes," Journal of Turbomachinery, Volume 132, Issue 2, DOI:10.1115/1.3106702.*

Abstract

Gas turbines are not generally designed for operation with a particle laden inlet flow but, in fact, are commonly operated in unclean environments resulting in dirt, sand, and other debris ingestion. In addition to the negative effects within the main gas path, for aeroengines these particles are pulled into the coolant system where they can clog cooling passages and erode internal surfaces.

Unlike previous research that focused on deposition and erosion within the main gas path, this study evaluated blocking in a double wall liner whereby both impingement and film-cooling holes were simulated. Double wall liners are commonly used in the combustor and turbine for combined internal and external cooling of metal components. Specifically, sand blockages were evaluated through comparisons of measured flowrates for a particular pressure ratio across the liner. Four liner geometries were tested whereby the coolant hole size and orientation were varied in test coupons. At ambient temperature, blocking was shown to be a function of the impingement flow area. A significant rise in blocking was observed as sand and metal temperatures were increased. The overlap between the impingement and film-cooling holes was also found to have a significant effect.

*Co-authors: Dr. Karen A. Thole, Mechanical and Nuclear Engineering Department, Penn State
Dr. Steve W. Burd, Pratt and Whitney, East Hartford, CT

Introduction

Figure 1.1 [1] shows two instances of gas turbines operating in dust-laden environments. Complete filtration of the intake air is often deemed infeasible because of the associated pressure drop, filter replacement and cleaning requirements, and overall increase in engine weight. Particle ingestion into a gas turbine can have serious effects on both performance and engine service intervals. While passing through the engine, ingested debris collides with and subsequently erodes the metal surfaces. These particles, which are also pulled into the coolant air bypass, clog the internal channels thereby reducing coolant mass flow and increasing part temperature. Elevated temperatures within the engine can melt the sand, further increasing the likelihood of deposition and blocking within the cooling channels. Two commonly used cooling techniques within a gas turbine are impingement and film-cooling. Impingement cooling is used to cool parts from the inside, as this type of flow would be aerodynamically disruptive within the main gas path. Film-cooling is often employed on the external surface by providing a coolant film along the exterior.

For this study, the combination of impingement and film-cooling holes, often referred to as a double wall liner, was subjected to a sand-laden coolant stream. Measurements of the coolant flow at a given pressure ratio were made to deduce the reduction in flow that would occur in an engine under sand-laden coolant conditions. The following parameters were investigated: liner geometry, pressure ratio, entering sand temperature, sand amount, and metal temperature. This paper also contains a literature review and description of experimental methods in addition to the experimental results performed at both ambient and engine temperatures.

Figure 1.1. Gas turbines operated in dust laden environments. (www.militaryphotos.net, 2007, used under fair use)

Relevant Past Studies

As stated previously, ingestion of foreign particles can adversely affect a turbine's performance and lifecycle. The past studies review begins with previous research focusing on actual incidents of in-service turbine hardware experiencing debris ingestion. It is followed by a review of simulated experimental and computational studies on the effects of particle ingestion relevant to gas turbine applications.

Research Motivation

The most common instances of foreign particle ingestion for a commercial aircraft engine arise from entering a volcanic ash cloud. An early instance of this potentially disastrous situation was on the June 24th, 1982 encounter of British Airways 77 where a Boeing 747, powered by Rolls-Royce RB-211 engines, flew into the eruption cloud of Mt. Galunggung near Indonesia [2]. Upon entering the cloud, the aircraft was forced into an emergency landing after all four engines experienced a temporary flameout. Upon investigation after landing, significant erosion and deposition was observed, as shown in Figure 1.2 [3]. This encounter, along with several others, prompted the aircraft community to address this new danger [4] and instruct pilots on tactics to avoid ash clouds and emergency procedures during an encounter [5]. The most well know instance of volcanic ash ingestion occurred on December 15th, 1989 when a Boeing 747-400, powered by GE CF6-80C2 engines, entered an ash cloud from Mt. Redoubt volcano near Anchorage, Alaska [6]. All engines experienced a flame-out after being throttled up in an attempt to climb above the debris. After numerous restart attempts and losing more than 10,000 feet in altitude, the crew was finally able to restart the engines and make an emergency landing. Repairs to the aircraft totaled more than 80 million dollars, which included the total replacement of all four engines. These and other instances of aircraft traversing through volcanic dust clouds prompted studies on the effects of ash ingestion for gas turbine engines and also the development of satellite and radar systems to warn pilots of possible encounters. Despite these precautions, the ingestion of volcanic debris is still considered to be a significant danger to commercial airliners.

Figure 1.2. Image of turbine nozzle guide vanes after ingestion of volcanic ash.

With regards to military aircraft, helicopter pilots in Desert Shield and Desert Storm were forced to come up with unorthodox operational procedures to help mitigate the negative effects of sand ingestion for virtually all helicopter platforms [7]. One such procedure was lifting the helicopter off before the recommended engine warm-up period and turning off the engines immediately after a landing. This reduced the total amount of sand being ingested into the engine while under load, which was primarily being stirred up by the rotors. Pilots also incorporated strict turbine washing regimes after each flight, which removed some of the deposits in the engine by flushing it with high pressure water.

Studies on Particle Ingestion

Several investigators have performed research as to the effects of particle ingestion with emphasis on gas turbines. The majority of these studies can be grouped into several categories: full-scale engine tests, accelerated erosion and deposition testing, and internal cooling blockage studies.

The earliest full-scale engine studies on dust ingestion were conducted by Batcho et al. [8] and Dunn et al. [9, 10] in 1987. For their tests, several engines were operated with a dust-laden inlet stream while monitoring engine performance. After completion of testing, each engine was disassembled and the effects of sand ingestion documented. They identified the following damage mechanisms that resulted in deterioration of engine performance: compressor erosion, deposition in the high pressure turbine, blockage of cooling holes in the high pressure turbine, and partial combustor fuel nozzle blockage. For their specific tests, however, the turbine inlet temperature was too low to result in sand glassification downstream of the combustor. While the concentration of sand ingested into the engine's Environmental Control System (ECS)

was monitored, no attention was given as to the effects of particles traveling through the coolant bypass and into the combustor and turbine internal cooling geometries.

As a result of the high cost associated with these types of engine tests, a Hot Section Test System (HSTS) was developed by Kim et al. [11] to simulate the exit temperature and flow of a T56 can-type combustor and the more modern F100 annular combustor. Actual engine hardware was installed downstream of the HSTS and different dust blends were introduced upstream of the HSTS for each test. It was concluded that deposition was dependent on sand composition, sand concentration, turbine inlet temperature, and metal surface temperatures. Molten deposition was reported in the turbine when inlet temperature and metal temperature were above 1177°C and 816°C, respectively. An independent cooling system was utilized thereby supplying the turbine components with a dust-free coolant stream, as the study was focused only on the effects of a particle laden main flow through the engine. Another study using the HSTS was performed by Weaver et al [12]. This study evaluated the effects of cooling hole diameter, hole roughness, turbine inlet temperature, and vane geometry with a dust-laden main flow. Test vanes included Inconel® 617 and Lamilloy film-cooled cylinders as well as F100-PW-220 first stage turbine vanes. Unlike previous studies, the coolant stream was modified to accommodate both clean and dust-laden flows. Inspection after testing showed that the cooling holes or passages had negligible clogging from dust while there was significant deposition on the external surfaces at elevated turbine inlet and metal temperatures.

Another subject of study pertaining to dust ingestion is the erosion caused by particle impacts with metal surfaces. Accelerated erosion studies at metal temperatures up to 815°C have been presented in the literature [13] showing the effects of impingement angle, temperature, particle and eroded surface character, and impact velocity [14, 15]. Recently the focus of this group has been investigating the effect of different turbine blade coatings on erosion rates and the resulting surface roughness characteristics. A study by Tabakoff and Simpson [16] compared uncoated turbine and compressor blades to a number of different coatings at elevated temperatures. After testing, the blade weight was taken and compared to the original value. A similar study of coated and uncoated turbine vanes was performed by Hamed et al. [17] with the primary focus being on the resulting vane surface roughness. All of these studies support the argument that particle ingestion causes material erosion and deposition on external compressor and turbine surfaces.

Other researchers have developed a high temperature accelerated deposition facility with emphasis on studying the characteristics and chemical composition of material deposits on turbine surfaces [18]. Jensen et al. [18] recognized the need for accelerated deposition studies as deposit formation could take as much as 25,000 operation hours in an industrial gas turbine. Bons et al. [19] also quantified the surface characteristics and roughness levels for in-service turbine blades and vanes to serve as a basis of comparison for their accelerated tests. Results of the investigation by Bons et al. identified the leading edge region as having the highest levels of external deposition for the evaluated turbine hardware. Another interesting finding of this study was the measurement of substantial deposition on in-service turbine vanes operated at a turbine inlet temperature below 900°C, which was substantially less than the 1177°C threshold for deposition previously stated by Kim et al [11].

A review of the current research on erosion and deposition in turbomachinery was presented by Hamed et al. [20]. In their paper, the authors presented a review of erosion studies including numerical studies of particle trajectories and collisions for the main gas path. A summary of computational and experimental studies on the mechanisms of particle delivery and deposition was also presented. The authors also addressed the performance and lifecycle reductions which are associated with erosion and deposition. The paper does not, however, address what effects erosion and deposition have on internal cooling geometries. This is because of a lack of experimental research on internal cooling blockage associated with dirty inlet air.

A numerical study of particles within a square channel having periodically spaced ribs was performed by Shah and Tafti [21]. For their study, 10 μm particles were shown to be more sensitive to large flow structures within the channel. Particle impacts on the rib surfaces were evenly distributed and impacts on the side walls were preferentially concentrated in the region of the top and bottom ribs. This was not true for the 100 μm particles, which showed significantly higher tendency to impact the upstream surface of the rib as well as the reattachment region behind the rib.

Walsh et al. [22] have currently performed the only experimental investigation within the literature directly focusing on the effects of a dust-laden coolant stream. Their study was focused on the effects of metal temperature, coolant temperature, coolant pressure ratio, number of cooling holes, sand amount, and sand diameter on cooling hole blockage for a test coupon with laser drilled film-cooling holes. Walsh et al. concluded that increases in metal temperature

had the most significant effect on cooling hole blockage. Walsh et al. reported 1-6% reduction in test coupon flow parameter at engine representative metal and coolant temperatures for a pressure ratio range of 1.1-1.6 across the cooling holes.

Geometries of the Double Wall Liners

Combinations representing four different designs of a double wall liner utilizing impingement and film-cooling were chosen as representative of either a combustor liner or blade outer air seal. All liners consisted of an impingement plate, spacer plate, and film-cooling plate, as shown in Figure 1.3. A periodic representation of the alignment between impingement and film holes is shown in Figure 1.4 for each of the four liners tested. As can be seen, for each double wall liner there was more or less overlap of the impingement jet locations with respect to the film hole entrances.

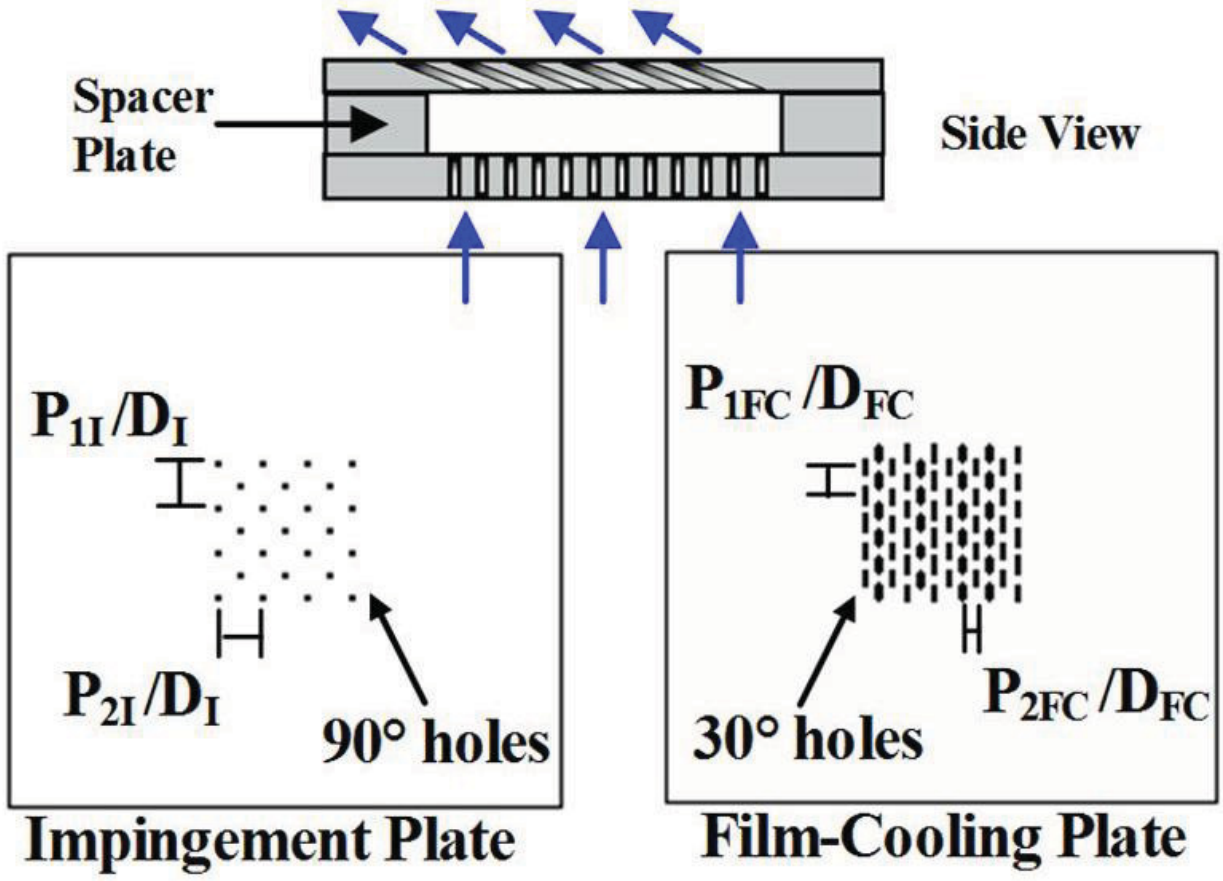

Figure 1.3. Representative impingement and film-cooling double wall liner.

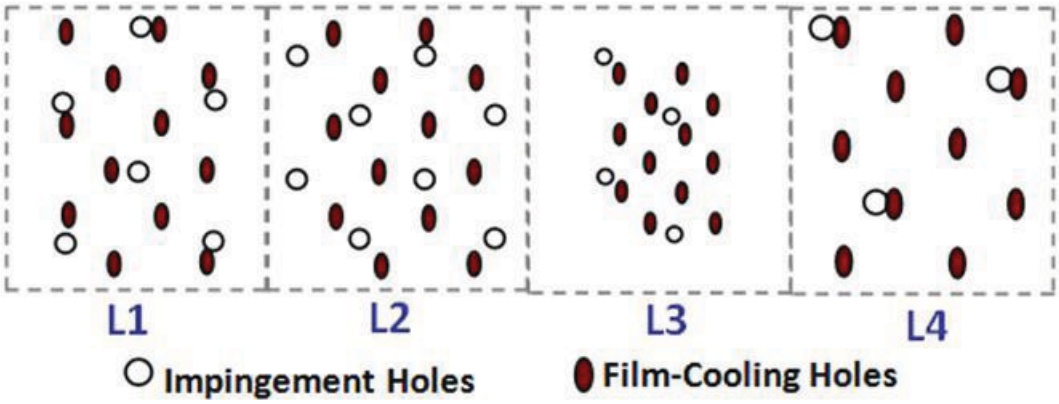

Figure 1.4. Overlap between impingement hole exit and film hole entrance (periodic section shown).

A 9 cm by 9 cm square sheet of Inconel® 625, which is a high nickel superalloy with similar physical properties to metals used within the engine, was used as the material base for each plate. The sheets had a machined finish and the thicknesses of the impingement, film-cooling, and spacer plates were 1.27 mm, 0.89 mm, and 1.65 mm respectively. The impingement and film-cooling holes were machined 90° and 30° inclined to the surface, respectively. All cooling holes were created using electron discharge machining (EDM), chosen for its high dimensional tolerance at this scale in comparison to traditional and laser machining. Each spacer plate was machined with a 3.8 cm square hole for the purpose of forming a sealed cavity between the impingement and film plates. All twelve plates were also machined with a six-hole mounting pattern to assure correct alignment for each test. Detailed information on each design is shown in Table 1.1.

Table 1.1. Double Wall Liner Details

	Film-Cooling					
Liner#	N_{FC}	D_{FC} (μm)	A_{FC} (mm^2)	L_{FC}/D	P_{1FC}/D	P_{2FC}/D
L1	64	635	20.3	2.8	7.0	7.1
L2	64	635	20.3	2.8	7.0	7.1
L3	100	508	20.3	3.5	8.8	7.1
L4	52	762	23.7	2.3	5.9	6.5
	Impingement					
Liner#	N_I	D_I (μm)	A_I (mm^2)	L_I/D	P_{1I}/D	P_{2I}/D
L1	25	635	7.9	2.0	11.3	11.3
L2	32	635	10.1	2.0	11.3	10.0
L3	25	508	5.1	2.5	14.1	14.2
L4	13	762	5.9	1.7	9.4	13.1

For the geometries shown in Figure 1.4, L1 was chosen as representative of an actual engine combustor liner. Each design was varied off of the L1 design to assess the effect of cooling hole diameter, total cooling flow area, and relative alignment between the impingement and film. The number of impingement holes was increased between L1 and L2 while keeping cooling hole diameter and the number of film-cooling holes constant. This allowed for the investigation of total impingement flow area on sand blocking levels. Cooling hole size was reduced by 20% for L3 while keeping the total film-cooling flow area and impingement hole pattern equal to the values for L1. L4 had an increased cooling hole diameter of 20% above L1 and L2 in addition to a different pattern for the film-cooling and impingement holes.

Experimental Facility and Methodology

The level of hole blockage was quantified through the use of the flow parameter, as was done by Walsh et al. [22]. The flow parameter (FP), shown in the nomenclature, is a convenient definition of a non-dimensional mass flow parameter [23]. In the definition, P_{exit} refers to the discharge pressure of the cooling hole. During testing each liner was exhausted to the ambient laboratory environment, which allowed P_{exit} to be replaced by P_{amb} in the definition of flow parameter. There is one unique flow parameter that results for a given geometry, temperature, and pressure ratio.

The pressure ratio is defined as the ratio of supply pressure upstream for the impingement plate to the exit static pressure of the film-cooling plate. The coolant supply pressure, P_{0C}, was measured upstream of the impingement plate. If either the film-cooling or impingement holes were partially blocked, one would expect to measure a lower flowrate than for an unblocked hole at the same pressure ratio. This drop in flowrate also corresponded to a drop in flow parameter. Ultimately, matching the flow parameter with engine conditions resulted in a matched air residence time within the liner. For a realistic coolant temperature, matching the air residence time resulted in a particle residence time which was similar to engine values. Matching the particle and air residence times assured that the thermal response of each particle, set by radiation and convection within the part, was equivalent to that occurring within the engine. It was because of these relationships that matching flow parameter as well as coolant and part temperatures were important for studying the blockage of an internal cooling geometry.

Before sand testing was performed, a baseline flow parameter curve, shown in Figure 1.5, was established for each liner at ambient and elevated temperatures. At a given coolant temperature, each liner had a unique relationship between pressure ratio and flow parameter. Varying the coolant temperature changed the fluid viscosity within the liner, resulting in a new relationship between the flow parameter and pressure ratio, as shown in Figure 1.5. Each respective baseline was used to evaluate the total reduction in flow parameter (RFP) for a blocked liner, as shown in the nomenclature.

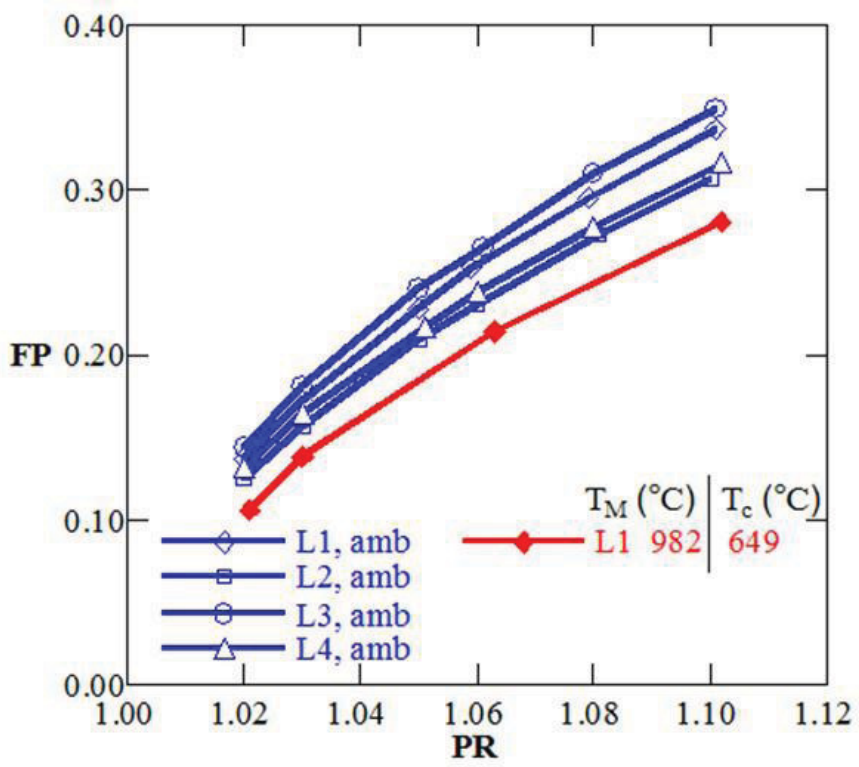

Figure 1.5. Baseline flow parameter curves for all liners at ambient conditions and L1 at heated conditions.

Prior to each blockage test where sand was injected into the air stream, the measured baseline flow parameter was repeated to ensure that the hole passages were clear of any sand from the previous test. Note that the blockage was based on the flow parameter that occurred at the final pressure ratio of the clogged liner. This procedure is illustrated in Figure 1.6 as a zoomed graph of ambient and heated baseline curves with representative data points. Under experimental conditions, the result of sand blocking with the liner was a sudden increase in pressure ratio and decrease in flow parameter. After clogging with sand, liner flow parameter and pressure ratio remained at their blocked values until the liner was cleaned manually. This

method of using the reduction in flow parameter to quantify sand blockage within cooling holes was published in a similar study by Walsh et al. [22].

The reduction in flow parameter can be reported several ways, whether an ambient temperature or heated test was conducted. The previously defined variable, RFP, was used to compare the reduction in flow parameter under ambient conditions. For all cold cases, the RFP was based on the difference between the blocked flow parameter, FP_B, and the equivalent unblocked flow parameter at the blocked pressure ratio, FP_0. The calculation of RFP is illustrated in Figure 1.6. At heated conditions, the RFP_H was used whereby FP_{0H} was the equivalent unblocked baseline flow parameter at the blocked pressure ratio and FP_{BH} was the blocked value at heated conditions, as shown in Figure 1.6.

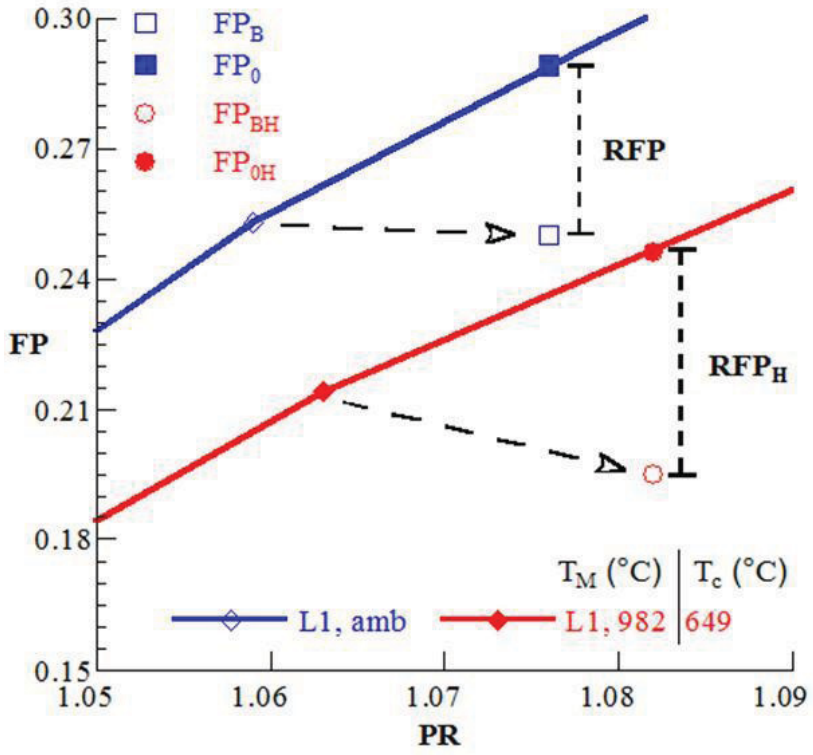

Figure 1.6. Testing procedure for calculation of %RFP.

Test Facility

Originally constructed by Walsh et al. [22], a test facility that generated a constant pressure upstream of the test coupons was modified to accept the double wall liner coupons, as seen in Figure 1.7. High pressure, room temperature air was supplied as coolant to the test coupons. This air was supplied to the lab, prior to which it was filtered and dried, by an auxiliary

compressor facility at approximately 550 kPa. A self-adjusting precision pressure regulator was used to control and regulate a constant coolant pressure. Downstream of the pressure regulator was a laminar flow element, having a maximum capacity of 1400 cm^3/s, that measured the total coolant flowrate through each liner. The required flowrate range was 170-830 cm^3/s.

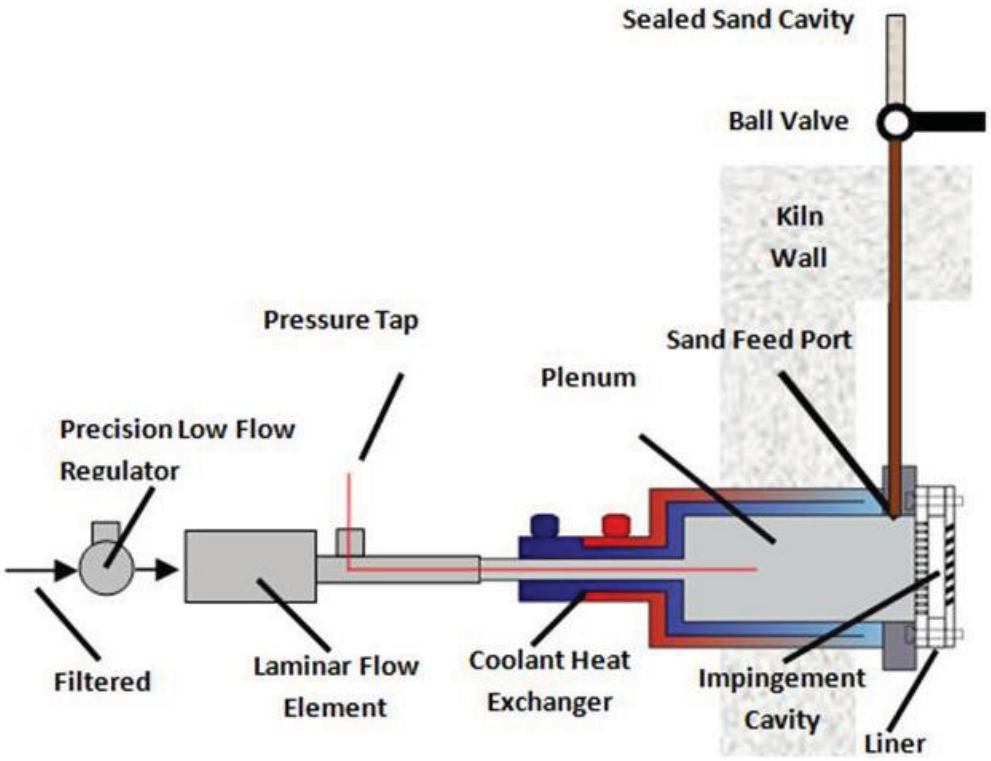

Figure 1.7. Test facility used for studying sand blockages in the double wall liner coupons.

Coolant temperatures were recorded within the center of the plenum chamber using a type K sheathed thermocouple probe as shown in Figure 1.7. Coolant pressure was also measured at this location using a 1.6 mm diameter Inconel® tube as a pressure probe. The ratio of plenum diameter to impingement hole diameter varied from 144:1 to 96:1, thus assuring that pressure measured within the chamber was equivalent to the total coolant pressure.

Control of the metal temperature was accomplished by placing the liner and sand feed pipe within an electric kiln. The coolant temperature was controlled with a multi-pass heat exchanger supplied with ambient temperature compressed air, also shown in Figure 1.7. Two fiberglass shielded type K thermocouples were affixed to the film-cooling plate using a high temperature ceramic adhesive to measure the metal temperature of the film-cooling plate. Each thermocouple was located in close proximity to a film-cooling hole, but not within the coolant

jet. For each test, the difference in metal temperature measured between the two thermocouples was less than 5°C. Variation of the metal and coolant temperature was accomplished by changing the kiln power and auxiliary heat exchanger flow for the coolant stream.

An electric oven, set at 150°C, was used to dry the sand for four hours before each test. This preliminary drying was performed to avoid humidity clumping of the sand. Sand delivery to the liner was accomplished using a sealed gravity feed system, shown in Figure 1.7. For each test, the prescribed sand amount was loaded above a valve that controlled access to the sand feed pipe. Opening this valve allowed the sand to pass vertically down the feed pipe, which was approximately 10 cm in length. This pipe terminated just upstream of the impingement plate and above the first row of cooling holes. The sand feed pipe was terminated above the cooling holes to insure that it did not disturb the inlet flow into the impingement plate. It is important to note that this resulted in a slightly higher mass loading of sand through the upper holes than through the lower holes. In addition, visual inspection after testing showed only trace amounts of sand within the coolant plenum, which meant that all the sand had become entrained within the coolant flow.

Since the tube supplying the sand was located within the hot portion of the kiln, as shown in Figure 1.7, it is important to recognize that there was significant heat up of the sand prior to entering the test coupon. Heat transfer to the falling sand was driven primarily through radiation from the section of feed tube which was exposed to the heated kiln. It is also important to note that the kiln temperature needed to be adjusted to maintain a constant coupon metal temperature for different coolant flowrates. For a constant coolant and kiln temperature, increasing the coolant flowrate to the coupon resulted in a decrease in the part's metal temperature. Because of this, the kiln temperature was varied to maintain a constant metal temperature for the different coolant flowrates. As a result, the supply tube temperature was changing with the kiln temperature. With the tube temperature changing, so did the entering sand temperatures. At elevated temperatures the probability of deposition increased when using heated sand. Therefore a transient calculation was performed for each test to estimate the sand temperature as it flowed into the impingement plate. Reported values of sand temperature were based on the mean particle size and assumed that the supply tube temperature was equal to the kiln temperature.

Each liner plate was affixed in the test setup using a ceramic adhesive and sealant that formed an airtight seal once cured up to 1260°C. Most importantly, the adhesive's coefficient of

thermal expansion was similar to that of Inconel® 625, making it an ideal high temperature sealant. Steps were made to ensure each joint was hermetically sealed before and after each test, which was verified through repeating the baseline flow parameter-pressure ratio curve.

Sand Characterization

The chosen test sand, Arizona Road Dust, is comprised primarily of crushed quartz [22]. The analysis of each of the sand samples agree with the manufacturer's specification stating that it contains different phases of quartz (SiO_2) up to approximately 68-76%. The other major constituent is aluminum oxide (Al_2O_3) between 10-15%, with traces of iron oxide (Fe_2O_3), sodium silicate (Na_2O), lime (CaO), magnesium oxide (MgO), titanium dioxide (TiO_2), and potassium oxide (K_2O), in descending concentration. Arizona Road Dust has been used extensively for particle ingestion testing by the aviation, automotive, and filtration industries. Its chemical composition closely matches the types of sand found in arid desert-like climates. In addition to having a wide variation in particle size, this particular sand agglomerates readily forming large particles.

In characterizing the sand, a number of measurement methods were originally used to verify the particle size distribution. To reduce the particle breakup during the sizing measurement, a dry analysis was performed by using a series of mesh sieves ranging from 53 μm to 850 μm. The sieves were stacked thus filtering the sand in different bandwidths. These results are given in Figure 1.8. The initial weight of each sieve and the sand were recorded. The entire stack was then lightly agitated for 4 hours. After the agitation, each sieve was weighed and the amount of sand within each size band calculated. Several large conglomerates of particles were observed in the 850 μm sieve. The maximum linear dimension of the conglomerates was measured by calipers as ~3000 μm and is listed in Figure 1.8 as the 100% data point. A minimum particle diameter of 0.6 μm was measured using a Horiba Partica LA-950 laser diffraction analyzer. The LA-950 utilizes both a wet and dry measurement method, both of which caused significant breakup of particle agglomerations and were therefore deemed unsuitable for measurement of the overall size spectrum. The results of the laser diffraction methods are also included in Figure 1.8.

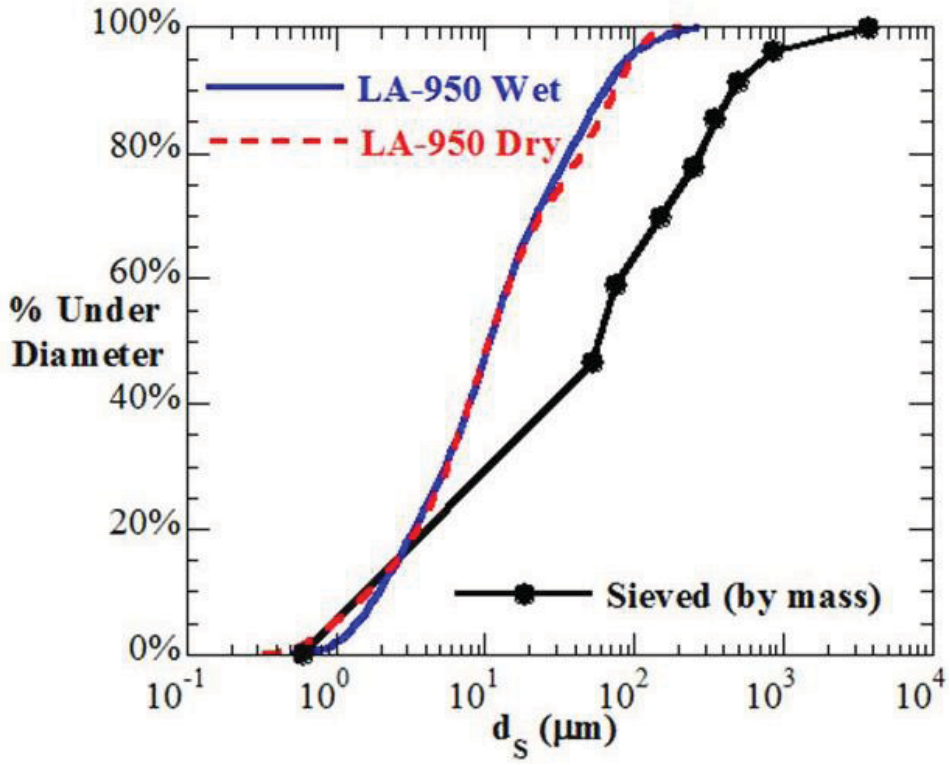

Figure 1.8. Size distributions for the test sand obtained by several methods.

Unless indicated, the amount of sand used was 0.35g for each of the tests. The 0.35g corresponded to a particle mass loading of 0.8, which was used by Walsh et al. [22] as representative of actual levels within the engine. Particle mass loading is defined as the mass flux ratio of the dispersed phase to the continuous phase [24]. For these tests the sand and cooling air served as the dispersed and continuous phases, respectively. Walsh et al. determined the appropriate mass loading by comparing the flow parameters of clean turbine components with field-operated components in which sand had entered the coolant stream and blocked cooling holes.

Deposition within the engine is most likely to occur over a longer period of time than the method used in this study in which a slug of sand was introduced to the part. To assure realistic results, several tests were performed to determine if a slug of a given sand amount has the same blocking characteristics as when the given sand amount was divided into portions. It was verified that the cumulative sand amount equaled that used for the single slug tests. Representative results of these comparison tests are shown in Figure 1.9. The tests indicate an insensitivity to how the sand was introduced into the liner as both the cumulative and slug tests resulted in the same overall blockage.

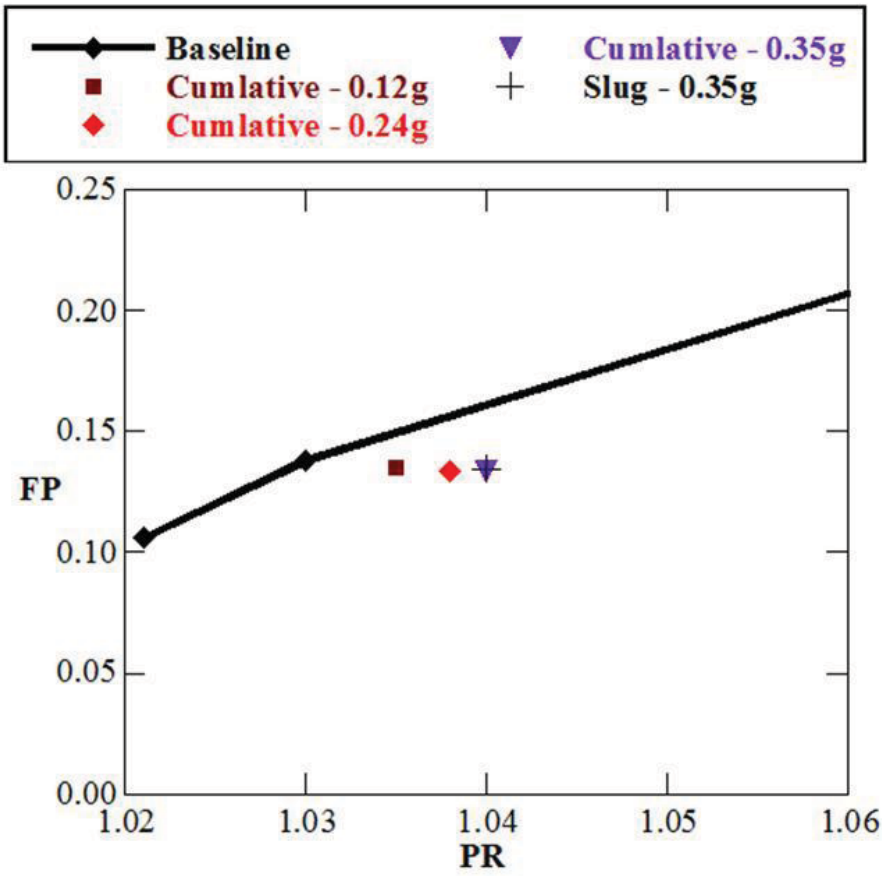

Figure 1.9. Cumulative blocking effects versus slug flow for L1 at T_M=982°C and T_c=649°C.

Testing Procedure

Before each test, deposited sand from the previous test was removed from the impingement and film-cooling plates. The liner was considered free of previous sand remnants once its original baseline flow parameters could be reproduced.

After confirming the appropriate baseline flow parameter curve, the desired pressure ratio was set between 1.02 and 1.1. For an unheated test, the system was ready for sand injection. When performing a heated test, the test apparatus was placed in the kiln prior to setting the appropriate pressure ratio. The auxiliary cooling air flowrate and kiln power were varied until the desired coolant and metal temperature were set and steady. Required time to reach steady state for a heated test varied from 3-6 hours, dependant on the desired test conditions.

With the pressure ratio set and steady-state temperatures achieved, the sand feed valve was quickly opened allowing the prescribed amount of sand to flow through the part. Once the pressure ratio and flow parameter were steady again, which typically took less than a few

seconds, the new pressure ratio and flow parameter were recorded. The appropriate reduction in the flow parameter was then calculated relative to the clean liner flow parameter at the blocked pressure ratio. A 25 case repeatability study conducted by Walsh et al. [22] showed that three tests conducted for each case resulted in repeatable results to within 7%. In addition, multiple investigators have performed these studies spanning over one year. Their results also indicate that an average of three tests resulted in good repeatability. Each data point presented by this study corresponds to an average of three independent tests.

Uncertainty Analysis

Uncertainty and repeatability tests conducted by Walsh et al. [22] showed that three tests provided an adequate repeatability for this type of cooling blockage tests. Average variation of RFP between each group of three tests was 2.5% for both ambient and heated conditions. The propagation of uncertainty associated with the measurement methods was calculated for all test conditions, as outlined by Figliola and Beasley [25], to validate the observed results and trends. At both ambient and heated conditions, the uncertainty in flow parameter was approximately ±2% of the measured value for all pressure ratios. At ambient conditions, the overall uncertainty in RFP was 0.11±0.011 at PR=1.02 and 0.16±0.01 at PR=1.10. At heated conditions, the uncertainty in RFP_H was 0.18±0.016 for PR=1.03, T_M=982°C, and T_c=649°C. Negligible variation in uncertainty was calculated between the different liner geometries. In addition, the uncertainty associated with measuring the prescribed sand amount was 0.35g ±0.005g.

Derivation of the Test Matrix

Significant consideration was given to the generation of the test matrix, shown in Table 1.2. The nominal coolant temperature chosen for the high temperature testing was 649°C. With respect to external metal temperatures, the combustor liner typically operates in excess of 1000°C. However, a maximum metal temperature of 982°C was chosen because of the material limitations of Inconel® 625 as it melts at a lower temperature than proprietary engine alloys.

With regards to entering sand temperature, no information was available as to the levels seen within the engine. Whether entering sand temperature was above or below the coolant temperature value was a function of particle residence time, slip velocity, and wall collision rate. Since realistic engine values for these variables are unknown, the maximum limitations of the

testing capabilities were chosen to evaluate this parameter resulting in an entering sand temperature range of 316°C to 760°C. This range was set by the minimum and maximum heated length of the sand feed tube within the limitations of the kiln's interior dimensions.

Table 1.2. Parameters Used for Combustor Liner Study

	T_M (°C)	T_c (°C)	m_s (g)	PR
L1	20°C		0.21, 0.35, 0.52	1.02, 1.03, 1.06, 1.10
L2			0.35	1.02, 1.03, 1.06, 1.10
L3			0.21, 0.35, 0.52	1.02, 1.03, 1.06, 1.10
L4			0.35	1.02, 1.03, 1.06, 1.10
L1	871, 982	538, 593, 649	0.35	1.03
L2	982	649	0.35	1.03
L3	982	649	0.35	1.03
L4	982	649	0.35	1.03

Discussion of Results

A number of tests were conducted to analyze the effect of sand being ingested into several double wall liner designs. The experimental results are broken into two sections: ambient temperature and elevated temperature. For the ambient temperature tests, the effects of pressure ratio, liner geometry, and sand amount were investigated. At elevated temperatures, the effects of liner geometry, film-plate metal temperature, and entering sand temperature were evaluated. The ambient results will be discussed prior to the high temperature results. In the following sections, the reduction in flow parameter will be referred to as an increase or decrease in "blockage".

Ambient Temperature Results

Figure 1.10 compares the blockage levels for all four liner geometries at a range of pressure ratios given a nominal sand amount of 0.35g. An increase in pressure ratio from 1.02 to 1.10 resulted in elevated blockage for all liners with a maximum increase in RFP from 12% to 20% for L3. As seen in Figure 1.10, at all pressure ratios the liners showed the same performance trend: lowest values of blockage for L2 and highest blocking levels observed with L3. The results show that the cooling hole diameter, both impingement and film, did not solely dictate the level of blocking for a given design. L3, despite having a 33% smaller cooling hole

diameter than L4, varied in RFP less than 1% relative to L4. L1 and L2, despite having the same cooling hole size, showed a difference in blockage of approximately 6% at a pressure ratio of 1.06. However, when considering the total flow area through the impingement plate, consistent trends were identified. Figure 1.11 shows the same data as Figure 1.10, but replotted versus the total flow area of each liner's impingement plate. Representing the data in this manner indicates that blocking for a given liner design decreases monotonically with increasing impingement flow area.

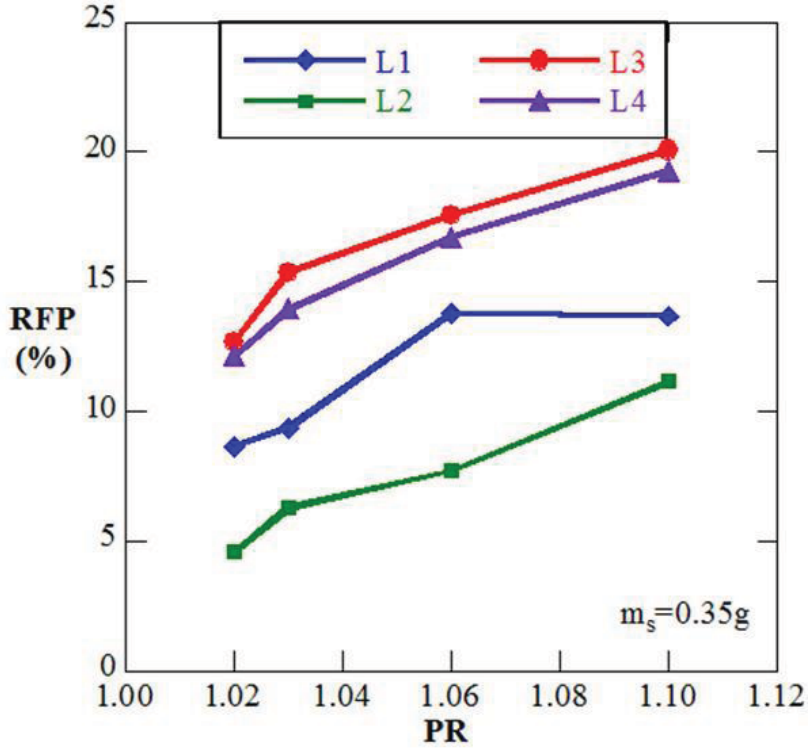

Figure 1.10. %RFP verses pressure ratio for all liners at ambient temperature.

It was concluded that blocking levels within the liner, at ambient temperatures, were influenced by several different factors that are unique to a double wall liner design. The two dominant factors were: filtration of large particles by the impingement plate before entering the impingement cavity (refer Figure 1.3 and Figure 1.7) and the breakup of particles which travel through the impingement holes and impact against the upstream side of the film-cooling plate.

It was observed that the impingement plate acted as a filter for the film-cooling plate with respect to sand particles and agglomerations whose maximum linear dimensions were equal to or greater that the impingement hole diameter. Approximately 7% of the particles tested were

above 600 μm in diameter, which was nominally the size of each liner's impingement holes. Particles in this size range blocked within the impingement holes and were therefore unable to convect into the cavity upstream of the film-cooling holes. It is also important to recall that the film-cooling and impingement hole sizes were matched for each liner configuration. For this particular design, the impingement plate was filtering out all of the larger particles which could have blocked cooling holes within the film-cooling plate.

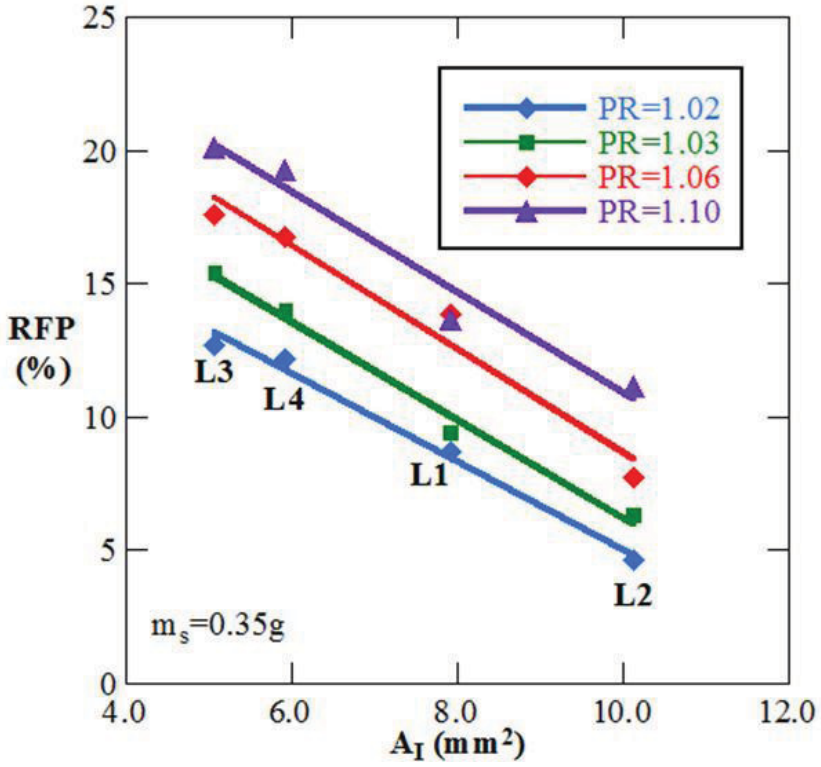

Figure 1.11. Ambient temperature results plotted versus impingement flow area for all liners.

Particles which did not stick to the upstream side of the impingement plate or block within the impingement holes were carried into the impingement cavity by the coolant flow. Upon exiting the impingement holes, the particles impacted on the upstream surface of the film-cooling plate. This impingement broke up the particles, increasing their likelihood to pass through the film-cooling holes. Post-test inspection of the liner confirmed that the particles were impinging on the upstream side of the film-cooling plate, as shown in Figure 1.12. The particle impingement velocities were high enough to locally abrade the metal surface, as shown by the dark circles on the upstream side of the film-cooling plate in Figure 1.12.

Figure 1.12. Post-test images of sand deposition patterns at ambient temperature for L1 at PR=1.03.

A study by Land et al. [26], performed congruently with this research, confirmed that particle breakup does occur within the double wall liner. The study compared the relative blocking characteristics of a combined impingement and film-cooling liner with a film-cooling only liner. Land et al. [26] reported a ~ 300% increase in blockage with the film-cooling only configuration when compared to the double wall liner, thus verifying that the impingement resulted in a beneficial breakup of the sand particles within the cavity.

For the presented research, further visual inspection of the impingement and film-cooling holes showed that the bulk of the blockage occurred at the entrance to and within the impingement holes. Conversely, very little blockage was observed within or around the film-cooling holes. The breakup of impinging particles and impingement plate filtering resulted in significantly higher amounts of blockage in and around the impingement holes when compared to the film-cooling plate.

Since all tests were performed with a nominal amount of sand, it is logical that a liner with less impingement flow area would block at a higher rate than a liner with a large impingement flow area. Impingement flow area and particle breakup do not, however, offer insight into the cause of elevated blocking for all liners as pressure ratio was increased. Blocking sensitivity to pressure ratio results from how well particles follow the coolant flow. As the pressure ratio was increased, so did the mean velocity of air through the part therefore resulting in a decreased time characteristic of the flow, τ_f. The particle response time, τ_s, is commonly used to describe the time required for a particle to respond to a change in velocity. In an average sense, τ_s remained constant for our testing since it was primarily a function of particle

density and diameter. Therefore an increased pressure ratio resulted in an increased average particle Stokes number (St).

Stokes number is commonly used to define how well a given particle will follow the fluid surrounding it. Particles with a St << 1 are assumed to follow the flow perfectly while particles having a St >> 1 are considered ballistic and are mostly unaffected by the fluid [24]. Studies by Tu et al. [27] showed that, for a rebounding flow over a curved wall, increased Stokes numbers were associated with particle trajectories deviating from the fluid streamlines thereby increasing the likelihood of wall collisions.

Calculations were performed to determine the Stokes number of 1 μm and 50 μm sand particles traveling through the liner. The impingement jet velocity and impingement hole diameter were chosen as the characteristic length and velocity of the coolant flow within the cavity. At 50 μm, particle Stokes numbers were above 500 for all pressure ratios. It was therefore assumed that the trajectories of sand particles at this size or larger deviated greatly from the cooling air path. For a 1 μm particle traveling through an impingement hole, Stokes numbers were slightly less than unity for all four liners. Therefore the Stokes number of the 1 μm particles fell within the range where particle motion was significantly affected by the coolant air but did not follow it perfectly. Increasing pressure ratio from 1.02 to 1.10 doubled the particle Stokes number for all particle sizes. We may infer that increases in pressure ratio also corresponded to an increased likelihood that sand particles would collide with the surfaces in and around the cooling holes. The increased number of wall collisions ultimately related to a higher probability of deposition for a given sand amount. Therefore elevated collision and deposition rates were the cause of the increased blocking at higher pressure ratios.

Ambient Temperature Results with a Varied Sand Amount

As explained previously, L3 exhibited the highest blockage of the four liner designs tested because of its relatively small impingement flow area. Therefore L3 was chosen to evaluate the sensitivity of the blocking to sand amount. As previously described for the nominal case, sand amounts were determined from the studies by Walsh et al. [22] based on comparing clean and field-operated turbine components. The maximum and minimum particle mass loadings from Walsh et al. [22] were matched for the double wall liners resulting in high and low

sand amounts of 0.52g and 0.21g, respectively. The effect of sand amount on L3 was then evaluated for all pressure ratios, as shown in Figure 1.13.

As shown in Figure 1.13, a 51% increase in sand amount resulted in an average increase in blocking of 18% across all pressure ratios. Lowering the sand amount by 41% resulted in an average 35% decrease in blocking. At pressure ratios above 1.03, these results agree with the results of Walsh et al [22] which showed a near linear dependence of blocking on the injected sand amount at a given pressure ratio. It is important to note that the studies by Walsh et al. were conducted at pressure ratios above 1.1. The effect of varying sand amount was also evaluated for another liner at a pressure ratio of 1.06 to assure that the results were not dependent on the film-cooling and impingement geometry. As shown in Figure 1.14, L1 exhibits the same trend as L3 with linearly increasing blockage as sand amount was increased.

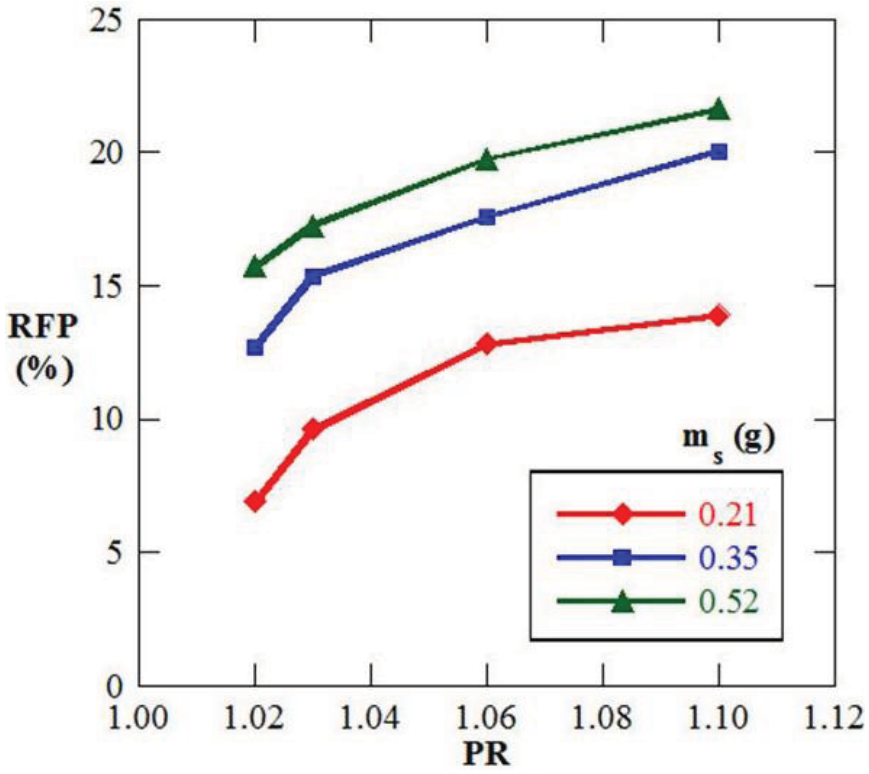

Figure 1.13. Effects of sand amount variation for L3 at ambient temperature.

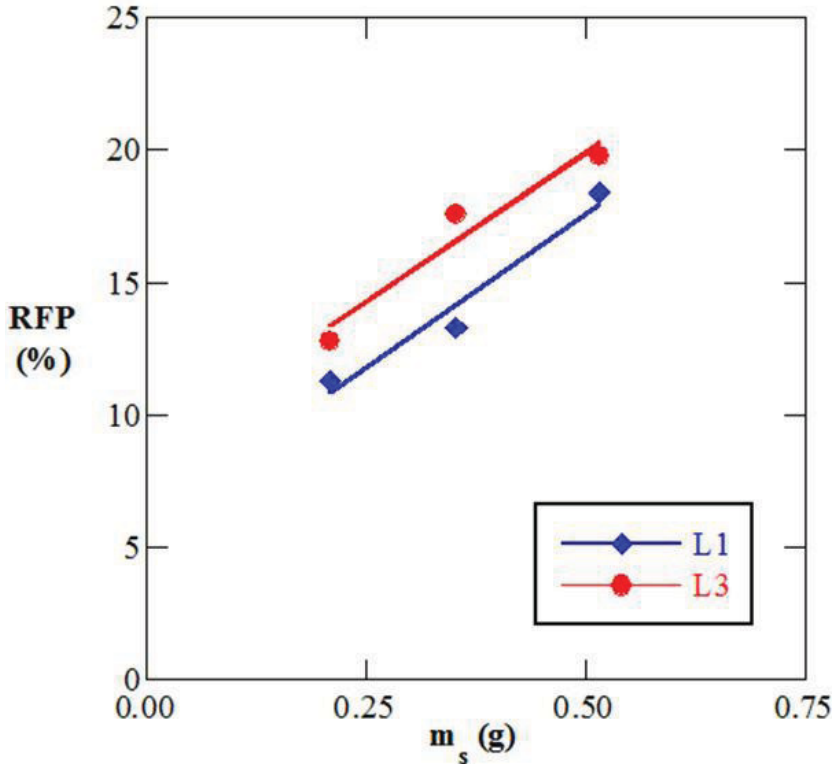

Figure 1.14. Varying sand amounts for L1 and L3 at PR=1.06 at ambient temperature.

Elevated Temperature Results

Each liner was evaluated with a constant metal, coolant, and entering sand temperature at T_M = 982°C, T_c = 649°C, and T_s ~ 760°C. In addition to these tests, as was described previously, the length of the sand delivery pipe was changed such that less of it was inside the kiln to lower the sand temperature for L1 and L2 to T_s ~ 370°C. As stated previously, a transient heat transfer calculation was performed to estimate the sand temperature flowing into the impingement plate. It is important to note that all elevated temperature tests were performed with a nominal sand amount of 0.35g.

As discussed previously, the reduction in flow parameter or blockage was calculated differently at heated condition than what was performed for the ambient temperature testing. At heated conditions, the RFP_H was used. In this equation for the reduction in flow parameter, FP_{0H} was defined as the equivalent baseline flow parameter at heated conditions and FP_H was the blocked value at heated conditions. Figure 1.6 illustrates the testing procedure and calculation of this parameter at heated conditions.

The high temperature results for each liner are shown in Figure 1.15 with the previously reported values of blockage for the ambient temperature results. Each liner showed an increase in blocking at elevated temperatures. L2 performed the best with the lowest values of blockage for both heated and ambient temperatures. L3 had the highest operational flexibility, exhibiting very little change in sand blockage between heated and ambient temperature testing. The largest increase in blockage, by means of an increase in temperature, occurred with L1. Explanation of the elevated temperature results was accomplished by disassembling each liner after testing and noting differences in the sand blocking patterns.

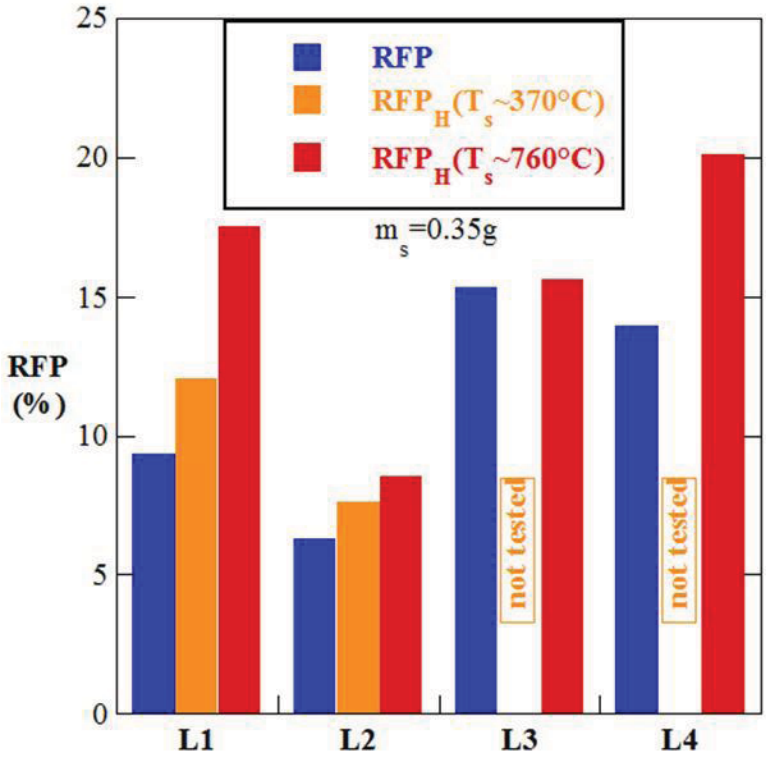

Figure 1.15. Comparison of all liners for ambient and heated test at T_M-982°C and T_c=649°C and two ranges of entering sand temperature at PR=1.03.

At elevated temperatures, the liner blocking results no longer scaled with impingement area as it did under ambient conditions. Visual inspection after heated testing confirmed that the sand blockage had moved into the film-cooling holes and continued to occur within the impingement plate. Recall that negligible amounts of blocking were observed within the film-cooling holes at ambient conditions. It was apparent that the impingement plate was still acting as a filter for larger particles, but observations of completely blocked film-cooling holes meant there was a new blocking mechanism occurring within the liner for heated conditions.

Under heated conditions, blockages within the film-cooling plate resulted from the sand becoming sticky at elevated temperatures. This stickiness increased the likelihood of sand adhering to the impingement and film-cooling plates as well as within the cooling holes. It was found, as shown in Figure 1.16, that the deposited sand takes the shape of small mounds on the upstream side of the film-cooling plate at elevated temperatures. Figure 1.16 illustrates these sand mounds in comparison to the case under ambient temperatures, as shown in Figure 1.12. As shown, each sand mound was centered on the location of the impingement hole exit. These mounds formed around and within the entrance to the film-cooling hole when there was overlap between the impingement hole exit and film-cooling hole entrance, thereby contributing to an increase in blocking within the nearby film-cooling holes.

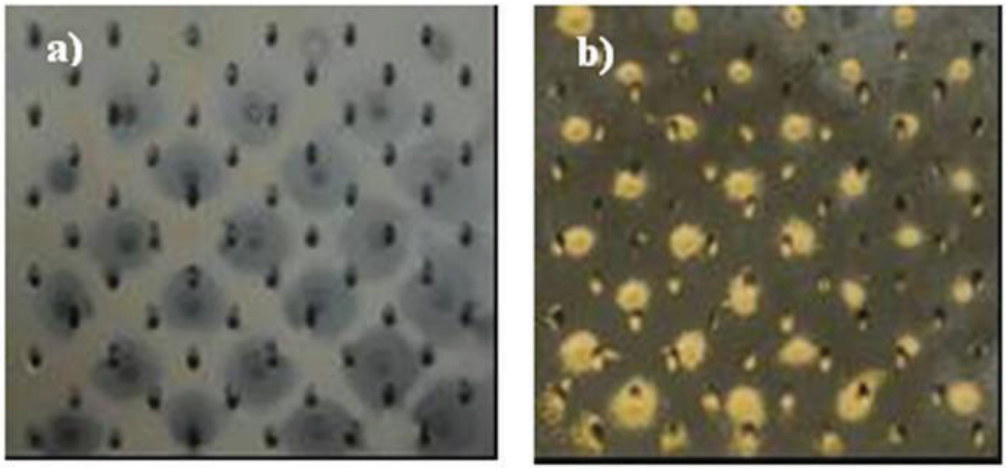

Figure 1.16. Upstream side of the L1 film-cooling plate at PR=1.03 for a) ambient and b) T_M=982°C, T_c=649°C, and T_s=386°C.

Recalling Figure 1.4, L2 and L3 showed little overlap between the impingement and film-cooling holes. The opposite was true for L1 and L4, which had much higher levels of cooling hole overlap. Therefore L2 and L3 were less sensitive than L1 and L4 to operating at elevated temperatures because of the difference in overlap between impingement and film-cooling holes. It was also of note that L4 showed the highest blockage at elevated temperature despite having the largest cooling hole diameter. Again, this was attributed to L4 having the highest level of impingement/film-cooling hole overlap when compared with the other three liners. This result further reinforced the hypothesis that the combination of sand stickiness and the amount of cooling hole overlap were responsible for the increase in blocking observed at elevated temperatures.

Results with Varied Metal and Sand Temperatures

Varied metal and entering sand temperature tests were conducted with L1 as it showed the greatest sensitivity to being operated at elevated temperatures. The range of metal temperatures tested, 871°C to 982°C, correspond to realistic values of metal temperature for the combustor liner. As discussed previously, the range of entering sand temperature was varied to the maximum allowable limitations for the testing setup. This value was set by the heated length of sand feed tube, as discussed previously. All tests were performed with a fixed coolant temperature of T_c = 649°C.

The results of this study are shown in Figure 1.17 along with the sand temperature entering the liner for each test. The blockage level at ambient conditions is also shown in Figure 1.17 to serve as a basis of comparison for the elevated temperature tests. For a relatively low entering sand temperature, the increase in metal temperature from ambient to 871°C resulted in a 13% increase in blocking. An increase of 17% in blocking was observed between ambient and T_M = 871°C for a relatively high entering sand temperature. Through visual inspection it was concluded that a metal temperature of 871°C was too low to sufficiently heat the sand as it passed through the liner. However, increasing the liner metal temperature to 982°C resulted in a dramatic effect. As shown in Figure 1.17, for a relatively high entering sand temperature blocking increased by 60% compared to T_M=871°C. This corresponded to two times the blocking at ambient conditions. For a relatively low entering sand temperature, blocking increased by 14% when compared to T_M=871°C

The dramatic increase in blockage for a high entering sand temperature occurred because the sand was becoming sticky at higher temperatures. The driving heat transfer mechanism of this effect was radiative heating from the liner's metal surfaces to the sand. Collisions with the surface also aided in heating up of the sand. The higher temperature, tackier sand was therefore more likely to deposit on the internal surfaces of the liner. After a particle adhered to the surface, it provided an area where subsequent particles could readily adhere. Inter-particle collisions of sticky particles also resulted in increasing mean particle size. Agglomeration of colliding particles resulted in an increase in Stokes number, which is a function of the particle diameter. Increasing Stokes numbers corresponded to a greater deviation of particle trajectories from the flow streamlines, thus increasing the likelihood of wall-collisions and deposition. Visual inspection of parts after testing, shown in Figure 1.18, support the conclusion that the

combination of elevated metal temperature and high entering sand temperature was having a significant effect on particle stickiness. At low entering sand temperatures, light color sand was observed which could be easily removed with high pressure air. At high entering sand temperatures, sand color darkened appreciably and could not be dislodged by high pressure air alone. The dark mounds of sand were difficult to break up and required manual removal.

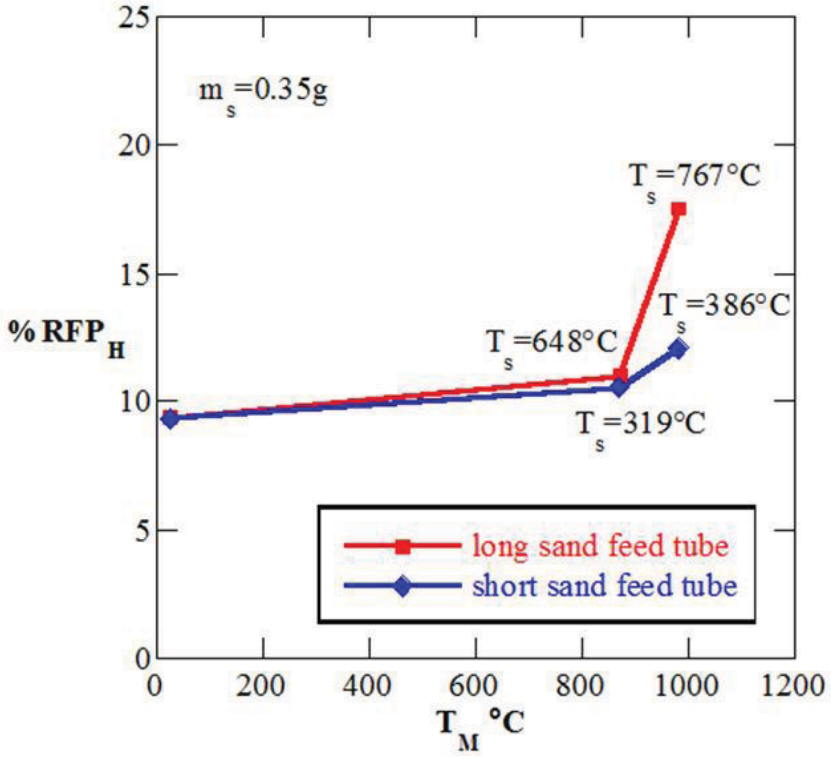

Figure 1.17. Blockage associated with varied metal and entering sand temperatures for L1 at a fixed coolant temperature of T_c=649°C and PR=1.03.

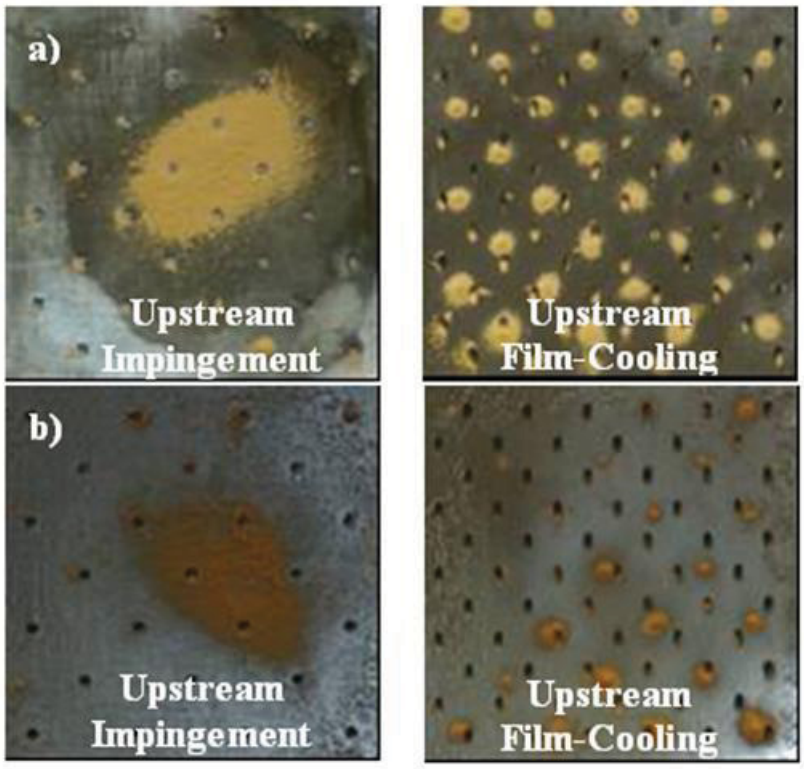

Figure 1.18. Post-test images of elevated temperature sand deposition patterns for L1 at T_M=982°C, T_c=649°C and PR=1.03 having two entering sand temperatures a) T_s=386°C b) T_s=767°C.

Conclusions

The effects of sand flowing through a combined impingement and film-cooling double wall liner have been presented. Pressure ratio across the liner, sand amount, metal temperature, and sand temperature were used to evaluate four realistic liner geometries. The four liners were designed to investigate what effect the cooling hole diameter, number of cooling holes, total coolant flow area, and relative alignment between the impingement and film-cooling holes had on blockage levels. The study was divided into two sections: ambient and engine representative temperature results.

For all liner geometries tested at ambient conditions, an increasing pressure ratio resulted in an increase in blockage. Since raising the pressure ratio resulted in an overall increase in fluid velocity, it was hypothesized that the increasing deviation of particles from fluid streamlines, described by the Stokes number, resulted in more wall collisions and therefore higher deposition rates. It was found that blocking levels scaled directly with impingement plate area at ambient conditions. At ambient conditions, the liner with the largest impingement flow area exhibited the

lowest blocking for all pressure ratios. Each double wall liner design also had a matched diameter of impingement and film-cooling holes, causing the impingement plate to act as a particle filter for the film-cooling plate. It was also observed that particles small enough to travel through the impingement holes subsequently impinged on the upstream side of the film-cooling plate. This impingement broke the particles up, allowing them to more easily pass through the film-cooling holes. Because of the particle breakup and filtering by the impingement plate, negligible buildup of sand was observed within the film-cooling holes or on the upstream surface of the film-cooling plate at ambient conditions.

At elevated temperatures, blocking levels did not scale with impingement area. The amount of blocking increased for all liners as metal temperature was increased. This was found to be a result of the sand becoming sticky at higher temperatures thus increasing the probability of particle deposition. Visual inspection of the liner after testing confirmed that the sand was becoming sticky, which resulted in elevated deposition levels on the upstream side of the film-cooling plate and within the film-cooling holes. This effect was quite different than at ambient conditions, where no sand buildup was observed on the upstream surface of the film-cooling plate. Since sand was depositing in small mounds on the upstream surface of the film-cooling plate downstream of the impingement jets, it was determined that liners with a high amount of overlap between the impingement and film-cooling holes blocked more when compared with staggered impingement and film-cooling holes.

Overall, the liner with the largest impingement flow area and least overlap between the impingement and film-cooling holes exhibited the lowest blocking overall at both ambient and heated conditions. At all operating conditions, the impingement holes were acting as a particle size filter for the film-cooling plate. This study has shown that impingement could be used to breakup larger particles thereby reducing their possibility of blocking within subsequent cooling geometries. In addition, the cooling liners with staggered film and impingement holes were found to be less sensitive to the sand depositing on the upstream side of the film-cooling plate, which occurred at higher temperatures.

Acknowledgements

This research was conducted through funding provided by Pratt & Whitney. The authors graciously acknowledge this support.

Nomenclature

General

A	cross sectional area
d	particle diameter
D	cooling hole diameter
FP	flow parameter, $FP = \left(\dot{m}_{hole}\sqrt{T_c R}\right)\Big/\left(P_{exit}A_{hole}\right)$
L	length
L_c	characteristic flow length
m	mass
$\dot{m}$	mass flow rate
n	number of holes
P	pressure
P_1	pitchwise hole spacing
P_2	streamwise hole spacing
PR	liner pressure ratio, $PR = P_{0C}/P_{exit}$
Q	volumetric flow rate
R	air gas constant
RFP	reduction in flow parameter at ambient conditions, $RFP = \left(FP_0 - FP_B\right)/FP_0$
RFP_H	reduction in flow parameter at heated conditions, $RFP = \left(FP_{0H} - FP_{BH}\right)/FP_{0H}$
St	Stokes number, $St = \tau_p/\tau_f$
T	temperature
U	velocity
u	uncertainty

Greek

ρ	density
μ	dynamic viscosity
τ_f	characteristic flow time scale, $\tau_f = L_c/U$

τ_s	characteristic sand response time, $\tau_s = \left(\rho_s d_s^2\right) / \left(18\mu_f\right)$

Subscripts

0	equivalent unblocked parameter at the blocked pressure ratio, ambient conditions
0H	equivalent unblocked parameter at the blocked pressure ratio, heated conditions
0C	coolant total property
amb	ambient laboratory conditions
B	blocked at ambient conditions
BH	blocked at heated conditions
c	coolant
exit	film-cooling hole exit
FC	film-cooling
hole	related to a single cooling hole
H	evaluated at heated conditions
I	impingement
M	metal
s	sand

References

1. United States Department of Defense. 2006]; Available from: http://www.defenselink.mil/transformation/.
2. Chambers, J.C., 1985, "The 1982 Encounter of British Airways 77 with the Mt. Galuggung Eruption Cloud," AIAA Paper. 85-0097.
3. Airline Pilot Magazine, 1990, 59, 6, June/July.
4. Mitchell, H.J. and Gilmore, F.R., Dust Cloud Effects on Aircraft Engines: Emerging Issues and New Damage Mechanisms, Research/Development Associates: Palo Alto, CA.
5. Smith, W.S., 1985, "Internation Efforts to Avoid Ash Clouds," AIAA Paper. 85-0101.
6. Campbell, E.E. 1994, "Recommended Flight-Crew Procedures if Volcanic Ash is Encountered. " in Volcanic Ash and Aviation Safety: Proceedings of the First International Symposium on Volcnaic Ash and Aviation Safety. Seattle, WA: Geological Survey Bulletin.
7. Coons, S., Private communication regarding the operation of helicopters in particle laden environments. 2006.

8. Batcho, P.F., et al., 1987, "Interpretation of Gas-Turbine Response Due to Dust Ingestion," Journal of Engineering for Gas Turbines and Power-Transactions of the Asme. 109(3): p. 344-352.

9. Dunn, M.G., et al. 1987, "Operation of Gas Turbine Engines in Dust-Laden Environments. " in Proceedings of the 69th Propulsion and Energetics Symposium. Paris, France.

10. Dunn, M.G., et al., 1987, "Performance Deterioration of a Turbofan and a Turbojet Engine Upon Exposure to a Dust Environment," Journal of Engineering for Gas Turbines and Power-Transactions of the Asme. 109(3): p. 336-343.

11. Kim, J., et al., 1993, "Deposition of Volcanic Materials in the Hot Sections of Two Gas Turbine Engines," Journal of Engineering for Gas Turbines and Power. 115(3): p. 641-651.

12. Weaver, M.W., et al. 1996, "Experimental Determination of the Influence of Foreign Particle Ingestion on the Behavior of Hot-Section Components Including Lamilloy. " in Proceedings from the ASME Turbo Expo. Birmingham, England.

13. Tabakoff, W., et al., Test facility for material erosion at high temperature. Discussion. 1979, Philadelphia, PA, ETATS-UNIS: American Society for Testing and Materials. 13.

14. Tabakoff, W., et al., 1995, "High-Temperature Coatings for Protection against Turbine Deterioration," Journal of Engineering for Gas Turbines and Power. 117(1): p. 146-151.

15. Walsh, P.N., et al., 1995, "Coatings for the Protection of Turbine Blades From Erosion," Journal of Engineering for Gas Turbines and Power. 117(1): p. 152-155.

16. Tabakoff, W. and Simpson, G. 2002, "Experimental Study of Deterioration and Retention on Coated and Uncoated Compressor and Turbine Blades. " in AIAA Aerospace Sciences Meeting and Exhibit. Reno, NV, USA.

17. Hamed, A.A., et al., 2005, "Turbine blade surface deterioration by erosion," Journal of Turbomachinery. 127(3): p. 445-452.

18. Jensen, J.W., et al., 2005, "Simulated land-based turbine deposits generated in an accelerated deposition facility," Journal of Turbomachinery. 127(3): p. 462-470.

19. Bons, J.P., et al., 2001, "The many faces of turbine surface roughness," Journal of Turbomachinery. 123(4): p. 739-748.

20. Hamed, A., et al., 2006, "Erosion and deposition in turbomachinery," Journal of Propulsion and Power. 22(2): p. 350-360.

21. Shah, A. and Tafti, D.K., 2007, "Transport of particulates in an internal cooling ribbed duct," Journal of Turbomachinery. 129(4): p. 816-825.

22. Walsh, W.S., et al. 2006, "Effects of Sand Ingestion on the Blockage of Film-Cooling Holes. " in Proceedings of the ASME Turbo Expo. Reno, NV.

23. Hill, P. and Peterson, C., Mechanics and Thermodynamics of Propulsion (2nd Edition). 1991, Reading, MA: Prentice Hall.

24. Crowe, C., et al., Multiphase Flows with Droplets and Particles. 1998, Boca Raton, FL: CRC Press LLC.

25. Figliola, R.S. and Beasley, D.E., Theory and Design for Mechanical Measurements. 2006, Hoboken, NJ: John Wiley and Sons Inc.

26. Land, C.L., et al. 2008, "Considerations of a Double Wall Cooling Design to Reduce Sand Blockage. " in Proceedings of the ASME Turbo Expo. Berlin, Germany.

27. Tu, J.Y., et al., 2004, "A study of particle rebounding characteristics of a gas-particle flow over a curved wall surface," Aerosol Science and Technology. 38(7): p. 739-755.

Paper 2: A Method for Identifying and Visualizing Foreign Particle Motion Using Time Resolved Particle Tracking Velocimetry

Cardwell, N.D., Vlachos, P.P., Thole, K.A., 2009, "A Method for Identifying and Visualizing Foreign Particle Motion Using Time Resolved Particle Tracking Velocimetry," International Gas Turbine and Aeroengine Congress and Exposition, Orlando, Florida, ASME Paper GT2009-60273.*

Cardwell, N.D., Vlachos, P.P., Thole, K.A., 2011, "A Method for Identifying and Visualizing Foreign Particle Motion Using Time Resolved Particle Tracking Velocimetry," Journal of Turbomachinery, Volume 133, Issue 2, DOI:10.1115/1.4001187.*

[Chapter reprinted with kind permission from ASME Journals]

Abstract

Gas turbines for aircraft are designed for operation with a clean inlet air flow. This ideal operational condition is often violated during take-off and landing, where the probability of particle ingestion is high with sand and dirt being the most commonly observed foreign particles. Current research on particle ingestion has identified several mechanisms that contribute to performance degradation in the turbine: erosion of internal and external surfaces; and flow blockages of film-cooling holes and internal cooling passages. The focus of the study given in this paper is to present a method that identifies the motion of foreign particles within an internal ribbed passage. The method uses a high-resolution, flowfield interrogation method known as Time-Resolved Digital Particle Image Velocimetry (TRDPIV). Observations from the two-phase flows showed that particle collisions occurred more frequently on the upstream surface of the ribs, especially in the inlet region. Results from these collisions included substantial particle breakup and a particle rebounding phenomenon between the upper and lower walls. Comparisons are made to LES predicted particle trajectories indicating some agreement, but also phenomena that are not predicted due to the inherent assumption of the modeling.

*Co-authors: Dr. Pavlos P. Vlachos, Mechanical Engineering Department, Virginia Tech
Dr. Karen A. Thole, Mechanical and Nuclear Engineering Department, Penn State

Introduction

Two-phase flows characterized by solids in an air stream are found in many engineering processes such as filtration systems, fluidized beds, and solid fuel combustors. Gas turbines are not designed for operation with such a gas-solid flow. These engines are well-suited for applications requiring large power output in comparison to the size and weight of the engine. They are utilized for a wide variety of purposes including tank propulsion, electrical power generation, and the propulsion of aircraft. As a result, gas turbines are often operated in environments with a high probability of particle ingestion, most commonly sand and dirt.

Figure 2.1 shows several instances of gas turbines being operated in particle laden environments. Complete filtration of the intake air is often deemed infeasible due to the associated high pressure drop, replacement and cleaning requirements for the filters, and an overall increase in the engine weight and size. Particle ingestion into a gas turbine can have serious effects on both performance and engine service intervals. While traveling through the main-gas path, ingested debris collides with and subsequently erodes the metal surfaces. These particles, which are also pulled into the coolant air bypass, clog internal cooling channels thereby reducing mass flow and increasing part temperature. Elevated temperatures within the engine make the sand tacky, further increasing the likelihood of deposition and blocking within cooling channels. Deposited sand adds additional conductive resistance to heat transfer between the coolant and metal.

Figure 2.1. Gas turbines operated in dusty environments. (www.militaryphotos.net, 2007, used under fair use)

Numerous analytical models have been developed that attempt to predict particle motion in a dispersed solid-gas flow. Researchers developing flow models for isotropic homogeneous turbulent two-phase flows have encountered significant difficulties expanding their predictions to more complicated wall bounded flowfields, such as those found in turbine cooling channels.

This is due to an inability to correctly model realistic turbulent particle transport as well as the effects of inter-particle and wall collisions. More advanced knowledge of the particle motion and carrier flowfield will aid in increasing the fundamental understanding of how particles are transported by a highly turbulent, wall-bounded flow.

Relevant Past Studies

Numerous rib roughened studies for airfoil cooling applications are reported in the literature with the focus being on heat transfer. Only a limited number of experimental studies have sought to resolve the mean and turbulent flow fields of a fully rib-roughened channel. The past studies review begins with previous research focusing on single phase rib channel flowfields. It is followed by a review of experimental and computational studies on multiphase channel flow. The last section presents a brief sample of research performed on multiphase flows using Particle Image Velocimetry (PIV).

Rib Channel Studies

An early work by Perry et al. [1] studied the effect of rib roughness on turbulent boundary layer flow. They showed that the effective roughness of spanwise grooves could be characterized by either the roughness height, k, or the boundary layer thickness, d. More recent experimental studies on rib roughened channel flow have been performed by Liou et al. [2], Casarsa et al. [3], Graham et al. [4], and Sewall et al. [5]. Using laser Doppler velocimetry (LDV), Liou et al. [2] studied a fully roughened rectangular channel with vertically aligned roughness elements. Their research showed that the separated shear layer growth and reattachment length were markedly different than for a geometrically similar backward facing step. The rib channel study by Casarsa et al. [3] compared time-averaged DPIV flowfields with the wall heat transfer, measured by liquid crystal thermography. Regarding the flowfield, their study identified four regions of flow separation in addition to evidencing the three dimensional behavior of the channel flowfield near the side walls. Graham et al. [4], for a fully roughened channel with aligned ribs, evaluated the effect of rib height for a fixed rib pitch. Using LDV and pressure drop measurements, they concluded that increasing rib height resulted in a larger recirculation region between successive ribs thus explaining the trend of decreasing inter-rib heat transfer as observed by other researchers. Graham et al. [4] also observed that the required

development length for a fully roughened channel was approximately 10 rib pitches for their configuration, which was larger than values previously reported by other researchers. Despite a number of experimental studies on aligned rib roughness elements, few studies have focused on the effects of staggered rib elements.

Numerous computational studies have been performed on rib roughened channel geometries, such as those by Cui et al. [6], Wahab and Tafti [7], and Sewall and Tafti [8]. Cui et al. [6] utilized a large eddy simulation (LES) to further explore the effect of rib spacing for channel flow having a single rib roughened wall. For closely spaced ribs, the mean outer flow was observed "riding" over the roughness elements with a separated vortex contained between each rib pair. With the larger rib spacing, reattachment occurred between subsequent ribs and large vortices were identified within the core flow through qualitative observations of the instantaneous velocity vector fields. A thorough review of the contributions and difficulties in simulating roughened channels was provided by Patel [9]. Recent numerical studies are beginning to rely on LES and Direct Numerical Simulations (DNS) to more accurately resolve the flow field than previous studies utilizing the Reynolds-Averaged Navier-Stokes equations (RANS).

Multiphase Channel Flow Studies

One of the current issues with computational simulations of multiphase flow derives from the difficulties in modeling interparticle and wall collisions. Traditionally, these collisions are treated as ideal reflections with no loss of inertia. In 1992, Sommerfeld [10] published an initial study on the computational modeling of a two-phase flow in a vertical channel. The only experimental data with which Sommerfeld could compare to was published in 1975 by Grant and Tabakoff [11]. Grant and Tabakoff used their accelerated erosion facility to study particle impacts in a model compressor stage. A high speed camera was utilized to visualize the particles as they traveled through the cascade. Sommerfeld [10] used images showing wall collision events to compare several different computational bouncing models. From his study, Sommerfeld concluded that numerical simulations of a confined gas-solid flow require a detailed modeling of particle-wall collisions including effects of wall geometry and particle shape. He also asserted a need for "detailed experiments that take into account the combination of particle and wall material and the roughness of the wall".

Another numerical study for a square channel was performed by Shah and Tafti [12]. The square channel computational domain was periodic in the streamwise direction having a flow Reynolds number of 20,000. Their channel also included square ribs aligned on the top and bottom walls. Spherical particles were introduced into the flow having diameters of 10 and 100 μm. The 10 μm were shown to be more sensitive to flow structures which was related to their relatively low Stokes numbers when compared to the 100 μm particles. Particle impacts on the rib surfaces were evenly distributed and impacts on the side walls were preferentially concentrated in the region of the top and bottom ribs. This even impact distribution was not true for the 100 μm particles, which showed a tendency to impact the upstream surface of the rib as well as the reattachment region behind the rib. They also noted a significant clustering of particles in the near wall region as indicated by 26% of the 50 μm and 100 μm particles within $0.05D_h$ of the channel walls.

Multiphase Particle Image Velocimetry (PIV) Studies

Digital Particle Image Velocimetry (DPIV) can provide full-field velocity measurements for both the carrier phase as well as the particle phase. Given a sufficiently high flow sampling rate, spatio-temporal resolved particle and fluid velocities can be readily calculated for the entire flowfield. In 1996, Jakobsen et al. [13] used DPIV to investigate time-averaged properties in a vertical channel solid-gas flow. Oil droplets and glass spheres were used to seed the flow with nominal diameters of 1 μm and 50-200 μm, respectively. Slip velocities for the large particles were found to increase with particle Stokes number and fine wakes behind these particles were observed in the carrier fluid. Lui et al. [14] studied a vertical wake flow in a confined rectangular channel for the mixing of two liquid phases. The results were then compared to an analytical model and two theoretical diffusion and dissipation models. The theoretical predictions were found to agree somewhat with the experimental data in an averaged sense but did not properly model the interaction between the two fluids. These works are an example of the current capabilities of DPIV to provide physical insight into two-phase flow interactions.

Summary and Objectives

To date, there have been no detailed DPIV measurements made in a rib roughened channel with a two-phase flow. Moreover, there have been no time-resolved measurements

made whereby particle trajectories can be determined. The objective of this paper is to present a methodology for measuring the flowfield and also measuring the particle flows for a ribbed channel. In addition, this methodology includes the capability of independent, time-resolved measurements for both phases of the flow. Observed particle trajectories will be compared with those indicated through computational simulations to determine where similarities and differences occur and where improved modeling is needed. It is important to note that the two flow phases, carrier flow and sand, were not resolved simultaneously.

The remainder of this paper discusses the experimental rib channel geometry and time-resolved DPIV (TRDPIV) facility and experimental methods; and also provides qualitative comparisons of the single phase and two-phase rib channel results with the literature.

Experimental Facility and Measurement Methods

For these measurements, a commonly used ribbed channel with staggered ribs was used for the TRDPIV measurements. Because both the facility and measurement method were new, benchmarking needed to be completed. This section describes the rib roughened channel geometry, the testing facility, the TRDPIV system, and data processing methodology for both the clean and particle-laden channel flows.

Staggered Rib Channel Geometry and Test Facility

The rib roughened channel used for this study, as shown in Figure 2.2, was designed to simulate an internal cooling channel for a turbine airfoil. As shown in Figure 2.2 and Figure 2.3, the experimental channel has both a smooth and rib roughened section. The inlet section was $12D_h$ long and was made up of a smooth wall to assure a fully developed and uniform inlet flow into the rib roughened section. Note that a scale of six times larger than the engine was chosen for the single phase flowfield measurements which allowed for improved measurement resolution for comparisons with published literature. For the two-phase channel studies, the ribbed channel was at actual engine scale to maintain the correct sand to channel geometric relationship. A summary of relevant channel dimensions are given in Figure 2.3 and Table 2.1 for the engine scale as well as the scaled up experimental geometry. Each channel section was manufactured primarily from acrylic, having exactly the same geometry with the only differences being the construction material used for the ribs. The use of acrylic allowed for full

laser and optical access to any area of the test channel. Within the rib roughened section, transverse spanwise ribs were placed 90° to the main channel flow and were staggered when comparing the upper and lower walls, as shown in Figure 2.3. The engine scale ribs were constructed with small brass square rod and the scaled up ribs were constructed of acrylic.

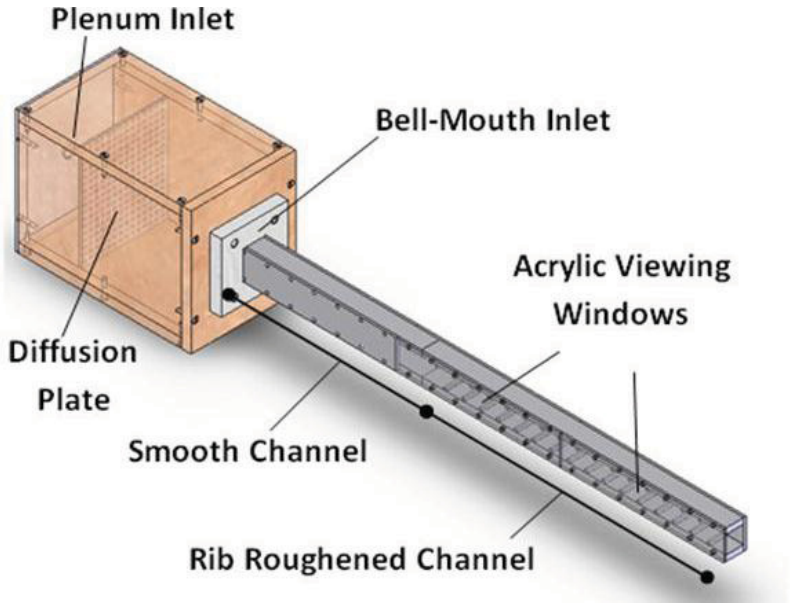

Figure 2.2. Illustration of the rib channel.

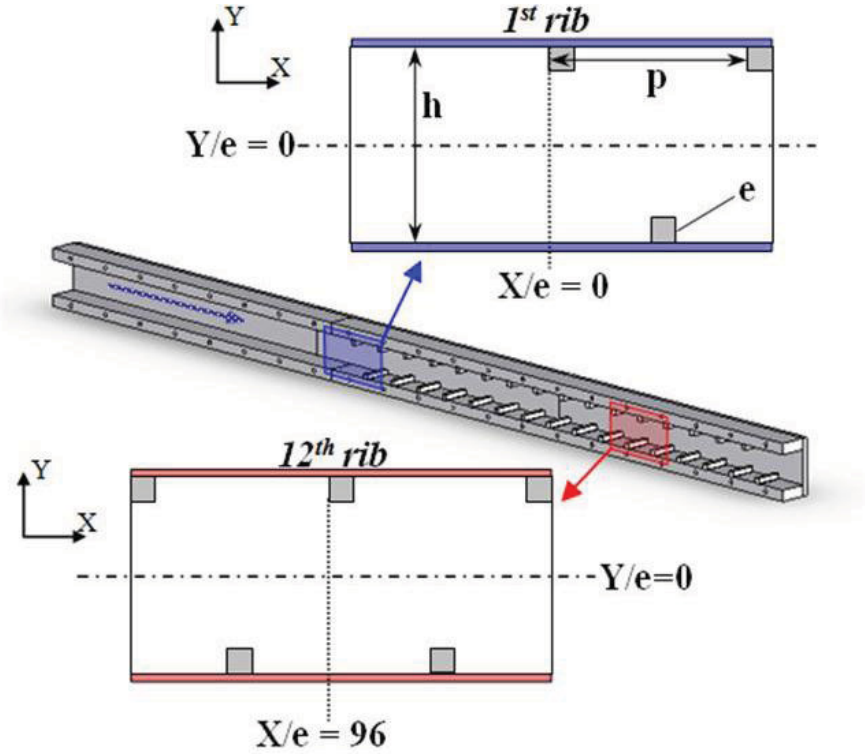

Figure 2.3. Section view of the inlet (1st rib) and developed (12th rib) measurement planes.

The coordinate system, also shown in Figure 2.3, was defined based on the channel centerline and upstream face of the 1st rib on the top wall. As with all other channel parameters, the staggered rib geometry was chosen as it matches with what is commonly seen within the engine and the published literature.

High pressure, room temperature air was supplied as coolant to the test channel. This air was distributed to the lab by an auxiliary compressor facility at approximately 550 kPa. A gate valve, situated far upstream of the plenum inlet, was used to control and regulate coolant flowrate. The total coolant flowrate to the channel was measured upstream of the plenum inlet by measuring pressure drop across a laminar flow element (LFE). The LFE had a maximum flowrate capacity of 1.2 m^3/s and a measured flowrate uncertainty of ±0.5%. Flowrate requirements for the channel ranged from 0.1-0.7 m^3/s. A Validyne DP-103 differential pressure transducer was used to measure the pressure drop across the LFE.

After passing through the LFE, the flow entered a plenum having a 40:1 area ratio compared to the channel flow area. Within the plenum the coolant flow passes through a round-hole diffusion plate having a closed to open area ratio of 4:1. After passing through the diffusion plate, the coolant entered the channel section through a bell-mouth inlet to assure a smooth and uniform inlet flow.

Table 2.1. Rib and Channel Geometric Parameters

	Engine Scale Model	6X Experimental Model
Height (h)	0.64cm	3.8cm
Aspect Ratio	1	1
e/D_h	0.12	0.12
p/e	8	8
p/D_h	1	1
rib angle	90°	90°
Re	2.5k, 10k	2.5k, 10k, 20k

Measurement Method for Flow and Particle Trajectories

Time Resolved Digital Particle Image Velocimetry (TRDPIV) is a non-invasive flowfield measurement technique which provides spatio-temporal resolved velocity field measurements. Shown in Figure 2.4, the TRDPIV system included the following components: fluid tracing

particles uniformly seeded within the flow, a high power pulsing laser to illuminate the particles, optics for laser manipulation, and a high speed digital camera to capture the motion of the fluid tracing particles.

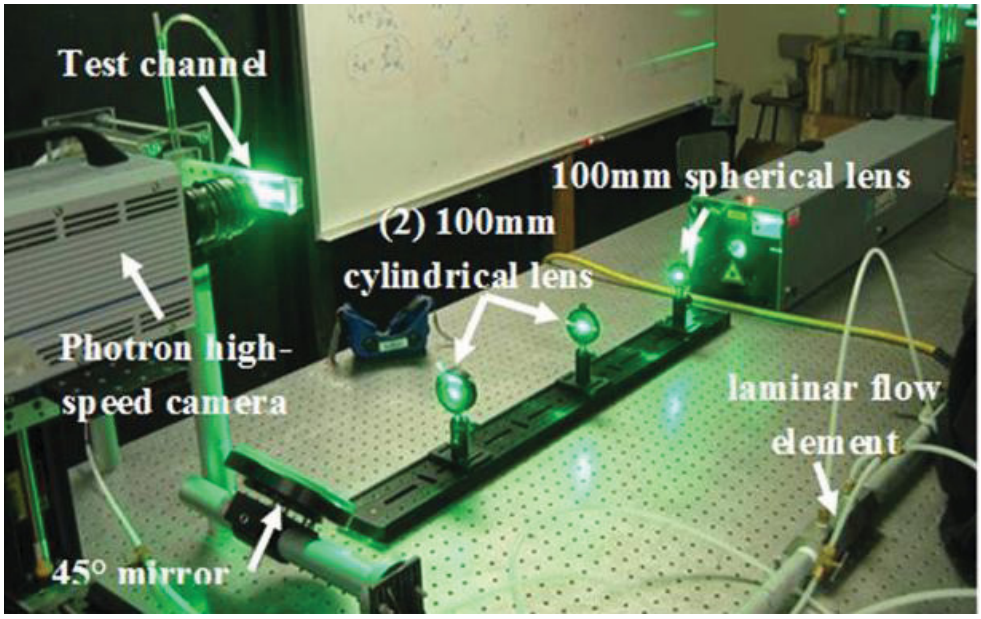

Figure 2.4. TRDPIV experimental setup.

For this study, a LaVision liquid atomizer was used to seed the air (coolant) flow with ~ 1 μm diameter alcohol droplets. Roughly spherical in size, the alcohol particles had a calculated Stokes number << 1. The Stokes number is defined as the ratio of particle relaxation time, τ_p, and the characteristic time scale of the flow, τ_f. When St << 1, it is assumed that the particle responds to flow fluctuations almost perfectly and therefore has a slip velocity of zero. A St >> 1 indicates that particle inertia is sufficiently high in relation to the flow influence that its trajectory is relatively unaffected by the flowfield [15]. As will be discussed later, the Stokes number range for the sand particles, in contrast to the flow seeding, ranges from St=0.002 to St= 2,000 which fully encompasses the realistic range of particle behavior from St<<1 to St>>1.

Illumination of the seeding particles was accomplished using a high power pulsing laser. A coherent light source is typically used for TRDPIV as it provides a means to investigate a particular region of the flowfield by illuminating the seed particles well above the level of background (diffuse) light. For the current study a 20W New Wave dual-head Pegasus laser was used for this purpose. The Pegasus laser has a maximum pulsing frequency of 20kHz, making it optimally suited for TRDPIV. As shown in Figure 2.5, the laser beam was manipulated into a

very thin (<1 mm) two-dimensional plane through the use of lenses and mirrors and then passed vertically through the channel's lower wall. The streamwise location of the laser plane defined the region of TRDPIV interrogation, which for this study was $2.1D_h$ streamwise by $1D_h$ spanwise, centered at the inlet and developed regions of the channel at the 1st and 12th rib, respectively.

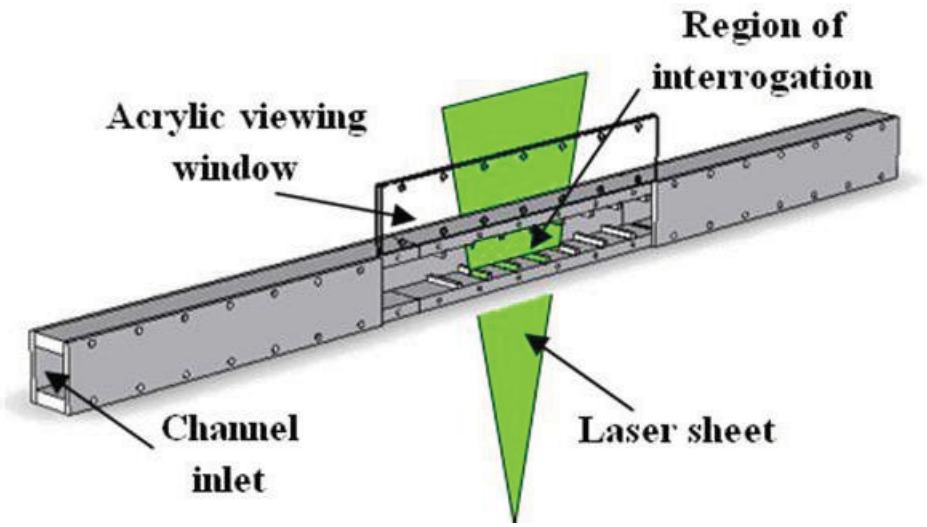

Figure 2.5. Illustration of a laser sheet being passed through the lower channel wall.

Recording of the tracer motion within the region of interrogation was accomplished using a high speed digital camera. Placed normal to the laser sheet, the camera recorded images of the fluid tracers at precisely controlled time intervals. Given this history of the fluid tracer motion, the associated channel flowfield may then be computed from the inter-frame flow tracer displacement using standard TRDPIV correlation techniques. For this study, a Photron Ultima APX-RS high speed digital camera was used having a maximum frame rate of 6000fps at 1024x1024 pixel resolution. Since the region of interrogation has an aspect ratio of 2.1:1, the camera resolution was reduced to 1024x464 to maximize the total number of frames that could be acquired in a single test.

Additional equipment employed in the study included a central data acquisition PC and Integrated Design Tools timing hub, which were used to control the laser and camera sampling frequencies. A Tektronics TDS 2014 oscilloscope was also used to monitor synchronization of the camera and laser timing signals.

The next step in TRDPIV is analysis of the captured particle images. The most commonly used method to analyze these types of images in the Standard Cross Correlation

Technique (SCC). After sectioning each image into individual correlation windows the SCC method utilizes a Fast Fourier Transform (FFT) between each image pair to measure particle displacement within each window [16-18]. A significant body of research has been performed exploring different correlation methods which seek to improve the accuracy and fidelity of TRDPIV measurements, but a review of these contributions is well beyond the scope of this paper. Herein we use a new technique, termed Robust Phase Correlation (RPC) by Eckstein and Vlachos [19] which improves upon the SCC by employing optimum spectral filtering based on a generalized cross-correlation. The method has been shown to increase measurement accuracy while reducing peak-locking. Supporting the results of Eckstein and Vlachos [19], significant improvements in valid vector detection and measurement accuracy were observed for the present rib channel experiment when using the RPC technique versus the SCC technique (data not shown). Therefore all processing was performed with the RPC using the parameters in Table 2.2.

Table 2.2. TRDPIV Processing Parameters

	1st Pass - RPC 2nd Pass - RPC
1st pass correlation window	64x32 (pixels)
2nd pass correlation window	32x16 (pixels)
grid spacing	4x4 (pixels)
measurement overlap	50% x 25%
number of vectors	241x111
flow samples per test	6000
flow sampling frequency	1500 Hz

Utilizing the above described facilities and measurement methodologies, two different experiments were performed to quantify the channel flowfields. The first experiment sought to highly resolve the single phase channel flowfield using TRDPIV. Therefore, the scaled up channel geometry was used having the flow seeded only with 1 μm alcohol flow tracers. The aim of the second experiment was to investigate a two-phase channel flow, with emphasis on the trajectories of larger particles. To accomplish this, three different types of sand were fed into the engine scale channel and their motion was recorded using the TRDPIV system. As a note, future studies will look at combing the two experiments, thereby simultaneously resolving both the coolant particle flows and particle trajectories.

Sand Characterization and Delivery

For the two-phase flow experiment, three different sand types were tested: ISO Coarse, Arizona Road Dust (AzRD), and sieved AzRD. To create a distribution of larger particles, the AzRD particles above 100 μm were separated using dry standard sieving practices to be used for the large diameter sand testing. All sands have the same basic chemical composition, primarily crushed quartz. The analysis of each of the sand samples agree with the manufacturer's specification stating that they contains different phases of quartz (SiO_2) up to approximately 68-76%. The other major constituent is aluminum oxide (Al_2O_3) between 10-15%, with traces of iron oxide (Fe_2O_3), sodium silicate (Na_2O), lime (CaO), magnesium oxide (MgO), titanium dioxide (TiO_2), and potassium oxide (K_2O), in descending concentration.

Despite their similar compositions, each test-sand had a significantly different size distribution. Shown in Figure 2.6 are the three sand size distributions tested for the two-phase channel flow experiments. A Horiba LA-950 particle size analyzer was used to measure the sand size distribution, having a reported accuracy of ±1% of the measurement size (±1 nm at 0.1 μm and ±10 μm at 1000 μm). As a quick reference, Table 2.3 indicates the mean, minimum, and maximum sand diameter of each test-sand. Also shown in Table 2.3 are the calculated Stokes numbers of the particles based on the rib height and bulk channel velocity.

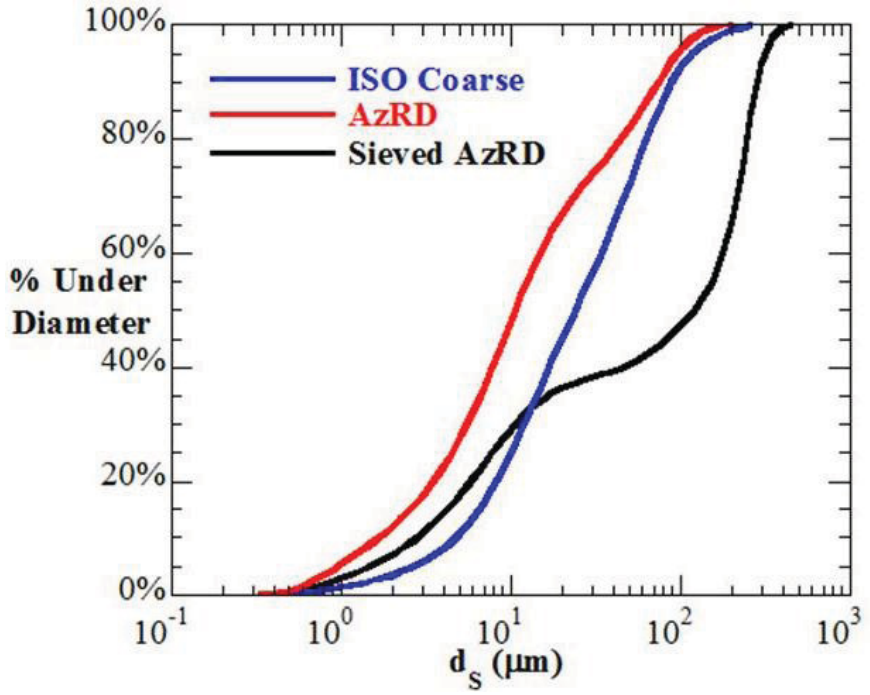

Figure 2.6. Size distributions for the test-sands obtained by a Horiba LA-950.

Particle mass loading was set to a value of 0.8, which was identified by Walsh et al. [20] as sufficient to generate engine representative blocking levels in simulated cooling geometries. Particle mass loading is defined in the nomenclature as the ratio of dispersed phase mass flow rate to the mass flow rate of the carrier fluid. This is also referred to as mass concentration ratio.

Dispersion of the AzRD was accomplished at the inlet to the smooth channel using a gravity-feed system, which was calibrated to provide to appropriate mass loading. The sand was injected tangentially to the flow at the bell mouth inlet. Acceleration and dispersion of the sand occurred throughout the smooth channel inlet, which was driven by the turbulent flowfield in the channel.

Table 2.3. Physical Properties of Sands Tested

	sand diameter - μm		
	d_m / St_m	d_{min}/ St_{min}	d_{max}/ St_{max}
ISO Coarse	37 / 59	< 0.1 / 0.001	243 / 2550
AzRD	62 / 166	< 0.1 / 0.001	~1000 / 43,170
Sieved AzRD	193 / 1600	77 / 256	517 / 11,540

Discussion of Results

The results of this study are presented in two main sections: mean averaged TRDPIV results for single phase flow and for two-phase flow seeded with three different particle size distributions. For the single phase channel flow, TRDPIV results are compared to published LDV [4] and LES [5] data on similar geometries at Re=20,000. Results from the two-phase flowfield are qualitatively compared to a two-phase LES study. Some data presented in this paper was originally published in a more detailed TRDPIV study of the single phase channel flow experiment by Cardwell et al. [21] and is appropriately referenced when applicable.

Single Phase Rib Channel Flow – Mean Averaged

The fully developed and entry regions of the ribbed channel flows for Re = 20,000 are given in Figure 2.7 with contours of turbulent kinetic energy (TKE) overlaid with mean velocity stream traces. As a note, the blanked-out area in Figure 2.7a at X/e = -6, Y/e=-4 was deemed an inaccessible area resulting from the local channel construction. Below the full flow plane that

was measured is a close-up of the region indicated in Figure 2.7. For the entry region (Figure 2.7a) the mean approaching flow separates from the top of the first rib resulting in separated shear layer as evidenced by the high values of TKE just above the ribs and a large recirculating region between the 1st and 2nd ribs. This inter-rib recirculating region was located behind the first rib from X/e=1 to 5 and Y/e=2.4 to 4 and was bounded by the closing of the first rib separated shear layer. Reattachment of the separated region occurred just upstream of the second rib at X/e=6.5.

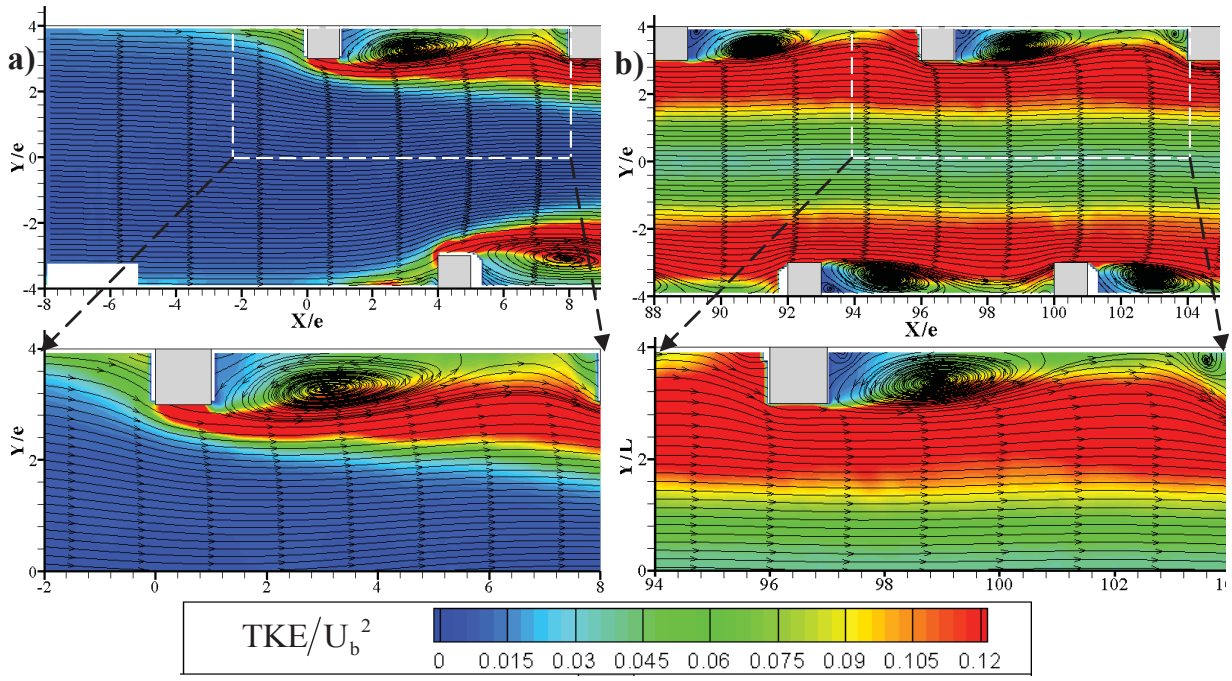

Figure 2.7. Contours of normalized turbulent kinetic energy overlaid with mean velocity streamtraces for Re=20,000 at the a) inlet and b) developed sections [21].

In the developed region (Figure 2.7b), the mean flowfield showed several important differences when compared to the inlet. Higher levels of TKE were observed throughout the flowfield with a much larger band of TKE above the ribs signifying a more energized and turbulent separated shear layer. Given the increased turbulence levels above the ribs, the inter-rib wake region closed faster with reattachment occurring at X/e=101. These results corresponded to a reattachment length of 6.5e at the inlet as compared with 5e in the developed section. A smaller recirculating region was also observed at just upstream of the 13th rib at X/e=102.7. The above described TRDPIV measured flowfields qualitatively agree with other published studies using other flowfield measurement techniques [4-6].

More specifically, Figure 2.8 and Figure 2.9 show direct comparisons of the mean velocity profiles derived from TRDPIV and profiles published by Graham et al. [4] using laser Doppler velocimetry (LDV) and Sewall et al. [5] using large eddy simulations (LES). The comparisons of mean streamwise velocity in Figure 2.8a and Figure 2.9a show good agreement between all three methods, both above the 12th rib and in the inter-rib region. Maximum streamwise velocity measured by TRDPIV was ~4% higher than the value measured by LDV and LES.

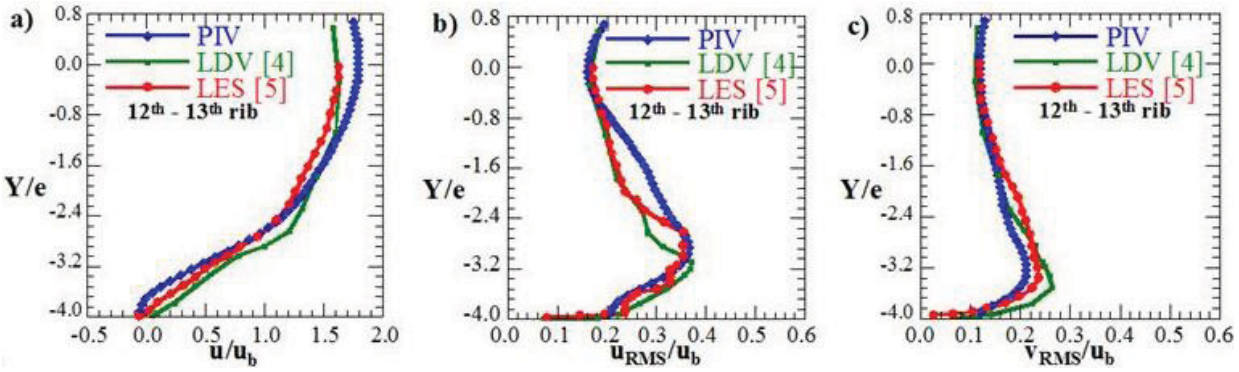

Figure 2.8. Comparisons in the inter-rib region of mean a) streamwise velocity b) streamwise velocity fluctuations c) spanwise velocity fluctuations between PIV, LDV, and CFD in the fully developed region at Re=20,000.

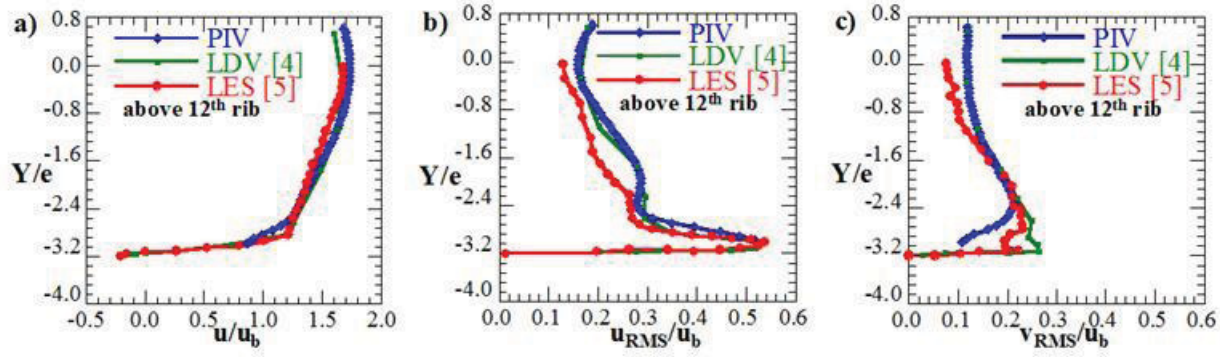

Figure 2.9. Comparisons above the 12th rib of mean a) streamwise velocity b) streamwise velocity fluctuations c) spanwise velocity fluctuations between PIV, LDV, and CFD in the fully developed region at Re=20,000.

Comparisons of streamwise velocity fluctuations in Figure 2.8b and Figure 2.9b also showed good agreement, with a maximum measured $u_{RMS}/u_b = 0.37$ at $Y/D_h=0.14$ in the inter-rib region and $u_{RMS}/u_b = 0.52$ at $Y/D_h=0.12$ above the 12th rib. Shown in Figure 2.8c and Figure 2.9c, the measured profiles of spanwise velocity fluctuations were also similar for all three

methods, with the reported TRDPIV values being slightly lower just above the 13th rib and near the channel wall in the inter-rib region. However, slight differences are to be expected since the studies by Graham et al. [4] and Sewall et al. [5] were performed on a channel with aligned ribs and the TRDPIV study presented was performed with a staggered rib array (see Figure 2.3). Ultimately, results for the three studies show close agreement and serve to confirm that the TRDPIV technique was accurately resolving the rib channel flowfield.

The TRDPIV method succeeded in fully resolving the unsteady rib channel flowfield in both space and time. Figure 2.10 shows the instantaneous flowfield and calculated vorticity magnitude for a single flow sample in the fully developed region. Vorticity is defined as the curl of the local velocity vector and is often related to the level of rotation present in the flow. The presence of a coherent flow structure, such as a vortex, is often evidenced by a region of high vorticity values. While a full, unsteady analysis of the rib channel flowfield is beyond the scope of this paper, it is useful to identify that the actual Stokes numbers of particles within the channel flow will vary considerably as they convect through the channel.

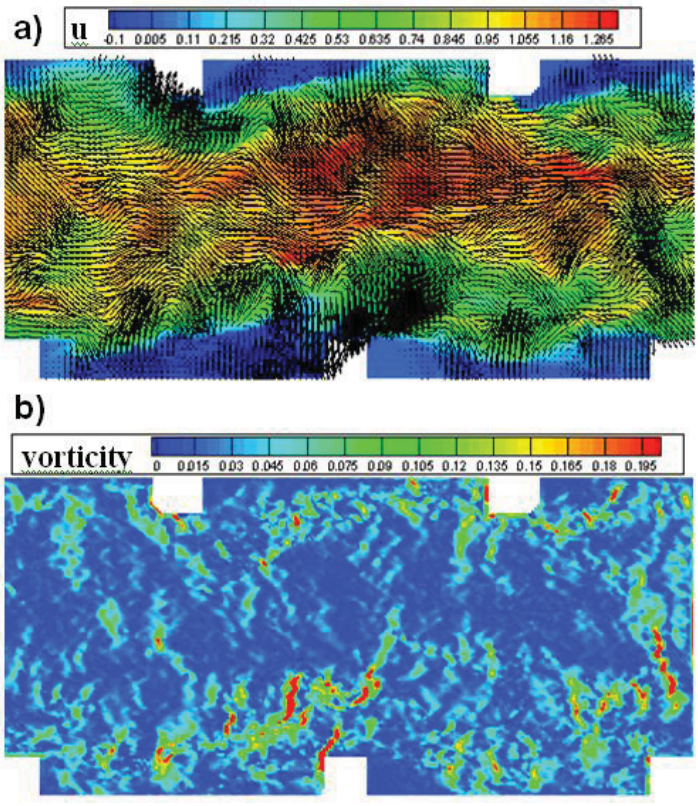

Figure 2.10. Instantaneous flow sample in the fully developed section for a). streamwise velocity magnitude and b). vorticity magnitude at Re=2500 [21].

Two-phase Rib Channel Flow

Each image shown in Figure 2.11-Figure 2.14 were exposed multiple times by the laser, resulting in particle streaks. The images in Figure 2.11, Figure 2.13, and Figure 2.14 were exposed 6 times and Figure 2.12 was exposed 4 times. The number of exposures per frame was adjusted to help visualize the particles better for different sand sizes. It is important to note that, for Figure 2.12, a minor synchronization error between the laser and camera caused some images to be exposed three or five times instead of the desired four laser pulses.

For all sand sizes, particles were observed traveling through the passage colliding with walls, rib surfaces, and each other. The ISO Coarse test dust, having a smaller range of sand diameters, most closely followed the mean flow direction, as shown in Figure 2.11. For these smaller diameter particles, fewer observed wall collisions occurred as compared with the larger diameter sand sizes.

Shown in Figure 2.12 the sieved AzRD was observed to be primarily inertially driven, a result of having a much higher mean particle diameter and therefore higher Stokes number. Inertially driven, or ballistic, particles have a higher tendency to follow their own particle paths and are only marginally influenced by the surrounding flows. The arrows shown in Figure 2.12 indicate the direction of the particles showing that the particles do move in a direction sometimes that opposes that of the mean flow direction.

The motion of unsieved AzRD could be described as a combination of ISO Coarse and Sieved AzRD since it has both a wide range of particle sizes and a relatively low mean particle diameter, as shown in Figure 2.13. It was also observed that particles can break up after a strong collision with the wall. Figure 2.14 shows a particle collision that occurred while testing with the unsieved AzRD at Re=20,000. This succession of images recorded the collision and subsequent breakup of a particularly large particle. The diameter of the particle was estimated to be approximately equal to the rib height and had a high slip velocity in relation to the smaller particles. Upon breakup, smaller fragments were observed to accelerate quickly into the channel flow while larger fragments accelerated slowly and maintained their trajectories longer. Recalling Figure 2.12, it was also shown that large particles colliding with the upstream rib surface occasionally rebound with sufficient velocity to travel upstream for several rib pitches until finally becoming re-entrained into the flow, as illustrated in Figure 2.15. It was therefore

inferred that the particle residence time within the cooling channel was much higher than the estimated fluid residence time, owing to the large number of rib and wall collisions.

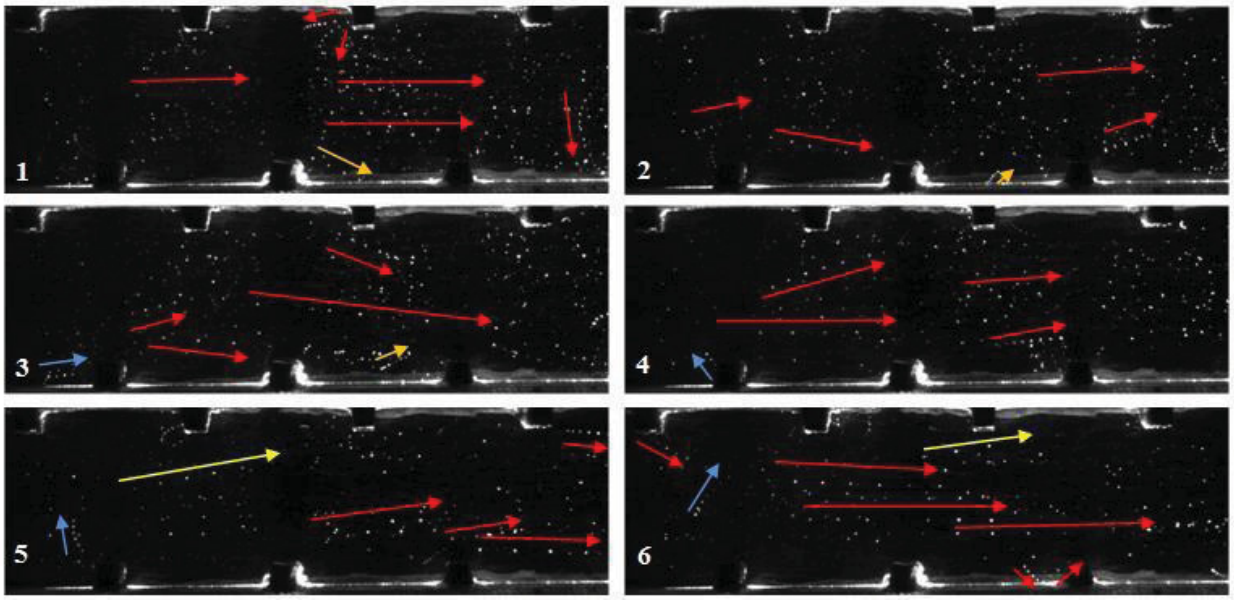

Figure 2.11. Succession of images illustrating particle motion of ISO Coarse test sand (d_{min}=0.1 µm, d_{max}=243 µm) at Re=20,000 (non-red arrows reflect particles located in multiple images).

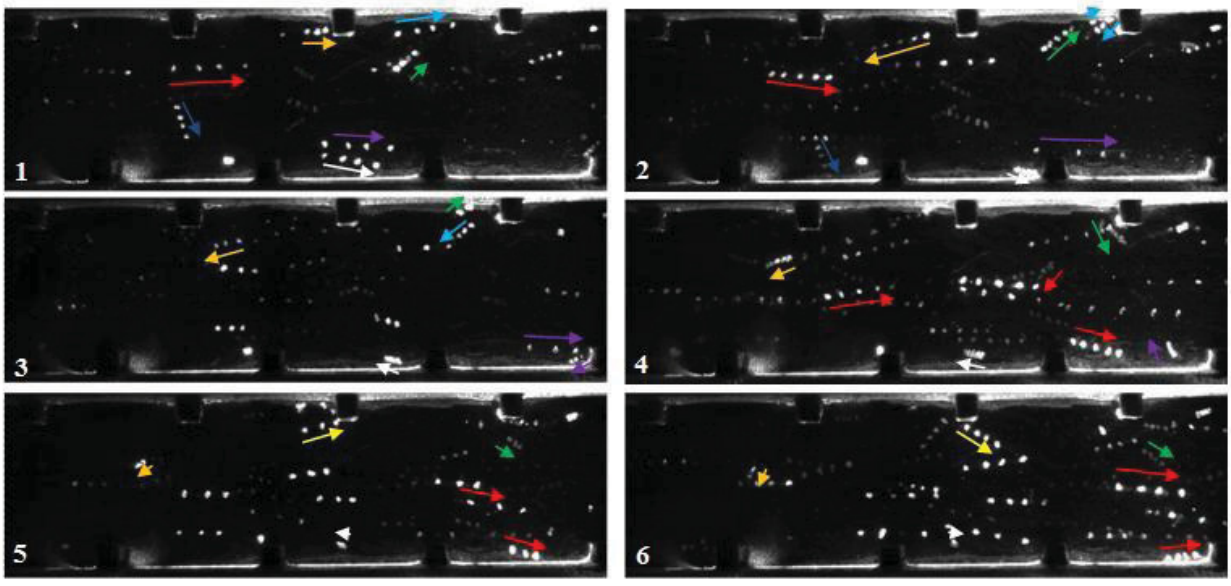

Figure 2.12. Succession of images with arrows illustrating particle motion of sieved AzRD (d_{min}=77 µm, d_{max}=517 µm) at Re=20,000 (non-red arrows reflect particles located in multiple images).

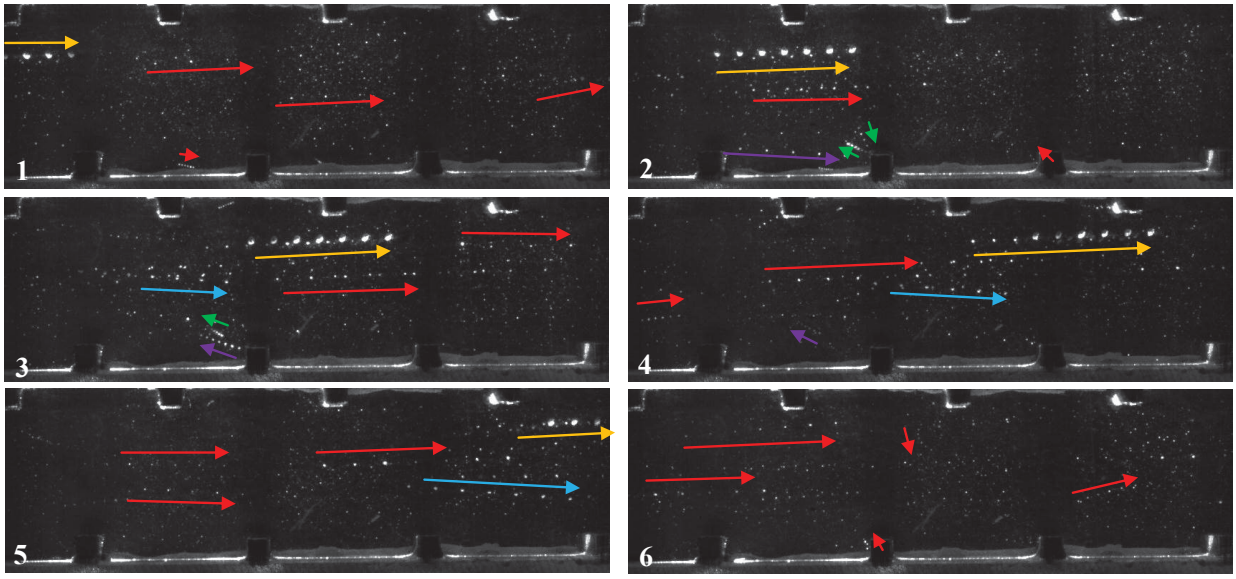

Figure 2.13. Succession of images illustrating particle motion of AzRD (d_{min}=0.1 μm, d_{max}=1000 μm) at Re=20,000 (non-red arrows reflect particles located in multiple images).

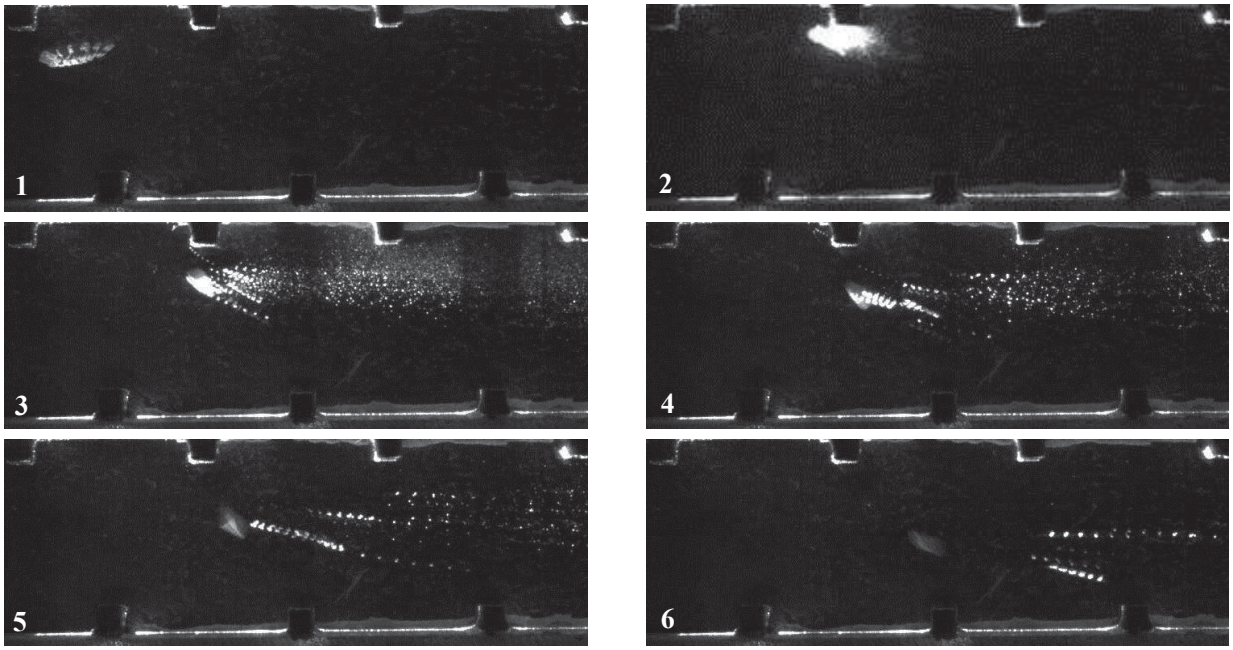

Figure 2.14. Set of images tracking particle breakup of a large AzRD particle colliding with the rib.

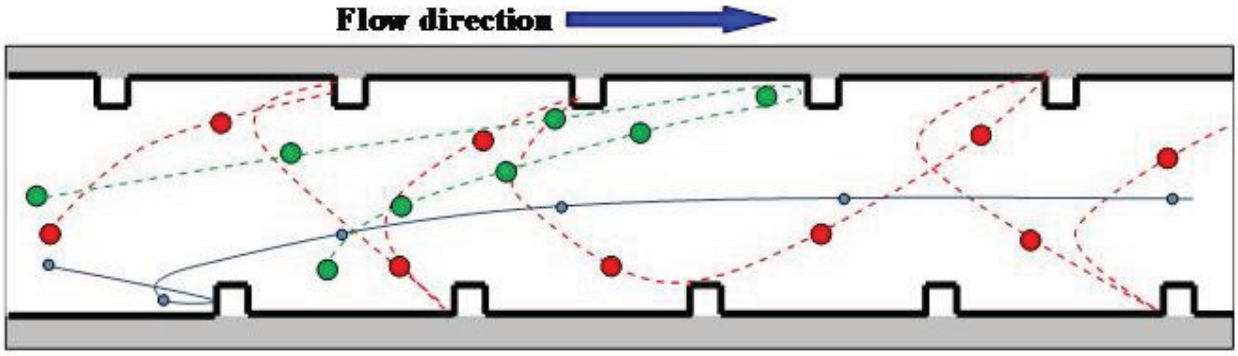

Figure 2.15. Illustration of a high Stokes number (dashed red and green) and an intermediate Stokes number particle (solid blue) moving through a staggered rib-roughened channel.

Comparison of Measured and Predicted Two-phase Channel Flows

Computationally simulating two-phase channel flows are quite complex and many assumptions are typically made for those simulations. Some typical assumptions include the following: particles follow the flow streamlines, there is no particle break-up, and particle collisions with the wall are perfect elastic collisions. The previous section clearly showed that these assumptions were violated as indicated by the qualitative analyses of the particle analysis. Despite these assumptions, one can ask whether the predicted particle dynamics and deposition is still consistent with the qualitative measurements such that the computations would still allow one to use the predictions to design improved, robust cooling methods in the presence of particle laden flows.

When compared to the study by Shah and Taft [12], the experimentally observed particle dynamics appeared markedly different than the LES prediction given the assumptions that were made. One of the findings by Shah and Tafti was a strong preferential concentration of particles near the channel walls after only a few time steps. They predicted that 40% of the 10 μm, 26% of the 50 μm, and 27% of the 100 μm would be within 0.05 D_h of the channel walls. Note that the Reynolds number and particle sizes were similar to those used in our study. This preferential concentration of particles near the walls was not observed experimentally for any of the particle sizes injected. In fact, an opposite trend was seen with a more homogeneous distribution of particles as sand diameters were decreased. Only the larger particles were observed to occasionally linger near the rib walls, owing to their higher inertia when compared to the smaller particles.

Qualitative analysis of our data showed that wall collisions occurred preferentially at the upstream rib face for all sand types and sizes, which does agree with the results presented by Shah and Tafti [12]. They reported a much higher particle impact velocity and concentration on the upstream surface of the rib. As illustrated in Figure 2.15, particles with high Stokes numbers hit the upstream rib face and then rebound into the core channel flow. Having sufficient inertia, these particles cross to the opposite surface and collide with the upstream face of the next rib. The rebounding process was repeated as the particle traveled through the channel, as illustrated in the inset on Figure 2.15. This phenomenon is a result of the presence of ribs on both walls, which serves to restart the rebounding process at each successive rib location. Successive particle collisions from top to bottom ribs was less frequently observed for ISO Coarse sand since particle Stokes numbers were significantly lower than both sieved and unsieved AzRD. Recall that lower Stokes numbers refer to particles being influenced by the local flow such that the particles are reentrained by the flow after a wall collision. The LES study by Shah and Tafti [12] could not predict this rebounding process since the domain was only modeled for one rib pitch with periodic boundary conditions.

It is important to note that the rebounding process would be similar for both a staggered rib channel (this study) and an aligned rib channel as presented by Shah and Taft [12]. The rebounding phenomenon results from three conditions which are independent of the rib staggering: 1) a particle must impact the upstream rib face at a relatively high velocity; 2) the particle, having a sufficiently high Stokes number, follows a ballistic path across the channel while being accelerated by the carrier flow; 3) owing to the presence of ribs on the adjacent wall, the particle impacts another front rib face at sufficient velocity to restart the process.

Conclusions

An experimental study on a rib channel flowfield was conducted to verify the TRDPIV method for both single phase and two-phase flows. The main tasks of this study were to benchmark the TRDPIV facility by comparing against the literature and also to provide qualitative insight into the particle motion within a simulated cooling channel.

Regarding the comparisons of the TRDPIV derived single phase flowfield to the literature, good agreement was found at Re=20,000 when comparing the mean averaged flowfield to those measured by LDV and LES. The presence of the previously reported

separated shear layer and inter-rib recirculating region were fully resolved in addition to a several smaller regions of recirculation past the reattachment point between the ribs. Profiles of mean velocity and velocity RMS also showed good agreement with the literature both above the rib and in the inter-rib region.

For the two-phase flow, TRDPIV measurements of particle motion were described for three different sand size distributions. For all particle sizes, there was a preferential concentration of wall impacts at the upstream rib surface with more wall impacts being observed as particle size increased. Particle rebounding was captured through these studies whereby it was shown that large particles traveled in a direction opposite to the mean flow direction. It was concluded that this occurrence greatly increases particle residence time which, in the engine, would result in much higher particle temperatures due to radiation and thus a greater probability of particle melting and deposition onto the channel walls.

Breakup of large agglomerations of particles was frequently observed during wall collisions, resulting in a decreasing Stokes number as the smaller diameter particles traveled through the channel. As a result of these frequent collisions with the upstream rib surface, the increasingly smaller particles will follow the flow more closely as they convect through the passage. The breakup of particles, through wall collisions, will likely result in the more homogeneous distribution of particles at the developed section as compared to the inlet.

The observed two-phase experimental results did not appear to completely concur with those derived by LES simulations on a two-phase ribbed channel flow, which is in part due to the inherent assumptions that are made. No preferential concentrations of particles were seen, as was reported by LES. For the larger sand diameters, the motion of the particles seemed to be driven primarily by particle-wall or particle-rib impacts, which resulted in significant particle breakup not modeled in the LES study. This work indicates the need for a more complete study combining observed experimental findings with improved modeling.

Nomenclature

General

A	area
d	diameter
D_h	hydraulic diameter

e	rib height
h	channel height
L	characteristic flow length
$\dot{m}$	mass flow rate
m_L	particle mass loading, $m_L = \dot{m}_p / \dot{m}_f = (\rho A N)_p / (\rho A U_b)_f$
N	number of particles
p	rib pitch
Re	Reynolds number, $Re = U_b D_h / \nu$
St	Stokes number, $St = \tau_p / \tau_f$
TKE	turbulent kinetic energy, $TKE = \left[u(x,y,t) - u_m\right]^2 + \left[v(x,y,t) - v_m\right]^2$
u	streamwise velocity
$\vec{U}$	local velocity vector
U_b	bulk streamwise velocity
v	wall-normal velocity
vorticity	curl of the velocity, $\vec{\nabla} \times \vec{U}$
X	streamwise coordinate
Y	wall-normal coordinate

Greek

μ	absolute viscosity
ν	kinematic viscosity
ρ	density
τ_f	characteristic flow time scale, $\tau_f = L_c / U$
τ_s	characteristic sand response time, $\tau_s = (\rho_s d_s^{\,2}) / (18 \mu_f)$

Subscripts

b	bulk
f	fluid

m	mean averaged
min	minimum value
max	maximum value
p	particle
RMS	root mean square

References

1. Perry, A.E., et al., 1969, "Rough wall turbulent boundary layers," Journal of Fluid Mechanics. 37: p. 383-413.
2. Liou, T.M., et al., 1990, "Experimental and Computational Study of Turbulent Flows in a Channel With Two Pairs of Turbulence Promoters in Tandem," Journal of Fluids Engineering. 112(3): p. 302-310.
3. Casarsa, L., et al., 2002, "Characterization of the Velocity and Heat Transfer Fields in an Internal Cooling Channel With High Blockage Ratio," ASME Conference Proceedings. 2002(36088): p. 451-458.
4. Graham, A., et al., 2004, "Flowfield Measurements in a Ribbed Channel Relevant to Internal Turbine Blade Cooling," ASME Conference Proceedings. 2004(41685): p. 383-391.
5. Sewall, E.A., et al., 2006, "Experimental validation of large eddy simulations of flow and heat transfer in a stationary ribbed duct," International Journal of Heat and Fluid Flow. 27(2): p. 243-258.
6. Cui, J., et al., 2003, "Large-eddy simulation of turbulent flow in a channel with rib roughness," International Journal of Heat and Fluid Flow. 24(3): p. 372-388.
7. Abdel-Wahab, S. and Tafti, D.K., 2004, "Large Eddy Simulation of Flow and Heat Transfer in a 90 deg Ribbed Duct With Rotation: Effect of Coriolis and Centrifugal Buoyancy Forces," Journal of Turbomachinery. 126(4): p. 627-636.
8. Sewall, E.A. and Tafti, D.K., 2006, "Large Eddy Simulation of Flow and Heat Transfer in the 180-Deg Bend Region of a Stationary Gas Turbine Blade Ribbed Internal Cooling Duct," Journal of Turbomachinery. 128(4): p. 763-771.
9. Patel, V.C., 1998, "Perspective: Flow at high Reynolds number and over rough surfaces - Achilles heel of CFD," Journal of Fluids Engineering. 120(3): p. 434-444.
10. Sommerfeld, M., 1992, "Modelling of particle-wall collisions in confined gas-particle flows," International Journal of Multiphase Flow. 18(6): p. 905-926.
11. Grant, G. and Tabakoff, W., 1975, "Erosion Prediction in Turbomachinery Resulting from Environmental Solid Particles," Journal of Aircraft. 12(5): p. 471-478.
12. Shah, A. and Tafti, D.K., 2007, "Transport of particulates in an internal cooling ribbed duct," Journal of Turbomachinery. 129(4): p. 816-825.

13. Jakobsen, M.L., et al., 1996, "Particle image velocimetry: Simultaneous two-phase flow measurements," Measurement Science & Technology. 7(9): p. 1270-1280.

14. Liu, Y., et al., 2006, "Turbulent mixing in a confined rectangular wake," Chemical Engineering Science. 61(21): p. 6946-6962.

15. Crowe, C., et al., Multiphase Flows with Droplets and Particles. 1998, Boca Raton, FL: CRC Press LLC.

16. Adrian, R.J., 1997, "Dynamic ranges of velocity and spatial resolution of particle image velocimetry," Measurement Science & Technology. 8(12): p. 1393-1398.

17. Adrian, R.J., 2005, "Twenty years of particle image velocimetry," Experiments in Fluids. 39(2): p. 159-169.

18. Westerweel, J., 1997, "Fundamentals of digital particle image velocimetry," Measurement Science & Technology. 8(12): p. 1379-1392.

19. Eckstein, A. and Vlachos, P.P. 2007, "A robust phase correlation DPIV processing algorithm for time resolved measurements. " in Proceedings of the 7th International PIV Symposium. Rome, Italy.

20. Walsh, W.S., et al. 2006, "Effects of Sand Ingestion on the Blockage of Film-Cooling Holes. " in Proceedings of the ASME Turbo Expo. Reno, NV.

21. Cardwell, N.D., et al. 2008, "Developing and fully developed turbulent flow in ribbed channels. " in Proceedings of the ASME Fluids Engineering Conference. Jacksonville, FL.

Paper 3: Developing and Fully Developed Flow in Ribbed Channels

Cardwell, N.D., Vlachos, P.P., Thole, K.A., 2008, "Developing and Fully Developed Turbulent Flow in Ribbed Channels," Fluids Engineering Conference, FEDSM2008-55190 (nominated for Best Paper)*.

Cardwell, N.D., Vlachos, P.P., Thole, K.A., 2011, "Developing and Fully Developed Flow in Ribbed Channels," accepted for publication in Experiments in Fluids (currently in press), DOI: 10.1007/s00348-010-0993-y.*

[Chapter reprinted with kind permission from Springer Science+Business Media]

Abstract

Wall-mounted roughness features, such as ribs, are often placed along the walls of a channel to increase the convective surface area and to augment heat transfer and mixing by increasing turbulence. Depending on the relative roughness size and orientation, the ribs also have varying degrees of increased pressure losses. Designs that use ribs to promote heat transfer encompass the full range of having only a few streamwise ribs, which do not allow fully developed flow conditions, to multiple streamwise ribs, which do allow the flow to become fully developed. The majority of previous studies have focused on perturbing the geometry of the rib with little attention to the spatially and temporally varying flow characteristics and their dependence on the Reynolds number.

A staggered rib-roughened channel study was performed using Time Resolved Digital Particle Image Velocimetry (TRDPIV). Both the developing (entry region) and a fully developed region were interrogated for three Reynolds numbers of 2,500, 10,000 and 20,000. The results indicate that the flow was more sensitive to Reynolds number at the inlet than within the fully developed region. Despite having a similar mean-averaged flowfield structure over the full Reynolds number range investigated, the population and distribution of coherent structures and turbulent dissipation within the fully developed region were also found to be Reynolds number dependent. Exploring the time-accurate flow characteristics revealed that in addition to vortices shed from the rib shear layer, the region of the rib wake was governed by a periodic process of bursting of the wake vortices resulting in the intermittent ejection of the inter-rib

*Co-authors: Dr. Pavlos P. Vlachos, Mechanical Engineering Department, Virginia Tech
Dr. Karen A. Thole, Mechanical and Nuclear Engineering Department, Penn State

recirculation region into the core flow. This periodic process was the driving mechanism resulting in mixing and heat transfer augmentation. A quadrant-splitting burst analysis was also performed to determine the characteristic frequency and duration of inter-rib bursting as well as the wake shedding frequency, both of which were determined to be Reynolds number dependent.

Introduction

Turbulent channel flows containing rib-roughened walls have been extensively studied for many years, owing to a broad applicability across numerous engineering applications. The effect of the ribs on the flow is often a primary design consideration whereby the presence of the rib geometry induces a desired augmentation of heat transfer along with providing additional convective surface area. Although similar to a combined backward-facing step [1] [2-4] and forward-facing step flow [5, 6], the turbulent flowfield generated from a rib is more complex resulting from the separation off both the rib edges. In addition, the presence of successive ribs provides another layer of complexity resulting from interactions between the rib-induced wakes.

An early study on the effect of rib-roughness on turbulent boundary layer flow was performed by Perry et al. [7] comparing different pitch-to-height ratios of square roughness elements. They identified two primary types of square roughness elements, which were classified as either d-type or k-type. The d-type roughness elements, where the rib pitch was less than three times the rib height, were characterized by fully separated flow over the inter-rib regions, which led to a sustained inter-rib vortex. The k-type roughness elements, illustrated in Figure 3.1, were described by a sufficiently large rib-pitch such that the separated flow over the initial rib became partially reattached before encountering the upstream face of the next rib. Over the years, significant effort has been employed to further clarify the effect of rib elements on the turbulent boundary layer and friction coefficient. The review by Jimenez [8] discusses the body of research for both d-type and k-type roughness studies.

A computational study by Cui et al [9], using a Large Eddy Simulation (LES), further explored the effect of rib spacing for turbulent channel flow having either d-type, k-type, or an intermediate spacing of roughness elements along a single wall. For a relatively small rib height-to-channel-height ratio of 0.1, the presence of the intermediate and k-type roughness elements had a significant effect on the core channel flow, shifting the maximum streamwise velocity away from the geometric center of the channel and closer to the adjacent smooth wall. For d-type roughness having a pitch-to-roughness height ratio of 1 (p/e = 1), the mean outer flow was observed “riding” over the roughness elements with a separated recirculating region contained between each rib pair. With the k-type roughness having a pitch-to-roughness height ratio of nine (p/e = 9), reattachment occurred between subsequent ribs and the presence of vortical

structures was observed within the near-rib region through qualitative observations of the instantaneous velocity fields. For an intermediate roughness type of p/e = 4, the extent of the mean separation cavity was roughly equivalent to the rib pitch. The experimental studies by Wang and Wen-Ruey [10] and Wang et al. [11] for k-type roughness elements supported the results of Cui et al. [9]. It has been shown that, for relatively high rib height-to-channel height ratio of h/e = 0.3, the presence of the ribs along a single wall causes the flow to have a strong three-dimensional velocity component near the side walls [12, 13]. The rib presence has also been shown to significantly augment the wall heat transfer. Researchers have reported a 250% increase in local heat transfer at the inter-rib reattachment location as compared to the smooth wall value [14-17].

Channel flows having rib roughness elements on two parallel walls are often referred to as "fully-roughened". As with comparing the step flow and roughened turbulent boundary layer studies, the results observed for a single-wall roughened channel cannot be readily applied to fully roughened channel flows. The most commonly studied fully-roughened channel configuration consists of square rib-arrays that are oriented 90° to the flow and vertically aligned along the two adjacent walls [18-24]. Numerous computational studies have sought to further investigate fully roughened channel flows with in-line ribs [25-27]. Recent numerical studies often utilize Large Eddy Simulations (LES) and Direct Numerical Simulations (DNS) to resolve the flowfield as compared to previous works, which often utilized the Reynolds-Averaged-Navier-Stokes equations (RANS). However, considerable computational requirements often limit LES and DNS to periodic boundary approximations and low Reynolds numbers. The reader is referred to the text by Bernard and Wallace [28] and the review by Patel [29] for an assessment of the difficulties in simulating turbulent separating flows.

Only a limited number of experimental studies have been performed to resolve the flowfield of a fully-roughened channel with staggered ribs [30, 31]. Of these studies, few have investigated the flowfield dynamics of the channel across a range of Reynolds numbers. The current study investigates a Reynolds number range of 2,500 to 20,000 at two channel locations corresponding to the entrance and a region with fully developed flow. The strength and distribution of coherent structures within the flowfield were also examined. Additionally, the rate of turbulent dissipation was estimated to provide a basis of comparison for computational

simulations which typically require the modeling of both the turbulent dissipation and kinetic energy.

Experimental Facilities and Methodology

For this study, experiments were performed in a fully roughened channel having staggered rib arrays. Flowfield measurements were achieved using an in-house developed Time-Resolved Digital Particle Image Velocimetry (TRDPIV) system and processing algorithm. This section describes the testing facility and rib-roughened channel geometry as well as the TRDPIV system and data processing methodologies.

Test Facility

An illustration of the experimental test facility is shown in Figure 3.2. Compressed, room temperature air was supplied to a plenum. The flowrate was regulated using a control valve located far upstream of the plenum inlet and was measured using a laminar flow element (LFE) with an uncertainty of ±0.5% of the 1.13 m^3/min full scale. The required flowrate for the channel ranged from 0.09-0.7 m^3/min. Given the measured flowrate, the channel Reynolds number was computed using the hydraulic diameter and bulk channel velocity for the length and velocity scaling. It is important to note that for a square duct, the hydraulic diameter (D_h) is equal to the channel height. A differential pressure transducer was used to measure the pressure drop across the LFE. The measured range of pressure drop was 150–1200 Pa with a transducer measurement accuracy of ±0.25% of the 2200 Pa full scale.

Prior to entering the channel, the flow passed through a 40:1 area-ratio plenum, as compared to the channel cross-sectional area. Within the plenum, the flow also passed through a round-hole diffusion plate having a closed to open area ratio of 4:1 before entering the channel section through a bell-mouth inlet to assure spatially uniform and undisturbed inlet flow. Two narrow strips of 80-grit sandpaper, running the width of the channel, were utilized to trip to boundary layer at the channel inlet for both rib walls.

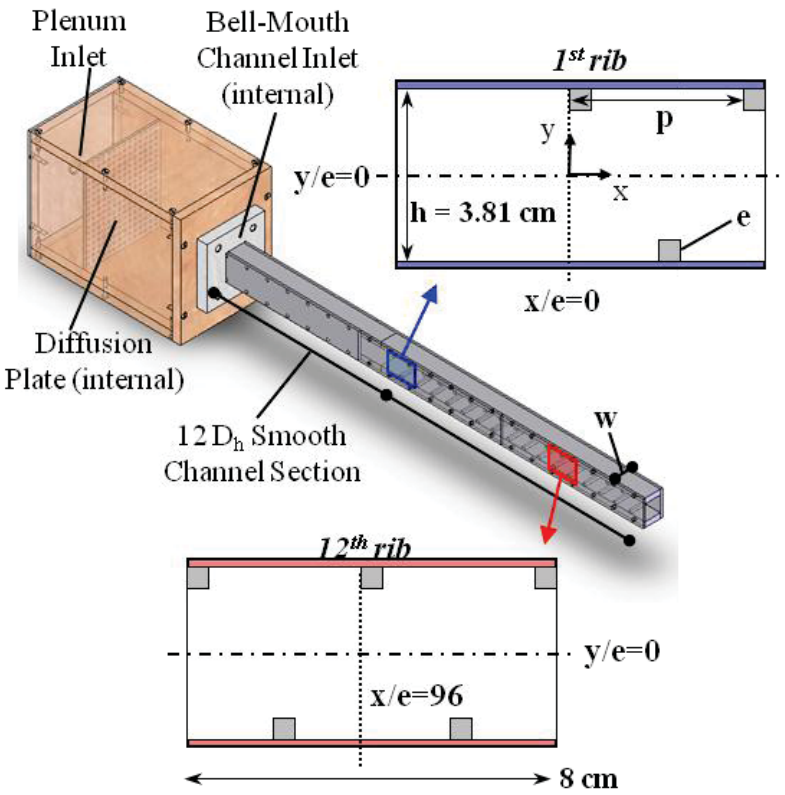

Figure 3.1. Illustration of the rib-roughened channel showing the inlet (1st rib) and fully developed (12th rib) measurement planes.

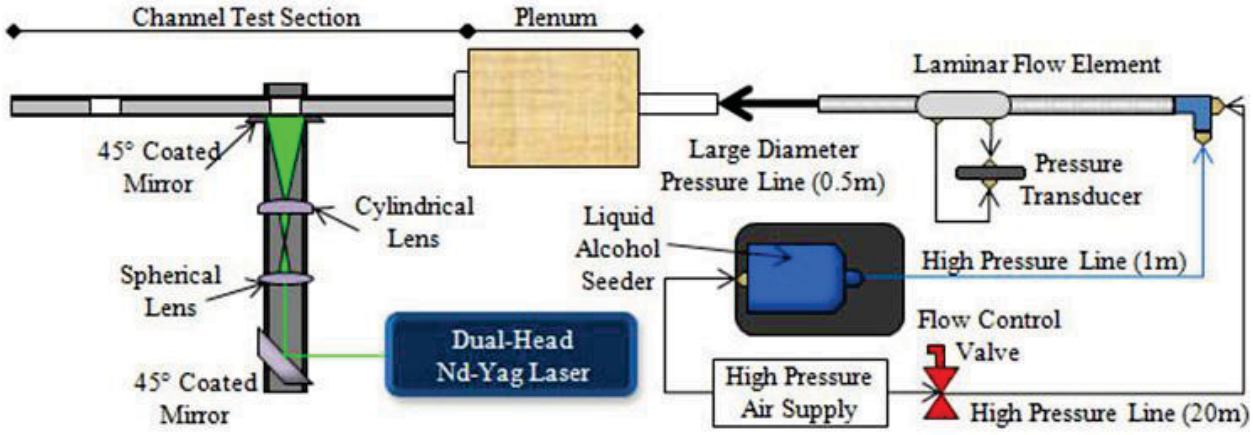

Figure 3.2. Flow facility and TRDPIV system used for rib-roughened channel study.

Staggered Rib Channel Geometry

The rib-roughened channel used for this study, as shown in Figure 3.1 and Figure 3.2, consisted of smooth and rib-roughened sections. A length of twelve hydraulic diameters, D_h,

was chosen for the smooth wall inlet section for the purpose of generating a fully developed mean flow upstream of the rib-roughened channel section. This entrance length is less than the theoretically development lengths of $16D_h$ and $23D_h$ for Re = 2.5k and 20k, respectively. A summary of relevant channel dimensions are given in Figure 3.1 and Table 3.1. The rib pitch-to-channel height ratio of eight (p/e = 8) corresponded to a k-type roughness. Transverse square ribs were placed 90° to the main channel flow along two adjacent walls and were symmetrically staggered with respect to one another. The two regions of interest, shown in Figure 3.1, were centered on the first and twelfth ribs. Based on previous studies of roughened channel flows with aligned ribs [19, 24] the flow was assumed to be fully developed by the twelfth rib. The local coordinate system for each measurement region was defined based on the channel centerline and upstream face of the first and twelfth ribs.

Both the smooth and roughened channel sections were constructed of acrylic. Each rib was also manufactured from acrylic so that the entire channel would be transparent, thus allowing for complete optical and laser access.

Table 3.1. Rib and Channel Geometric Parameters

	Rib Characteristics
h/w	1
e/D_h	0.12
p/e	8
p/D_h	1
Rib angle (α)	90°

Time Resolved Digital Particle Image Velocimetry System

Time Resolved Digital Particle Image Velocimetry (TRDPIV) was used to provide spatio-temporally resolved, noninvasive measurements of the velocity field. A 20W New Wave dual-head Pegasus laser, having a maximum double pulse frequency of 10 kHz, was used to illuminate the flow as shown in Figure 3.2. The laser pulse energy at a sampling frequency of 1.5kHz was 10mJ for each laser cavity. Through the use of optics, the laser beam was manipulated into a very thin (< 1 mm) two-dimensional plane and passed through the channel wall. For each region of interest, the desired area was illuminated by manually traversing the laser sheet.

Imaging normal to the laser sheet, a Photron Ultima APX-RS high speed digital camera recorded images of the fluid tracers with an interframe separation of 450 μs, 120 μs, and 60 μs

for Re = 2.5k, 10k, and 20k. The interframe measurement delays were chosen to assure that the bulk centerline particle displacement was between 4-6 pixels for all flow conditions. With an 8GB buffer, the camera was able to capture ~12000 total frames at 3000 fps operating in double pulsed mode. This camera frame rate corresponded to a 1.5 kHz sampling rate for the flowfield and a total sampling period of approximately two seconds. As illustrated in Table 2, the sampling frequency was sufficient to resolve the estimated large scale shedding behind the ribs. A Strouhal number of 0.2 was utilized for this estimation with the characteristic length and velocity scales equal to the rib height and bulk channel velocity, respectively. It is important to note that the sampling frequency would provide time-resolved measurements with respect to the large-scale structures but cannot resolve the full spectrum of all turbulent scales present in the flow. The camera resolution was set to 1024x464 pixels resulting in a spatial resolution of 84.7 μm/pixel. Accordingly, the measurement size of the two regions of interest was $2.1D_h$ by $1D_h$. A data acquisition card and computer controlled timing hub were used to control and synchronize the laser and camera sampling frequencies. Signal monitoring equipment was used to check the synchronization of the camera and laser timing, thus ensuring that the system was performing as intended. All time-averaged results and statistics for each test were generated using 5000 independent flow samples, which was sufficient to satisfy statistical convergence.

Table 3.2. Estimation of the Rib Shedding Frequency

Re	U (m/s)	Shedding Freq. (Hz)
2,500	0.9	38
10,000	3.7	154
20,000	7.5	312

An alcohol based liquid atomizer produced approximately 1 μm diameter droplets which were used as flow tracers. The flow tracers were injected upstream of the LFE, as shown in Figure 3.2, to ensure a homogenous distribution of particles within the channel. The imaged particle size was calculated from Mie scattering theory to be approximately 2 pixels in diameter. This imaged diameter of the droplets was also verified through qualitative observations. Because of the small imaged particle size, special attention was therefore paid to the selection of a processing algorithm which would reduce or eliminate the expected peak-locking effects.

DPIV Analysis Methodology: Robust Phase correlation

The most common method of analyzing digital particle image velocimetry (DPIV) images employs a standard cross-correlation technique (SCC). The SCC utilizes a Fast Fourier Transform (FFT) based correlation to measure the particle displacement between image pairs [32-34]. Herein, we utilized a new technique, termed Robust Phase Correlation (RPC) [35-37], which improves upon the SCC by employing optimum spectral filtering based on a generalized cross-correlation. The method has been shown to increase measurement accuracy while reducing peak-locking, which is a common problem related to having a small imaged flow tracer diameter. Supporting the results of Eckstein and Vlachos [35], significant improvements in valid vector detection and measurement accuracy were observed for the present rib channel experiment when using the RPC technique versus the SCC technique. All data processing was performed with the RPC using the parameters listed in Table 3.3.

Table 3.3. DPIV Processing Parameters (Robust Phase Correlation)

	Two-Pass Discrete Window Offset
1st pass correlation window	64x32 (pixels)
2nd pass correlation window	32x16 (pixels)
grid spacing	4x4 (pixels)
number of vectors	241 x 111
flow samples per test	5000
flow sampling frequency	1500 Hz
windowing function	50% Gaussian (with zeropadding)

Identification of Coherent Structures

Significant research has been performed on the identification and classification of coherent structures (CS) within a turbulent flowfield [38-40]. The method chosen for the current study was the critical point method, often referred to as the delta-criterion, proposed by Chong et al. [38]. In short, this method defines a CS as one that has a closed streamline, which is identified from the velocity gradient tensor, $D = \nabla\vec{U}$, as a region of only complex eigenvalues as evidenced when the discriminant (Δ) is strictly positive:

$$\Delta \equiv \left(\tilde{R}/2\right)^2 + \left(\tilde{Q}/3\right)^3 \quad (1)$$

where $\tilde{R} \equiv R + 2P^3/27 - PQ/3$ and $\tilde{Q} \equiv Q - P^2/3$ are calculated from the invariants of the velocity gradient tensor: $P = -\text{trace}(D)$, $Q = \left(P^2 - \text{tr}(D^2)\right)/2$, $R = -|A|$.

As with all vortex identification methods, the delta-criterion requires some validation and tuning to minimize the possibility of false identifications. For the current work, a simple Galilean decomposition [41] of the flowfield aided in the adjustment of two thresholding parameters: the magnitude of Δ and the computed area of each individual region of complex eigenvalues. For all case, it was found that ignoring points with < 0.1% of the maximum Δ value and all identified regions with < 36 (grid units)^2 surface area provided the best balance between reducing the number of misidentifications and preserving correctly identified structures.

Once calibrated, the delta-criterion method was applied on the full flowfield for 5000 flow samples. After processing and validation, each connected region of positive Δ was taken as an identified CS. The center of the CS was taken as the weighted centroid of the connected region, which was observed to be accurate within several grid units of the observed core location. The circulation direction and magnitude were also computed for each identified CS. This was accomplished by computing a line integral over the simple, closed-path perimeter of the CS as previously defined by the delta-criterion method. It should be noted that coherent structures with circulation strength of less than 1% of the maximum measured circulation were discarded.

Dissipation Rate Estimation

The rate of turbulent energy dissipation was also estimated from the time-resolved velocity measurements. Single point measurement techniques, such as hotwire or LDV, must rely on assumptions of local isotropic behavior and Taylor's hypothesis of frozen turbulence to estimate the turbulent dissipation. By spatio-temporally resolving a slice of the flowfield, TRDPIV has the advantage of directly measuring spatial derivatives needed to calculate the dissipation rate. However, direct estimation of the dissipation rate from TRDPIV is often deficient given that the spatial resolution is typically much larger than the Kolmogorov length scale.

To address this deficiency, the large eddy PIV method by Sheng et al. [42] was used to estimate the rate of turbulent dissipation within the rib-roughened channel. Sheng et al. proposed

using a subgrid-scale model to estimate the turbulence dissipation rate, given that the spatial resolution of TRDPIV is typically somewhere between the integral length scale and the Kolmogorov length scale of the flow. This methodology was adapted from computational fluid dynamics, specifically from Large Eddy Simulations (LES), that seek to resolve only the larger turbulent scales of the flow and model the smaller scales. This partial modeling is possible given that the smaller scales are generally considered to be more Reynolds number dependent and less flowfield dependent than the larger scale structures that are more flowfield dependent. For a more thorough review on the estimation of dissipation rate from DPIV, the reader is referred to the works by Sheng et al. [42] and Sharp and Adrian [43].

For the current study, the Smagorinsky model [44] was used to estimate the subgrid-scale stress tensor. The Smagorinsky constant was set to 0.17, which is within the range of commonly used values for turbulent flow. The grid spacing for the interrogation window, given in Table 3.3, was chosen as an estimate of the filter width used to separate the large-scale and small-scale structures. Since only two-dimensional slice of data was measured, local isotropic assumptions were made for the out of plane stresses, which is commonly accepted for this type of analysis [42, 45]. For each flow sample, the spatial derivatives of velocity were computed using a second-order finite difference scheme. Based on our previous work this approach provides a good compromise between the propagation of error and computational simplicity of the method [46, 47].

Uncertainty Analysis of Measured and Computed Parameters

The uncertainty associated with each reported parameter was calculated for all test conditions to assure the significance of the results. These reported values include the channel Reynolds number, flowfield velocities, turbulent kinetic energy (TKE), turbulence dissipation rate, as well as the location and circulation strength of the identified coherent structures.

The uncertainty in Reynolds number, as calculated using the sequential perturbation method [48], was approximately ±4.5% and ±0.8% of the measured value at Re = 2.5k and 20k, respectively. Regarding the measurement of the mean averaged flowfield, it is known from statistical theory that the sample mean approaches the population mean as the sample size approaches infinity. If we assume that each individual measurement of velocity is unbiased, then the uncertainty in the mean is approximately equal to the standard deviation of the sample

population, σ, divided by the square-root of the number of samples. This is commonly referred to as the standard error of the mean, SEM. The mean uncertainties in velocity, TKE, and turbulent dissipation for 5000 flow samples are shown in Table 3.4 as well as the 95% confidence values. For the measurement of mean velocity and TKE, the uncertainties were low (<0.5%) owing to the large sample size as well as the improved accuracy of the RPC method. Negligible variation in uncertainty for mean velocity and TKE was observed for different Reynolds numbers.

The relative uncertainty in turbulence dissipation was found to be approximately one order of magnitude greater than that for the velocities. This increase resulted from elevated uncertainty in the estimation of the spatial gradients, especially in regions of high shear. Overall, the reported relative uncertainty in turbulence dissipation was less than 5%, which was considered acceptable. It is important to note that this uncertainty does not account for any bias error resulting from the use of the Smagorinsky model. This issue of uncertainty in the Large-eddy PIV method was recently evaluated for zero-mean isotropic turbulence [45] showing that the bias error may be as large as 100% when compared to other methods for estimating turbulence dissipation. The majority of the bias was attributed to uncertainty in the value of the Smagorinsky constant, which may be adjusted to correct for this bias error.

The uncertainty in the core location and circulation strength of identified coherent structures was based on the measurement and computation methodologies. Given the discrete measurement of velocity, the uncertainty in the core location was estimated to be on the order of the grid spacing, which was approximately ±7% of the rib height. A similar value of uncertainty was also attributed to the estimated radius of the coherent structure, which was used for computing the circulation strength. The typical error in the RPC PIV velocity measurements, based on the analysis by Eckstein and Vlachos [36], was estimated to be ±1.4% of the mean velocity. Given the error in the radius and velocity estimate, we estimate that the cumulative error in circulation strength was about ±7.1% of the mean circulation strength.

Table 3.4. SEM Uncertainties (and 95% Confidence Interval)

	Re - 20k IN	Re - 20k DEV
$\bar{u}/U$	±0.14% || (±0.40%)	±0.34% || (±0.62%)
$\bar{v}/U$	±0.09% || (±0.24%)	±0.20% || (±0.34%)
$\overline{TKE}/U^2$	±0.18% || (±0.48%)	±0.39% || (±0.71%)
$\bar{\varepsilon} \cdot e/U^3$	±1.45% || (±3.87%)	±2.47% || (±4.55%)

Time Averaged Flowfield Results

The velocity distribution was measured at the roughened channel inlet to verify flow uniformity entering the ribbed section. Plotted in Figure 3.3 are ensemble-averaged profiles of the u-component of velocity as well as the turbulent fluctuations measured upstream of the first rib (x/e = -7) within the smooth channel section. All velocities and wall distances were nondimensionalized by the appropriate friction velocity, u_τ, and are plotted for one-half the channel height. The friction velocity was determined by minimizing the root mean squared deviation (RMSD) of the ten points closet to the centerline and the well-established logarithmic region correlation, as shown in Figure 3.3. RMSD for Re of 2.5k, 10k, and 20k were 0.003, 0.004, and 0.024 m/s, respectively.

Overall, the results matched well with published data for a smooth-wall turbulent channel flow [49-52]. For all Reynolds numbers, the observed peak in $u'^+ \approx 2.7$ at $y^+ = 15$ matched well with trends reported in the literatures for both channel and boundary layer flows [53], as did the decay to a value of $u'^+ \approx 1$ at the channel centerline. However, differences were observed in the wake region as compared to the published data, most notably the lack of a well defined shoulder-region. This dissimilarity is attributed to the $12D_h$ smooth channel development length, which was previously mentioned as being shorter than is required for the mean and fluctuating velocities to become fully developed, especially with respect to the channel centerline. Further investigation into the spectral content of the u' turbulent fluctuations (not shown) confirmed, however, that the flow entering the roughened channel section was indeed turbulent for all cases.

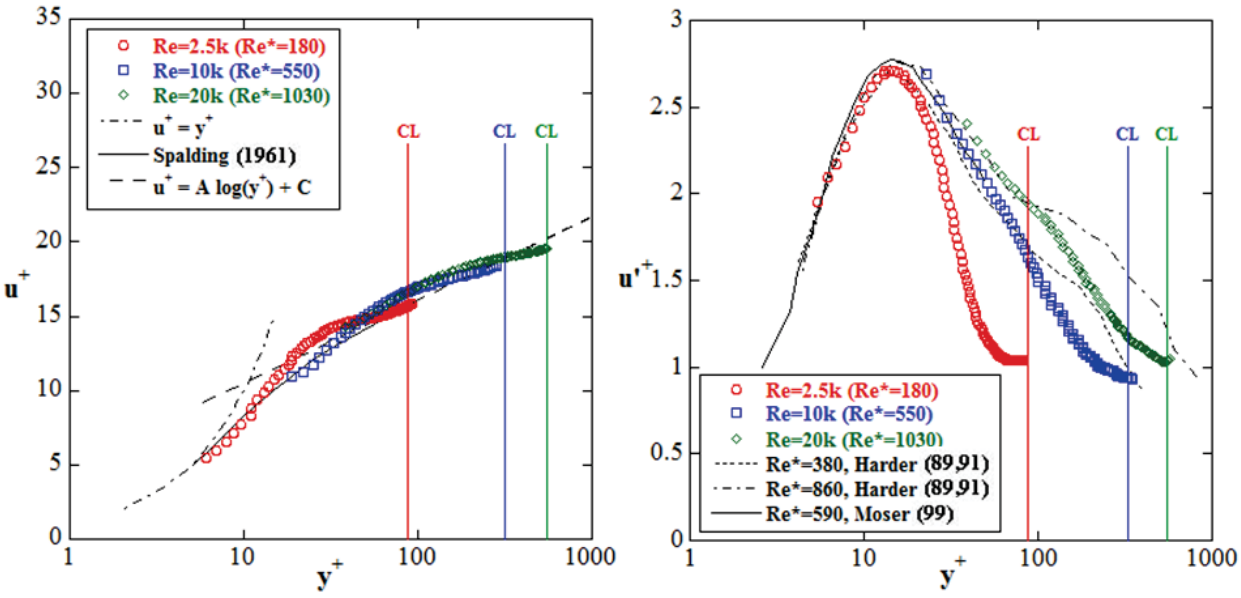

Figure 3.3. Ensemble averaged velocity profile for a) u and b) u′, plotted in wall units at x/e = -7 and spanning y/e = 0 to 4.

Regarding the flowfield development across multiple rib pitches, comparisons of u-component velocity and turbulence intensity profiles in Figure 3.4 confirms that the channel flow was fully developed by the twelfth rib, or x/e = 96 from the channel inlet. As discussed earlier, the study by Graham et al. [19] reported a required development length of ten rib pitches for a channel with inline ribs at a Reynolds number of 20,000. The velocity profiles in Figure 3.4a-b confirm that this is satisfied for a staggered rib configuration across the evaluated Reynolds number range.

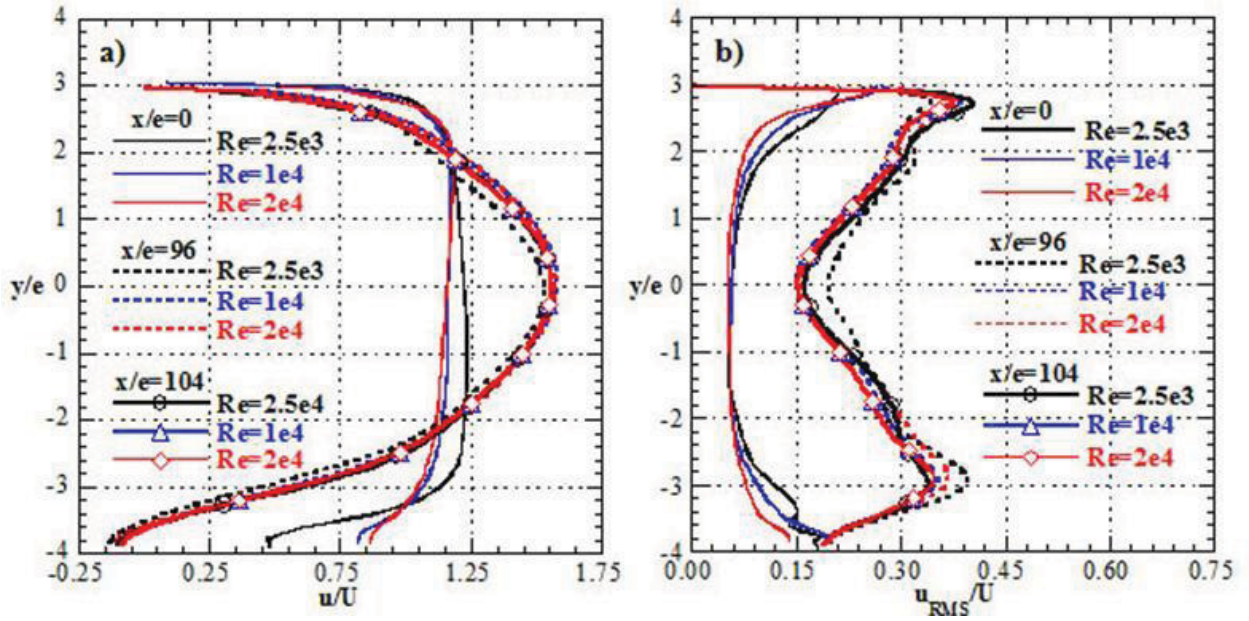

Figure 3.4. Spanwise slices of a) mean and b) RMS u-component velocities within the inlet and developed region.

As a result of the rib presence the flow is subject to boundary layer separation, regions of recirculation, reattachment of separated flow, and a strong mixing layer. To further elucidate the characteristics of these flow features to the channel Reynolds number, a physical description is presented for each test condition in Figure 3.5 and Figure 3.6.

The white lines in Figure 3.5 and Figure 3.6 corresponded to the shear layers emanating from the corners of the rib, which were identified from the local maxima of the spanwise TKE gradient, $\partial \mathrm{TKE}/\partial \mathrm{y}$. The shear layers were easily identified this way, given that the interaction between rib-deflected flow (high velocity) and the separated flow (low velocity) resulted in abrupt increase in TKE. The same abrupt increase in TKE was also observed for the shear layer between the mixing layer and the separated inter-rib flow, which was used to identify the lower extent of the mixing layer. Also computed was the stream function, which led to the identification of the separating and reattaching streamline as illustrated by the black line in Figure 3.5 and Figure 3.6. Recirculating regions, shown as gray lines with white directional arrows, were based on visual observations of the flowfield.

At the inlet (Figure 3.5), the velocity gradient in the approaching boundary layer generates a clockwise recirculation area upstream of the rib face (RR1) for all Reynolds numbers. At Re = 2.5k, the maximum velocity in this region is relatively high at 21% of the

bulk channel velocity, which displaced the incoming boundary layer by impartation of flow momentum in the wall-normal direction. Non-dimensional turbulent kinetic energy (TKE) levels in the region of RR1 were low (~0.02 at x/e = -0.5 & y/e = 3.5). As Reynolds number was increased, a decrease in the size of RR1 was observed due to inertial effects as well as an increase in TKE upstream of the rib, signifying an increase in turbulence upstream of the rib at higher Reynolds numbers.

Separation off the sharp corners of the rib generated a strong mixing layer (ML), evidenced by high values of TKE as shown in Figure 3.5. The upstream separation resulted from the impingement of the separated boundary layer on the upstream corner of the rib. As Reynolds number was increased from Re = 2.5k to Re = 10k, higher TKE was observed on top of the rib which was attributed to an upstream shift of the shear layer's separation point. Increasing Reynolds number from 10k to 20k did not significantly affect the separation point of the upstream shear layer, which appeared to be at a maximum. Separation of the flow off the downstream rib corner resulted from the adverse pressure gradient which was caused by the sudden area expansion of the channel behind the rib. These two separated shear layers provided the upper and lower bounds of the ML.

The separated ML governed the overall flow structure of the inter-rib region. At Re = 2.5k, the ML remained fully detached resulting in a large back flow region (BFR). For the higher Reynolds numbers, the separated ML reattached between ribs at x/e = 5.75, which in turn generated a large recirculating region behind the rib (RR4). Two small, corner recirculating zones (RR2 and RR3) were also observed downstream of the first rib and upstream of the second rib. As with RR1, the spatial extent of these structures decreased with increasing Reynolds number such that they were not well resolved at Re = 20k.

Within the developed region (Figure 3.6), the sensitivity of the flowfield to the Reynolds number was less pronounced than at the inlet. The corner recirculating regions (RR1, RR2 and RR3) were present for all Reynolds numbers, although a decrease in the spatial extent of these structures was observed as Re was increased from 2.5k to 10k. High levels of TKE were observed on top of the rib for all Reynolds numbers, indicating that the flow separation on top of the rib was similar for all Reynolds numbers. This was attributed to locally high values of TKE upstream of the rib resulting from the presence of the ML from the previous rib. Interestingly, a

10% higher value of peak TKE was observed within the ML for Re = 2.5k as compared to Re = 10k and 20k. Higher values of TKE were also observed above the mixing layer at Re = 2.5k.

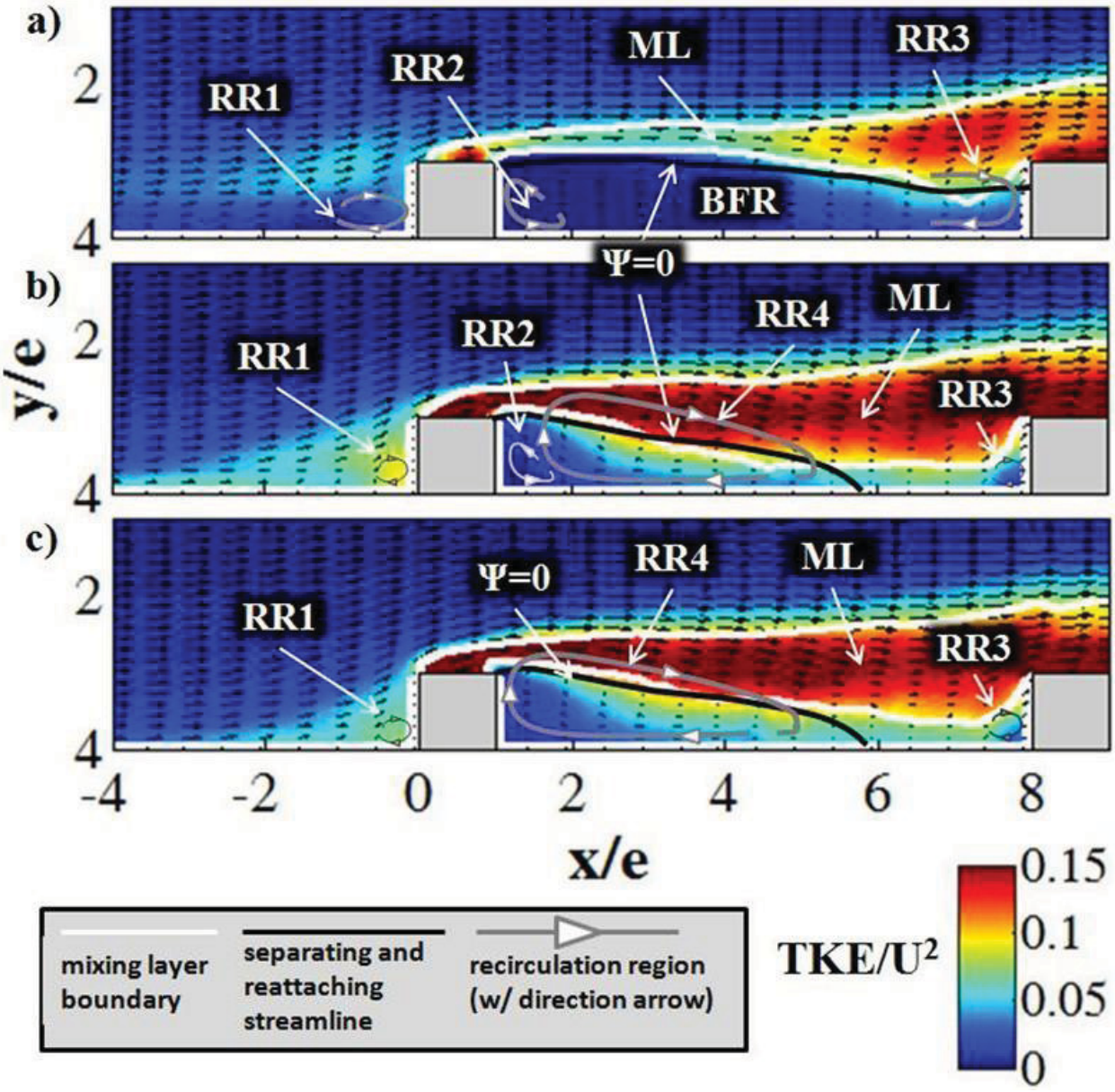

Figure 3.5. Contours of TKE overlaid with velocity vectors, with a streamwise vector skip = 7, for a) Re = 2.5k-IN b) Re = 10k-IN c) Re = 20k-IN.

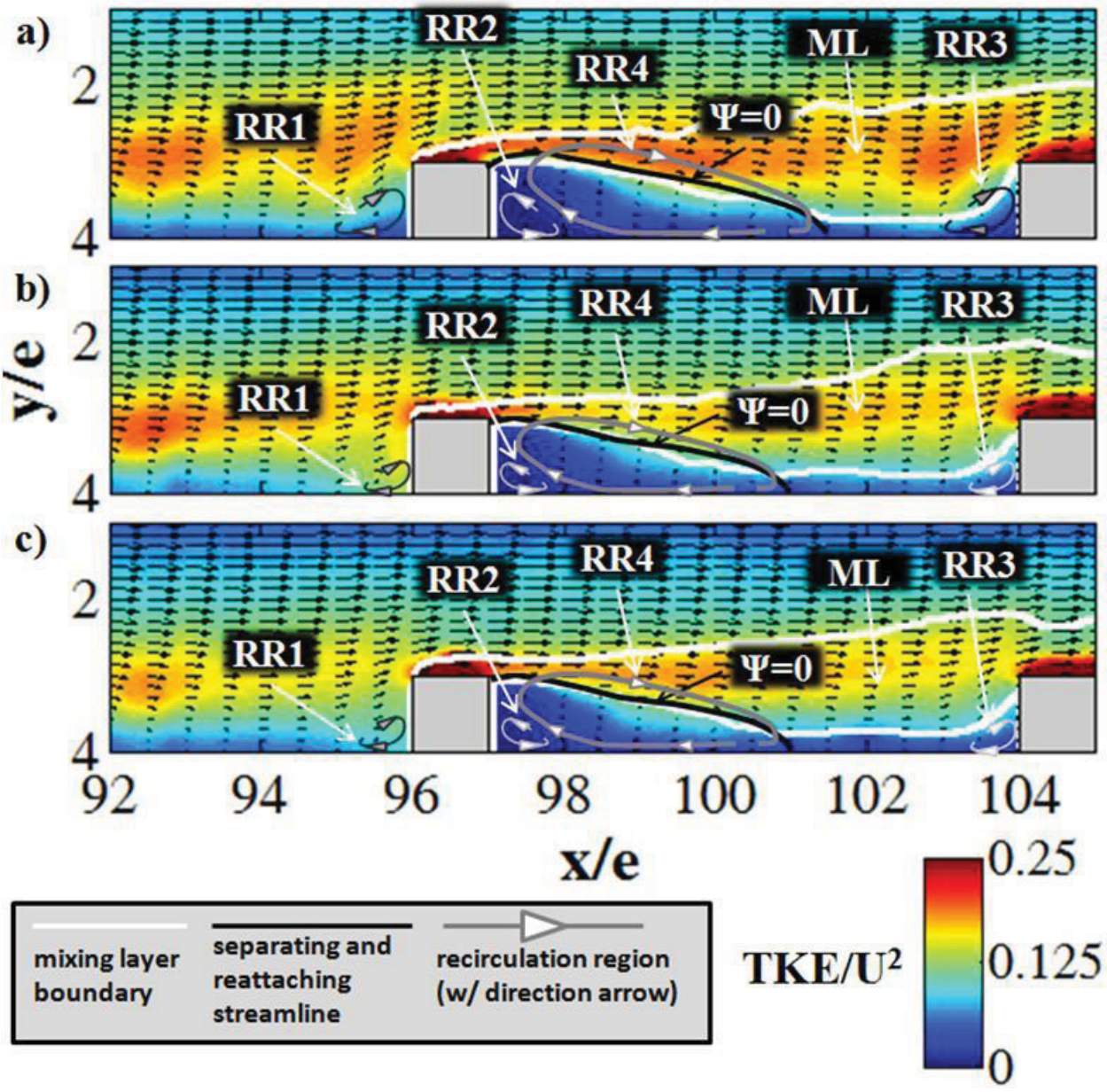

Figure 3.6. Contours of TKE overlaid with velocity vectors, with a streamwise vector skip = 7, for a) Re = 2.5k-DEV b) Re = 10k c) Re = 20k-DEV.

Turbulence Dissipation Rate

Provided in Figure 3.7 are the contours of turbulent dissipation as estimated by the large eddy PIV method [42]. At the inlet, elevated levels of dissipation were observed in the ML region, as previously defined in Figure 3.5 and Figure 3.6. For Re = 2.5k, the delayed separation of the upstream shear layer was further evidenced by lower values of dissipation on the top of the rib (x/e = 0 to 1) as compared with Re = 10k and 20k. An additional area of increased dissipation was also observed upstream of the second rib (x/e = 6.5 to 8) at Re = 10k and 20k, which was attributed to the impingement of the mixing layer on the upstream rib face. Increasing Reynolds number from 10k to 20k resulted in an increase in the spatial extent and magnitude of this region, which was the only significant difference in ensemble-averaged dissipation between the two Reynolds numbers.

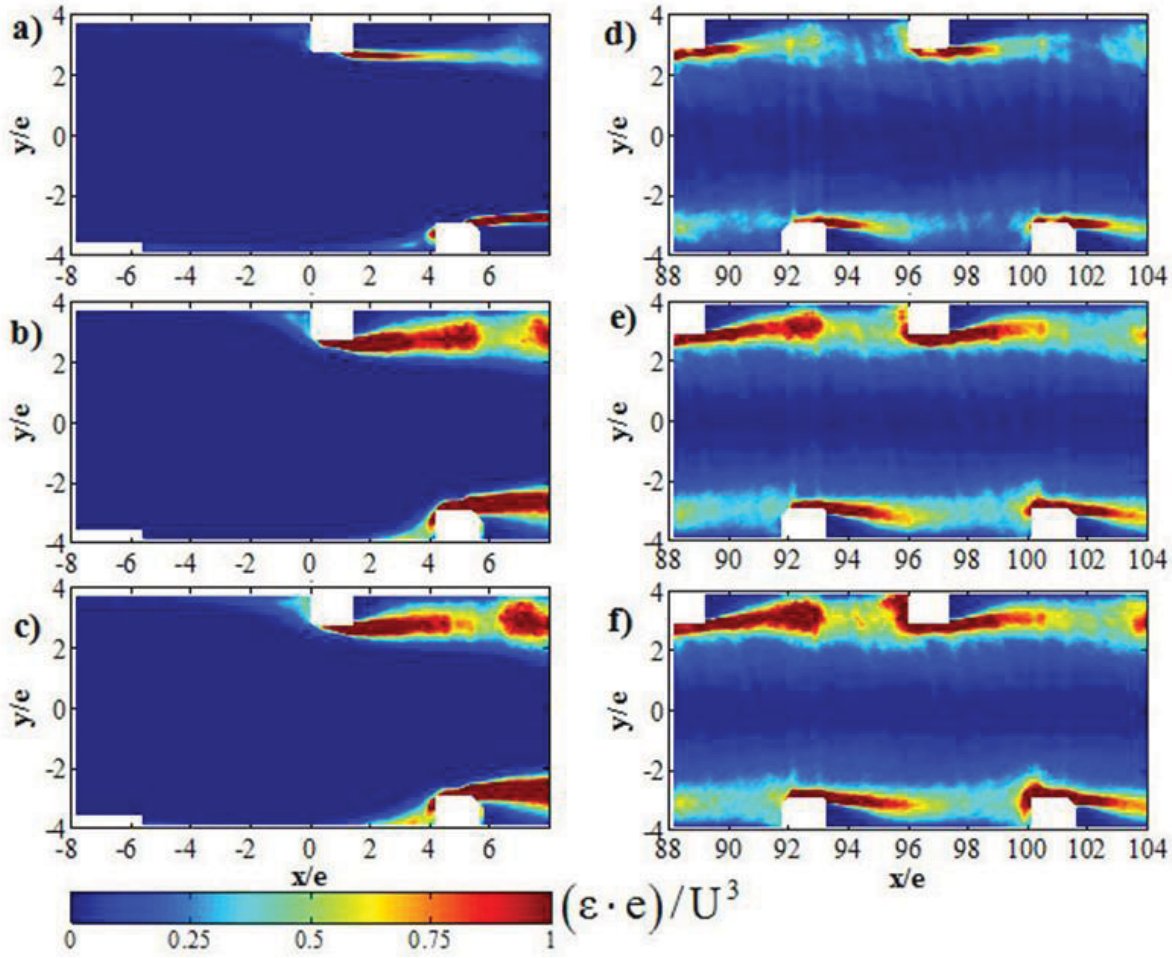

Figure 3.7. Contours of turbulence dissipation for a) Re = 2.5k-IN b) Re = 10k-IN c) Re = 20k-IN d) Re = 2.5k-DEV e) Re = 10k-DEV f) Re = 20k-DEV.

A 24X increase in turbulent dissipation was observed along the channel centerline between the inlet and developed regions. The CS identification results, which are presented in the following section, showed a larger presence of CS within the core flow of the developed region. This suggests that the higher dissipation levels were a result of the interaction between the CS and the bulk channel flow, which likely is also the cause of increased TKE within the core flow.

As with the inlet, elevated dissipation was measured within the rib ML in the developed region. Increasing Reynolds number from 2.5k to 10k resulted in an 8% increase in the peak dissipation observed within the ML. In addition to an increase in the downstream length of this elevated region, higher dissipation was also observed upstream of the rib. Recall that this region of increased dissipation was also observed at the inlet. However, the increase in the dissipation within the developed region was much closer to the upstream rib face than at the inlet. Further increasing Reynolds number from 10k to 20k expanded the extent of this region and increased the peak dissipation by ~6%.

Time Accurate Flow Characteristics and Analysis of Coherent Structures

The shear layer between the high-momentum central flow and the low-momentum recirculation region (RR4), as well as the ejection of the recirculating regions during unsteady "bursting events" at the walls, resulted in the generation and shedding of CS off the ribs. Several instantaneous snapshots of the flowfield, shown in Figure 3.8, illustrate a typical disruption and the subsequent ejection of thae inter-rib recirculation region into the core channel flow. The nondimensionalized time, t*, was defined as the measurement time over the characteristic fluid scale, τ_f, which was equal to the ratio of hydraulic diameter to channel bulk velocity. The rib wake was at the reference state at t* = 0, which was chosen by observation of the velocity field. After a period of time, turbulent instabilities in the ML result in the formation of two counter rotating vortices, as shown in t* = 0.37, which produces a relatively high velocity jet in the wall normal direction as illustrated by the black arrow. This spanwise fluid displaces the ML into the core flow, disrupting it and causing a rapid ejection of the separated inter-rib region into the core flow, as shown in t* = 1.85. Once the ejection mechanism has completed, the shear layers reorganize resulting in a new formation of RR4, as illustrated in t* = 2.22 and 2.39. This process was observed at all Reynolds numbers and channel locations.

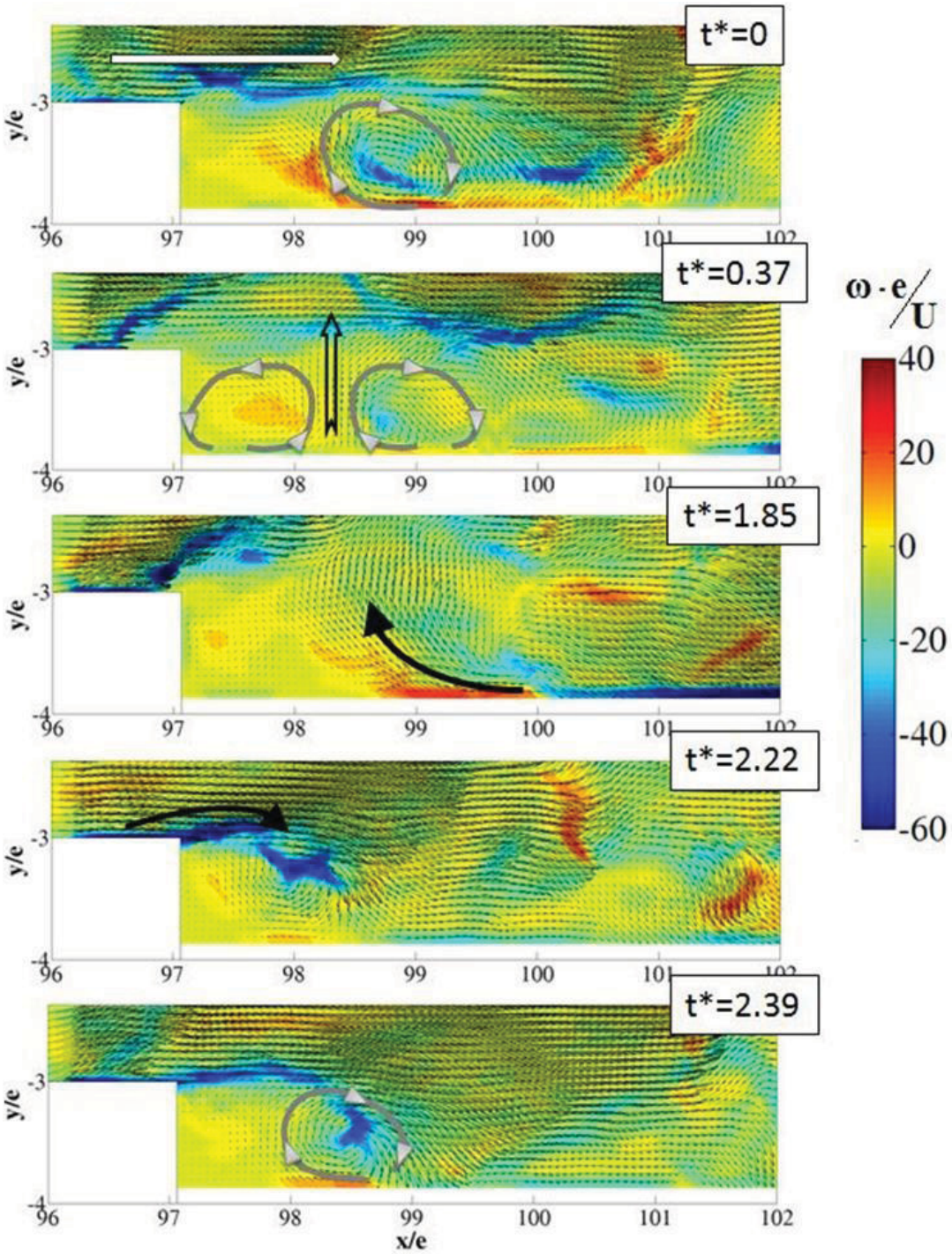

Figure 3.8. Five instantaneous flowfield snapshots illustrating the bursting and ejection of the inter-rib recirculating region, Re = 2.5k-DEV.

Burst events within the channel flowfield were quantified through quadrant-splitting of the Reynolds stress temporal history. This type of analysis has been shown to accurately identify both bursting and sweeping motions in turbulent boundary layers [54-58]. Shown in Figure 3.9a, the Reynolds stresses at each measurement location were arranged into four quadrants corresponding to the sign of u′ and v′. A burst was identified by a shift of the flow into the second quadrant (Q2), which is associated with ejection motions (u′ < 0, v′ > 0). The burst was deemed complete once the Reynolds stresses no longer resided in the second quadrant. From this information the inter-burst time, ΔT, and burst duration, Δt, were quantified for the entire flowfield, as illustrated in Figure 3.9c. The burst analysis was chosen over a spectral analysis given the high level of flow intermittency, as indicated by the broad range of inter-burst times in Figure 3.9b within the fully developed inter-rib region.

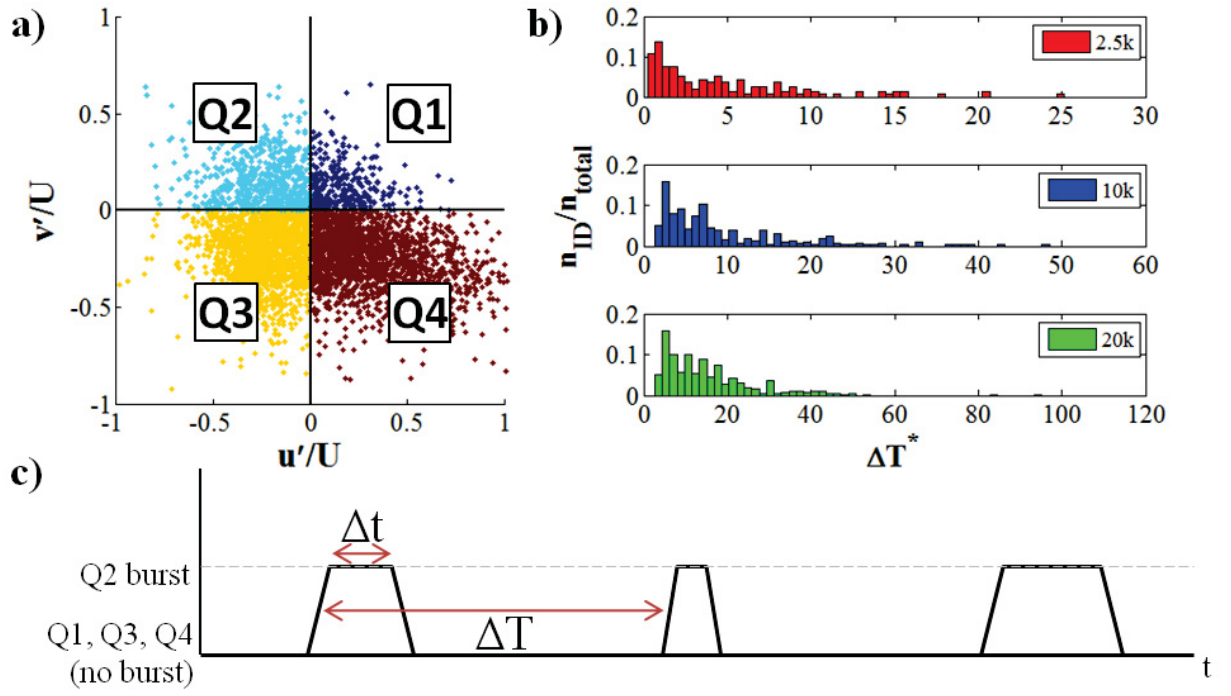

Figure 3.9. a) Illustration of the u′/v′ quadrant analysis, b) non-dimensional inter-burst time for x/e = 99 and y/e = -3, and c) the definition of inter-burst time and burst duration.

The inter-burst separation and burst duration are shown in Figure 3.10 and Figure 3.11 as Strouhal numbers non-dimensionalized by the bulk channel velocity, U, and the rib height, e.

$$St_{\Delta T} = \frac{e \cdot 1/\Delta T}{U} \qquad St_{\Delta t} = \frac{e \cdot 1/\Delta t}{U} \tag{1}$$

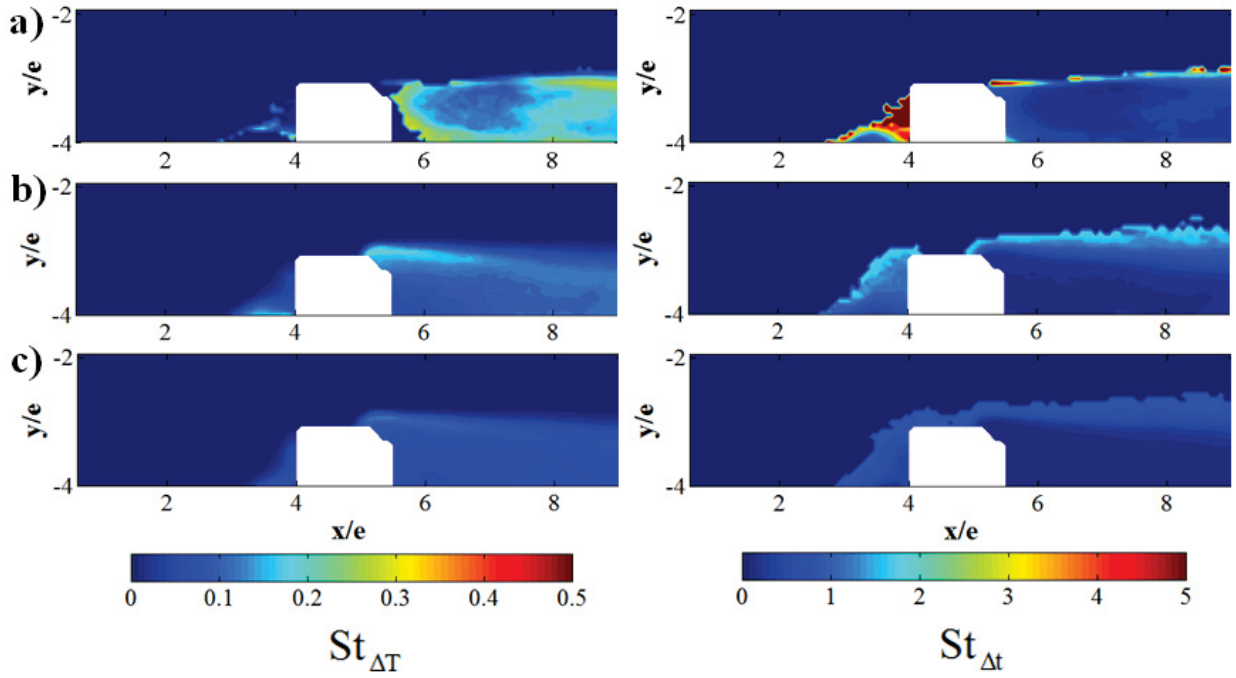

Figure 3.10. Ensemble-averaged inter-burst frequency and duration centered on the 1st rib within the inlet section for a) Re - 2.5k, b) Re - 10k, and c) Re - 20k.

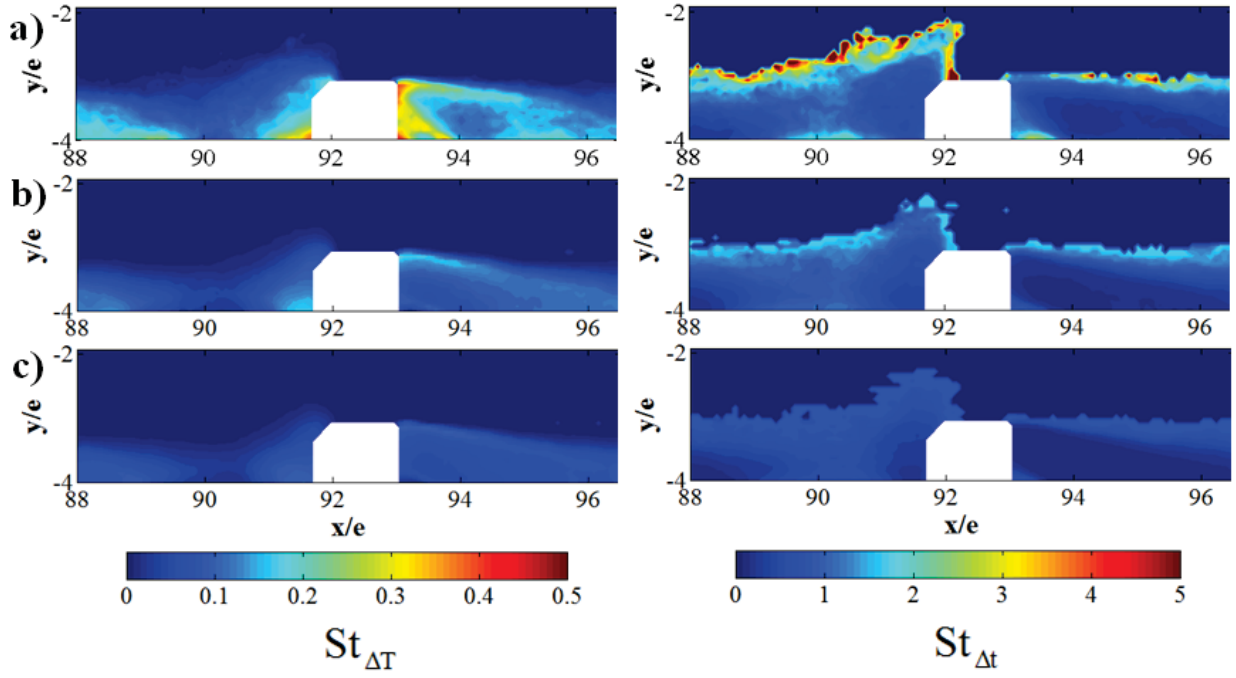

Figure 3.11. Ensemble-averaged inter-burst frequency and duration centered on the 12th rib within the fully developed section for a) Re - 2.5k, b) Re - 10k, and c) Re - 20k.

Within the inlet and fully developed regions, the bursting of RR1 and RR4 (see Figure 3.5 and Figure 3.6) were visible at all Reynolds numbers as well as the corner vortex RR2 at Re = 2.5k. Bursts were also observed within the rib-induced mixing layer (ML), which were attributed to the bursting of coherent structures generated by Kelvin-Helmholtz instabilities.

The frequency of RR4 bursting, as illustrated in Figure 3.8, was found to be strongly dependent on flow Reynolds number and only slightly affected by channel location. Shown in Table 3.5, the burst frequency was inversely proportional to Reynolds number and decreased by 57% at the inlet and 33% within the fully developed region between Re = 2.5k and 20k. In addition, the non-dimensional burst duration increased with Reynolds number, as shown by the 57% decrease in $St_{\Delta t}$ at the inlet and 39% within the fully developed region between Re = 2.5k and 20k. Overall, the results indicate that inter-rib bursts occur less frequently at higher Reynolds numbers but have a longer disruption period.

The rib wake shedding frequency was also determined using the quadrant splitting analysis, as indicated by the burst frequency and duration downstream of the rib corner within the rib wake (Table 3.5). The burst frequencies were inversely proportional to Reynolds number, with a stronger sensitivity observed within the fully developed region as compared to the inlet. It is important to note that the Strouhal frequencies observed were less that the commonly accepted value of approximately 0.2 for all cases sans Re = 2.5k within the developed region.

Table 3.5. Average Burst Frequencies and Durations in the Wake and Recirculating Regions

	wake region (x/e=6.0 ; y/e=-3.3)		**recirc. region (x/e=6.0 ; y/e=-3.7)**		**wake region (x/e=94.0 ; y/e=-3.3)**		**recirc. region (x/e=94.0 ; y/e=-3.7)**	
Re	**$St_{\Delta T}$**	**$St_{\Delta t}$**	**$St_{\Delta T}$**	**$St_{\Delta t}$**	**$St_{\Delta T}$**	**$St_{\Delta t}$**	**$St_{\Delta T}$**	**$St_{\Delta t}$**
2.5k	0.14	0.28	0.14	0.28	0.21	0.72	0.12	0.23
10k	0.12	0.23	0.09	0.17	0.16	0.43	0.10	0.19
20k	0.08	0.14	0.06	0.12	0.09	0.23	0.08	0.14

Figure 3.12 illustrates the total population of coherent structures (CS) as identified by the delta-criterion method. At the inlet, a band of high strength CS was observed emanating off the upstream corner of the first rib for all Reynolds numbers. At Re = 2.5k, the spatial extend of this band matched closely with the location of the ML as identified in the mean-averaged flowfield (Figure 3.5 and Figure 3.6). Additionally, a region of CS was also observed upstream of the rib

face corresponding to the location of RR1. As Reynolds number was increased to 10k, a large plume of high strength CS was observed downstream of the first rib, which spanned a larger region than the identified ML. Additionally, a greater number of low-strength CS were identified in the approaching boundary layer as well as within the core channel flow. Only marginal differences in the distribution of CS were observed between Re = 10k and 20k.

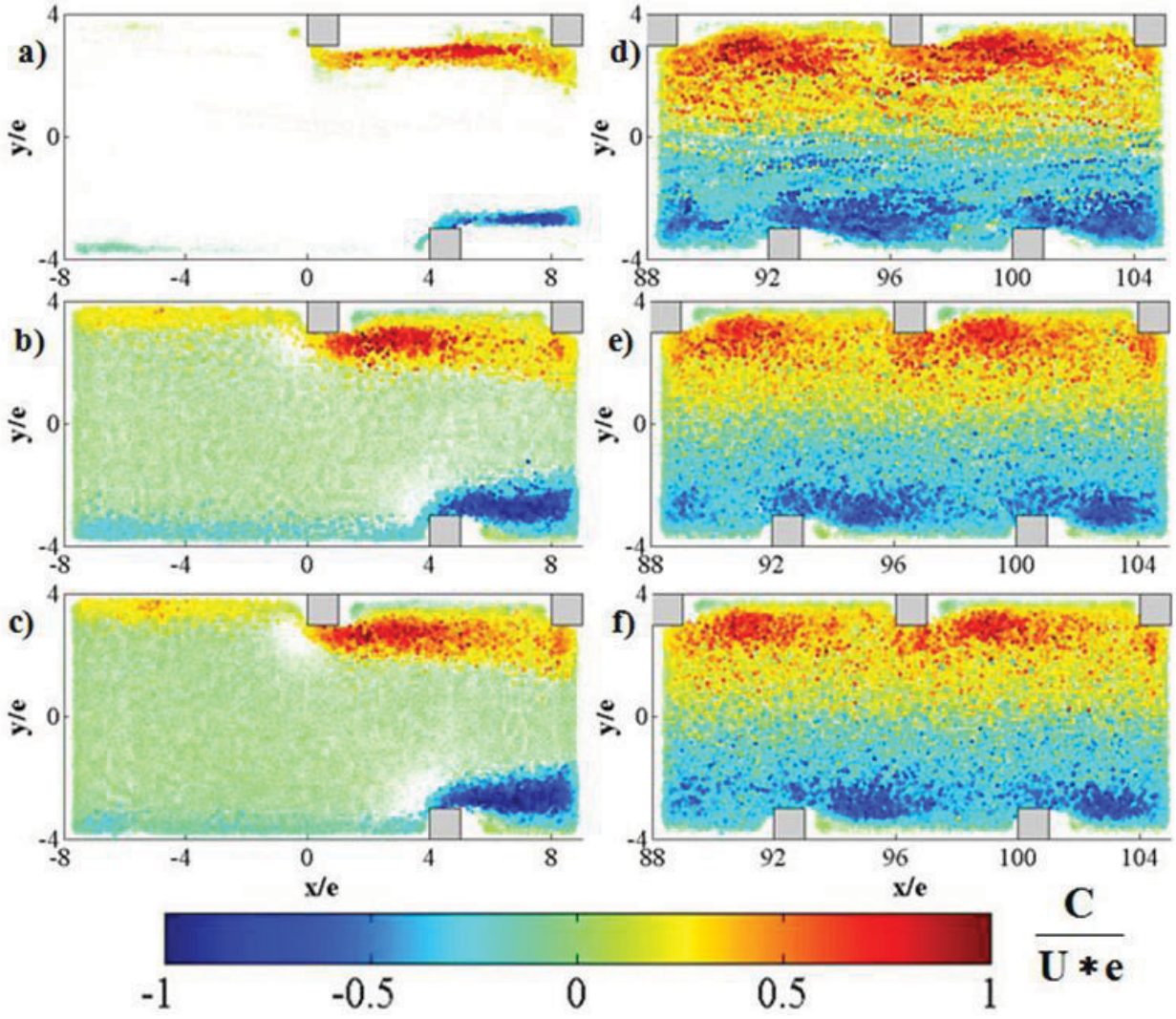

Figure 3.12. Identified coherent structures for the inlet a) Re = 2.5k-IN b) Re = 10k-IN c) Re = 20k-IN and fully developed region d) Re = 2.5k-DEV e) Re = 10k-DEV f) Re = 20k-DEV.

Within the developed region, the population of CS was more uniformly spatially distributed due to the vortices being shed from upstream ribs. A large number of high strength CS were identified within the regions bounded by the ML of each rib. The most interesting observation was the presence of high strength CS within the core flow and across the channel

centerline for all Reynolds numbers. Plotting the spanwise location of the CS versus circulation strength (Figure 3.13) illustrated that a significant number of CS with positive circulation values were observed in the lower section of the channel along with negative circulation CS in the upper section, which was not observed in the inlet. This suggests that the CS shed from the ML "survive" long enough to convect across the channel centerline, especially at Re = 2.5k where the relative inertia of the bulk channel flow was lower than at higher Reynolds numbers.

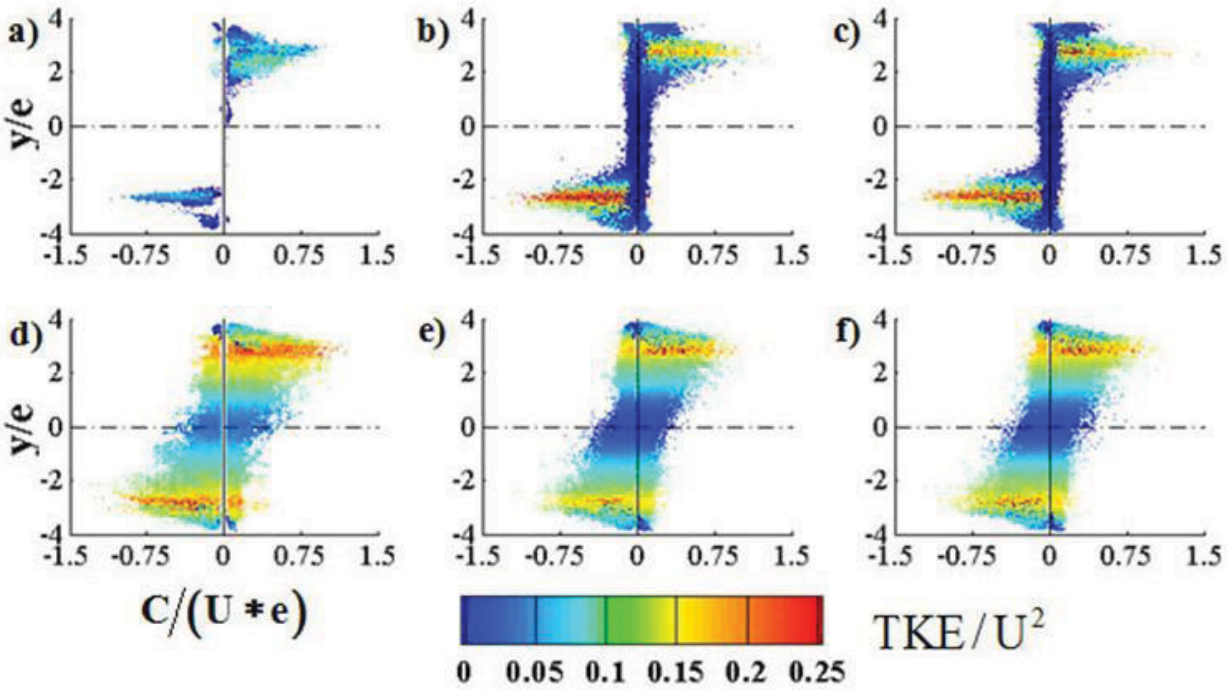

Figure 3.13. Scatter plots of vortex strength spanwise location, contoured with normalized TKE, for a) Re = 2.5k-IN b) Re = 10k-IN c) Re = 20k-IN d) Re = 2.5k-DEV e) Re = 10k-DEV f) Re = 20k-DEV.

At the inlet, approximately five times as many CS were identified at Re = 10k and 20k as compared to Re = 2.5k. However, this difference was not as pronounced in the fully developed section with Re = 10k and Re = 20k having approximately 1.7 times the number of identified CS at Re = 2.5k.

Conclusions

A study on fully-roughened and staggered rib-channel flow was performed using TRDPIV for investigating the effects of Reynolds number on the flowfield structure. In addition to the time-averaged and time-accurate flowfield results, analysis of the spatial distribution of the turbulent dissipation rate and the coherent structures populating the flow field are presented.

Observations of the mean-averaged flowfield provided information about the general character of the flow, which was dominated by the separated flow over the ribs. Several fundamental phenomena were observed as a result of the rib presence: shear layer and wake formation, regions of recirculation and reattachment of separated flow, and a strong mixing layer. At the channel inlet, a strong dependence to Reynolds number was observed in the inter-rib region, especially with regards to the separated shear layer and recirculating regions located near the first and second ribs. Within the developed region, the structure of the inter-rib region was somewhat less sensitive to changes in the Reynolds number. However, higher levels of turbulence were observed within the core flow at Re = 2.5k as compared to Re = 10k and 20k. The highest levels of turbulent dissipation, as estimated by the large eddy PIV method, were observed within the rib-generated mixing layer. Dissipation levels within the inter-rib region were shown to be sensitive to Reynolds number across the entire range tested.

The spatial distribution of coherent structures at the inlet region showed a preferential concentration within the separated mixing layer generated by the ribs. Within the fully developed region, the distribution of coherent structures was more homogeneous than at the inlet. Additionally, high strength coherent structures were observed within the bulk channel and across the channel centerline, indicating that they had been shed by successive upstream ribs and that the life of these structures was greater than their convection time across a single rib pitch.

The time-accurate flow characteristics revealed that vortices shed from the rib shear layer interact with the region of the rib wake resulting in a periodic process where the wake vortex bursts and is ejected from the inter-rib recirculation region into the core flow. This process augments the mixing and transport phenomena within the channel.

Acknowledgements

The generous support of Pratt & Whitney and technical program managers Dr. Atul Kohli, Mr. Jeff Prausa and Dr. Bill Cousins are acknowledged.

Nomenclature

General

BFR	back-flow region
C	vortex circulation
CL	channel centerline
CS	coherent structure
D_h	hydraulic diameter
DEV	fully developed channel region
e	rib height
h	channel height
IN	inlet channel region
ML	mixing layer
n_{ID}	number of identified burst events per bin
n_{total}	total number of burst events for the test case
p	rib pitch
Q1 - Q4	quadrant number
Re	flow Reynolds number, $Re = U \cdot D_h / \nu$
RMS	quadratic mean, root mean square
RR#	recirculating region
t	time
Δt	burst duration
t*	nondimensionalized time, $t^* = t / \tau_f$
ΔT	inter-burst time
ΔT^*	nondimensionalized time, $\Delta T^* = \Delta T \cdot U / e$
TKE	turbulent kinetic energy, $TKE = u'^2 + v'^2$
u	streamwise velocity component
u′	fluctuating streamwise velocity, $u' = u - U$
U	bulk streamwise velocity
v	wall-normal (spanwise) velocity component

v'	fluctuating wall-normal velocity, $v' = v - U$
w	channel width
x	channel streamwise direction
y	channel wall-normal (spanwise) direction

Greek

σ	population standard deviation
ε	turbulent dissipation rate
ω	vorticity
ν	kinematic viscosity
τ_f	characteristic fluid scale, $\tau_f = D_h / U$
Ψ	stream function

References

1. Armaly, B.F., et al., 1983, "Experimental and theoretical investigation of backward-facing step flow," Journal of Fluid Mechanics Digital Archive. 127(-1): p. 473-496.
2. Armaly, B.F., et al., 1983, "Experimental and theoretical investigation of backward-facing step flow," Journal of Fluid Mechanics Digital Archive. 127(-1): p. 473-496.
3. Le, H., et al., 1997, "Direct numerical simulation of turbulent flow over a backward-facing step," Journal of Fluid Mechanics. 330(1): p. 349-374.
4. Neto, A.S., et al., 1993, "A numerical investigation of the coherent vortices in turbulence behind a backward-facing step," Journal of Fluid Mechanics Digital Archive. 256(-1): p. 1-25.
5. Bowen, A.J. and Lindley, D., 1977, "A wind-tunnel investigation of the wind speed and turbulence characteristics close to the ground over various escarpment shapes," Boundary-Layer Meteorology. 12(3): p. 259-271.
6. Sherry, M.J., et al. 2009, "Flow separation characteristics of a forward facing step immersed in a turbulent boundary layer. " in 6th International Symposium on Turbulence and Shear Flow Phenomena. Seoul, Korea.
7. Perry, A.E., et al., 1969, "Rough wall turbulent boundary layers," Journal of Fluid Mechanics. 37: p. 383-413.
8. Jimenez, J., 2004, "Turbulent flows over rough walls," Annual Review of Fluid Mechanics. 36: p. 173-196.
9. Cui, J., et al., 2003, "Large-eddy simulation of turbulent flow in a channel with rib roughness," International Journal of Heat and Fluid Flow. 24(3): p. 372-388.
10. Wang, K.-C. and Wen-Ruey, C., 2006, "An Experimental Investigation of the Turbulence Structure of a Block-Mounted Rectangular Channel Flow," Journal of Science and Engineering Technology. 2(3): p. 9-20.
11. Wang, L., et al., 2007, "PIV Measurement of Separated Flow in a Square Channel With Streamwise Periodic Ribs on One Wall," Journal of Fluids Engineering. 129(7): p. 834-841.
12. Casarsa, L. and Arts, T. 2002, "Aerodynamic performance investigation of a Rib Roughened Cooling Channel Flow with high blockage ratio ". in 11th International Symposium on Application of Laser Techniques to Fluid Mechanics. Lisbon, Portugal.
13. Lohász, M., et al., 2006, "Flow Features in a Fully Developed Ribbed Duct Flow as a Result of MILES," Flow, Turbulence and Combustion. 77(1): p. 59-76.
14. Arts, T., et al. 2007, "Experimental and Numerical Investigation of Flow and Heat Transfer in a Ribbed Square Duct. " in 3rd International Symposium on Integrating CFD and Experiments in Aerodynamics. U.S. Air Force Academy, CO, USA.
15. Casarsa, L. and Arts, T., 2005, "Experimental Investigation of the Aerothermal Performance of a High Blockage Rib-Roughened Cooling Channel," Journal of Turbomachinery. 127(3): p. 580-588.
16. Casarsa, L., et al., 2002, "Characterization of the Velocity and Heat Transfer Fields in an Internal Cooling Channel With High Blockage Ratio," ASME Conference Proceedings. 2002(36088): p. 451-458.
17. Rau, G., et al., 1998, "The Effect of Periodic Ribs on the Local Aerodynamic and Heat Transfer Performance of a Straight Cooling Channel," Journal of Turbomachinery. 120(2): p. 368-375.

18. Chandra, P.R., et al., 2003, "Heat transfer and friction behaviors in rectangular channels with varying number of ribbed walls," International Journal of Heat and Mass Transfer. 46(3): p. 481-495.
19. Graham, A., et al. 2004, "Flow Measurements in a Ribbed Channel Relevant to Internal Turbine Blade Cooling. " in ASME Turbo Expo 2004. Vienna, Austria.
20. Han, J.C., 1988, "Heat Transfer and Friction Characteristics in Rectangular Channels With Rib Turbulators," Journal of Heat Transfer. 110(2): p. 321-328.
21. Han, J.C. and Park, J.S., 1988, "Developing heat transfer in rectangular channels with rib turbulators," International Journal of Heat and Mass Transfer. 31(1): p. 183-195.
22. Liou, T.-M., et al., 1990, "Experimental and Computational Study of Turbulent Flows in a Channel With Two Pairs of Turbulence Promoters in Tandem," Journal of Fluids Engineering. 112(3): p. 302-310.
23. Liou, T.-M., et al., 1993, "LDV Measurements of Periodic Fully Developed Main and Secondary Flows in a Channel With Rib-Disturbed Walls," Journal of Fluids Engineering. 115(1): p. 109-114.
24. Sewall, E.A., et al., 2006, "Experimental validation of large eddy simulations of flow and heat transfer in a stationary ribbed duct," International Journal of Heat and Fluid Flow. 27(2): p. 243-258.
25. Abdel-Wahab, S. and Tafti, D.K., 2004, "Large Eddy Simulation of Flow and Heat Transfer in a 90 deg Ribbed Duct With Rotation: Effect of Coriolis and Centrifugal Buoyancy Forces," Journal of Turbomachinery. 126(4): p. 627-636.
26. Kim, H.-M. and Kim, K.-Y., 2004, "Design optimization of rib-roughened channel to enhance turbulent heat transfer," International Journal of Heat and Mass Transfer. 47(23): p. 5159-5168.
27. Sewall, E.A. and Tafti, D.K., 2006, "Large Eddy Simulation of Flow and Heat Transfer in the 180-Deg Bend Region of a Stationary Gas Turbine Blade Ribbed Internal Cooling Duct," Journal of Turbomachinery. 128(4): p. 763-771.
28. Bernard, P.S. and Wallace, J.M., Turbulent Flow Analysis, Measurement, and Prediction. 2003, Hoboken: John Wiley and Sons.
29. Patel, V.C., 1998, "Perspective: Flow at high Reynolds number and over rough surfaces - Achilles heel of CFD," Journal of Fluids Engineering. 120(3): p. 434-444.
30. Huang, R.F., et al., 2007, "Flow and Heat Transfer Characteristics in Rectangular Channels With Staggered Transverse Ribs on Two Opposite Walls," Journal of Heat Transfer. 129(12): p. 1732-1736.
31. Rivir, R.B., et al., 1996, "Turbulence and Scale Measurements in a Square Channel with Transverse Square Ribs," International Journal of Rotating Machinery. 2(3): p. 209-218.
32. Adrian, R.J., 1997, "Dynamic ranges of velocity and spatial resolution of particle image velocimetry," Measurement Science & Technology. 8(12): p. 1393-1398.
33. Adrian, R.J., 2005, "Twenty years of particle image velocimetry," Experiments in Fluids. 39(2): p. 159-169.
34. Westerweel, J., 1997, "Fundamentals of digital particle image velocimetry," Measurement Science & Technology. 8(12): p. 1379-1392.
35. Eckstein, A., et al., 2008, "Phase correlation processing for DPIV measurements," Experiments in Fluids. 45(3): p. 485-500.
36. Eckstein, A. and Vlachos, P.P., 2009, "Digital particle image velocimetry (DPIV) robust phase correlation," Measurement Science and Technology. 20(5): p. 055401.

37. Eckstein, A. and Vlachos, P.P., 2009, "Assessment of advanced windowing techniques for digital particle image velocimetry (DPIV)," Measurement Science and Technology. 20(7): p. 075402.
38. Chong, M.S., et al., 1990, "A general classification of three-dimensional flow fields," Physics of Fluids A: Fluid Dynamics. 2(5): p. 765-777.
39. Hunt, J.C., et al., Eddies, streams, and convergence zones in turbulent flows. 1988, Center for Turbulence Research Report CTR-S88. p. 193.
40. Jeong, J. and Hussain, F., 1995, "On the identification of a vortex," Journal of Fluid Mechanics Digital Archive. 285(-1): p. 69-94.
41. Adrian, R.J., et al., 2000, "Analysis and interpretation of instantaneous turbulent velocity fields," Experiments in Fluids. 29(3): p. 275-290.
42. Sheng, J., et al., 2000, "A large eddy PIV method for turbulence dissipation rate estimation," Chemical Engineering Science. 55(20): p. 4423-4434.
43. Sharp, K.V. and Adrian, R.J., 2001, "PIV study of small-scale flow structure around a Rushton turbine," AIChE Journal. 47(4): p. 766-778.
44. Smagorinsky, J., 1963, "General Circulation Experiments with the Primative Equations," Monthly Weather Review. 91(3): p. 99-164.
45. de Jong, J., et al., 2009, "Dissipation rate estimation from PIV in zero-mean isotropic turbulence," Experiments in Fluids. 46(3): p. 499-515.
46. Etebari, A. and Vlachos, P., 2005, "Improvements on the accuracy of derivative estimation from DPIV velocity measurements," Experiments in Fluids. 39(6): p. 1040-1050.
47. Karri, S., et al., 2009, "Robust wall gradient estimation using radial basis functions and proper orthogonal decomposition (POD) for particle image velocimetry (PIV) measured fields," Measurement Science and Technology. 20(4): p. 045401.
48. Figliola, R.S. and Beasley, D.E., Theory and Design for Mechanical Measurements. 2006, Hoboken, NJ: John Wiley and Sons Inc.
49. Harder, K.J. and Tiederman, W.G., Influence of wall strain rate, polymer concentration, and channel height upon drag reduction and turbulent structure. 1989, Purdue University. p. Technical Report PME-FM-89-1.
50. Harder, K.J. and Tiederman, W.G., 1991, "Drag Reduction and Turbulent Structure in Two-Dimensional Channel Flows," Philosophical Transactions: Physical Sciences and Engineering. 336(1640): p. 19-34.
51. Moser, R.D., et al., 1999, "Direct numerical simulation of turbulent channel flow up to Re[sub tau] = 590," Physics of Fluids. 11(4): p. 943-945.
52. Spalding, D.B., 1961, "A single formula for the law of the wall," Journal of Applied Mechanics. 28(3): p. 455.
53. Bogard, D.G. and Thole, K.A., Wall-Bounded Turbulent Flows, in The Handbook of Fluid Dynamics, R.W. Johnson, Editor. 1998, Springer-Verlag: Heidelberg, Germany. p. 49-63.
54. Bogard, D.G. and Tiederman, W.G., 1986, "Burst detection with single-point velocity measurements," Journal of Fluid Mechanics. 162: p. 389-413.
55. Bogard, D.G. and Tiederman, W.G., 1987, "Characteristics of ejections in turbulent channel flow," Journal of Fluid Mechanics. 179: p. 1-19.
56. Robinson, S.K., 1991, "Coherent Motions in the Turbulent Boundary Layer," Annual Review of Fluid Mechanics. 23(1): p. 601-639.

57. Wallace, J.M., et al., 1972, "The wall region in turbulent shear flow," Journal of Fluid Mechanics. 54(01): p. 39-48.
58. Wallace, J.M. and Lu, S.S., 1972, "Structure of the Reynolds stress near the wall," Journal of Fluid Mechanics. 55(01): p. 65-92.

Paper 4: Evaluation of a Hybrid Particle Tracking Velocimetry Algorithm (PTV) Combined with Digital Particle Image Sizing (DPIS)

Final manuscript in submission to *Measurement Science and Technology*[*]

Abstract

The complex dynamics present in multiphase flows are often insufficiently understood and, therefore, provide a rich area of study both in theoretical understanding and practical application. Practical examples of these flows include the ingestion of foreign particulates in gas turbines and targeted drug treatment within the human body. Experimental investigation of multiphase flows, however, is not straightforward and requires special techniques focusing on the simultaneous resolution of both the carrier and discrete phases present in the flowfield.

The new method presented in this paper, a multi-parametric particle pairing algorithm for particle tracking velocimetry (MP3-PTV), provides a powerful technique for the measurement of multiphase flows. After imaging the particles present in a multiphase flow with a high-speed laser and camera system, the MP3-PTV employs a variable pair-matching algorithm which utilizes displacement preconditioning in combination with estimated particle size and intensity to match particle pairs between successive images. To improve the method's efficiency, a new particle identification and segmentation routine was also developed.

Validation of the new method was initially performed on two artificial data sets: a traditional single-phase flow published by the Visualization Society of Japan (VSJ) and an in-house generated multiphase flow having a bi-modal distribution of particles diameters. On the VSJ data set, the newly presented segmentation routine performed very well delivering a two-fold increase in identifying particles when compared to other published methods. Metrics of the measurement yield, reliability and overall tracking efficiency were used for method comparison. For the simulated multiphase flow data set, measurement efficiency of the carrier phases improved from 9% to 41% for MP3-PTV as compared to traditional hybrid PTV.

When employed on experimental data of a gas-solid flow, the MP3-PTV effectively segregated the two particle populations and reported a vector efficiency and velocity error equivalent to measurements for the single-phase images. Simultaneous measurement of particle

*Co-authors: Dr. Pavlos P. Vlachos, Mechanical Engineering Department, Virginia Tech
Dr. Karen A. Thole, Mechanical and Nuclear Engineering Department, Penn State

and carrier flowfield velocities allowed for the calculation of instantaneous particle slip velocities. This method of measurement illustrated the algorithm's capability to robustly and accurately process PTV images for a variety of traditional and nontraditional image conditions.

Introduction

The investigation of multiphase flows is of considerable interest to the scientific and engineering community. Despite numerous advancements in the field, there is still a need for robust non-invasive experimental multiphase flow techniques. The desired method would be able to simultaneously resolve the velocity of the carrier and discrete phases as well as providing size and shape information for the discrete phase [1-3]. Phase Doppler Particle Analyzer (PDA/PDPA) was traditionally used for simultaneous velocity and size measurements. However, PDPA is limited by the assumption of spherical droplets/particles [4, 5] and is a point measurement technique. More recently, Particle Image Velocimetry (PIV) and Particle Tracking Velocimetry (PTV) have gained wide acceptance for spatiotemporal measurements in multi-phase flows [6, 7]. In this work, a methodology was developed that significantly augments the capability and accuracy of PTV/PIV experiments towards resolving complex multi-phase flows, in particular when the dispersed phase does not follow the main flow. Such conditions often impose insurmountable challenges for conventional PTV/PIV methods.

PIV [8-10] employs a locally windowed cross-correlation between two successive images to determine the displacement of particle patterns. While it is effective in the measurement of single-phase flows, the extension of PIV to measuring multiphase flows is very challenging, especially when the motion of the carrier and discrete phases do not correlate well with one another. Moreover, the local velocity estimation tends to be biased towards the velocity of the largest and brightest particles within the pattern.

PTV, unlike PIV, relies on the direct tracking of individual particles between successive images. By this methodology, the motions of each phase may therefore be measured independently of the other, assuming phase discrimination is possible. Early PTV methods involved tracking particles through four-or-more consecutive images [7, 11] and regularly employed schemes for the minimization of trajectory length and angular deviation. While comparatively robust, the tracking yield of these methods was low in comparison to the number of possible measurements. Also proposed was the binary image cross-correlation [12, 13]. For this method, a windowed cross-correlation, centered on each particle, was performed between the two images which provided a displacement estimate. Another two-frame PTV method proposed the use of a heuristic match probability to determine the most probable trajectories [14]. This two-frame method was found to be an improvement over the traditional four-frame

methods in terms of computation expense, tracking yield, and allowable dynamic ratio. Similar to the heuristic match method, a "fuzzy logic" PTV algorithm has also been proposed [15]. It is important to note that all previously mentioned PTV methods rely on a smoothness parameter, indicating *a-priori* knowledge of the flowfield which is not always available for multiphase flows.

Several methods utilize an initial PIV analysis of the flowfield to provide a "first guess" for the particle trajectories [16, 17]. These methods, often referred to as "super-resolution PIV" or "hybrid PIV/PTV", showed significant increases in the tracking yield and dynamic range for densely seeded flows. Other super-resolution methods have been presented which utilize improved particle matching techniques, such as Kalman filtering [18] and an improved global interpolation scheme [16]. The previously described match probability method [14] has also been presented as a hybrid scheme [19] which showed improvements in vector yield. However, it should be emphasized that these methods would be unable to track particles that do not behave as flow tracers, owing to their heavy reliance on PIV-derived predictions of the particle velocities.

Several two-frame PTV algorithms have been presented that do not rely on a PIV-derived velocity estimate. The relaxation algorithm [20] is an improvement over the original relaxation method [21] for both the tracking algorithm and particle identification scheme. An iterative variational approach [22] was also proposed which makes use of a local regularization of the estimated particle trajectories to progressively improve the tracking efficiency. While effective, the algorithm required a large number of iterations (over 700) for a single image pair before a suitable convergence was achieved which significantly increases the computational cost of this method. A recent PTV method, referred to as enhanced particle tracking velocimetry (EPTV) [23], was shown to improve tracking reliability by utilizing the measured particle intensity information in combination to the particle position proximity, as two parameters of enhanced particle pair matching. The incorporation of particle-related information helped increase tracking efficiency significantly. Although this method appears to outperform all previously reported PTV methods, little attention was given on quantifying the actual error of the velocity measurements.

The objective of this paper is to introduce a new PTV algorithm that is aimed towards enhancing the capability for resolving multiphase flows and in particular situations under which

the disperse phase does not follow the carrying flow, and provide detailed error analysis and validation in order to demonstrate the method advantages and possible limitations. The improvements of the method consist of a new and more robust particle segmentation procedure and an augmented multi-parameter particle pairing approach incorporating particle image sizing methodologies [24]. We show that the combination of particle position, size and intensity within the particle pairing process results in significant performance improvements when compared to previously reported results.

Particle Tracking Methodology

The PTV implementation presented herein, named Multi-Parametric Particle Pairing (MP3-PTV), is designed for use with single-exposure images. As illustrated in Figure 4.1, the MP3-PTV algorithm requires the following steps: image pre-processing, particle identification, particle sizing, displacement preconditioning, particle pairing, and validation of velocity measurements. With modification, the methods described could also be implemented for multi-exposed images or tracking with more than two frames. However, these were not explored herein.

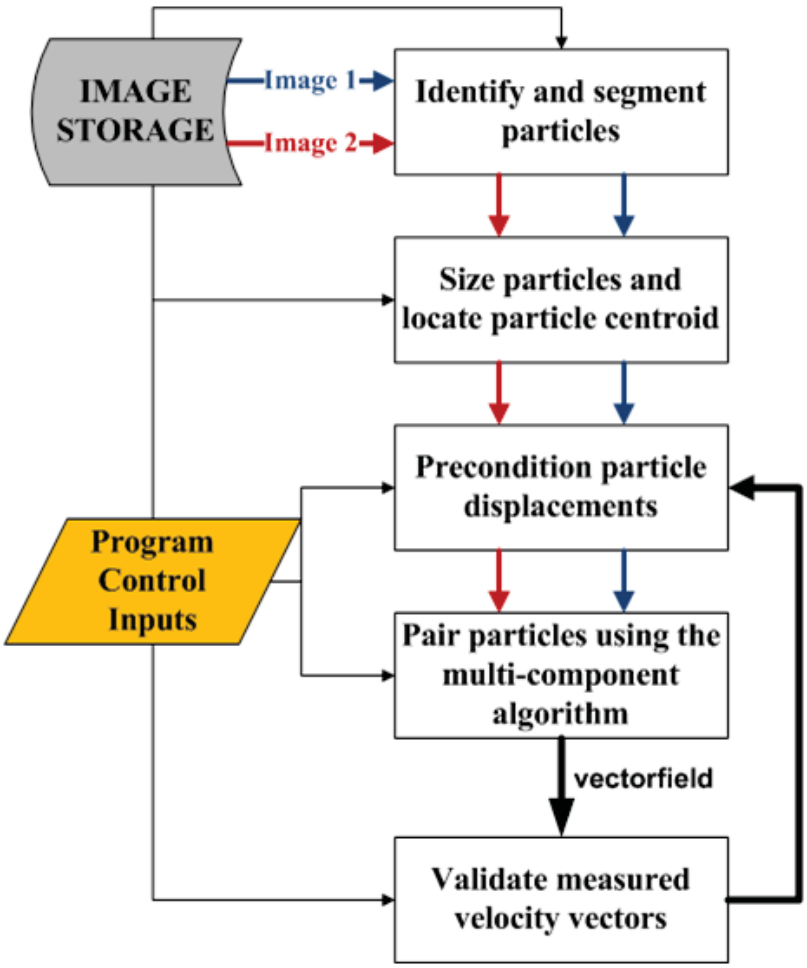

Figure 4.1. Flowchart illustrating the individual processes of the MP3-PTV algorithm.

Multi-Parameter Particle Pair Matching

For the MP3-PTV, three particle-related parameters are estimated and used for the pair matching: particle diameter (d), maximum "true" intensity (I), and distance from the estimated particle position (D). For each particle in frame one, a matching coefficient (C_{12}) is computed in association to each particle located in frame two, bounded within a user-defined search radius, r_s, centered on the particle's estimated location in frame two, as shown in Eq. 1.

$$C_{12} = \left[W_d \left(\frac{|d_1 - d_2|}{d_{max} - d_{min}} \right) + W_I \left(\frac{|I_1 - I_2|}{I_{max} - I_{min}} \right) + W_D \left(\frac{D}{r_s} \right) \right] \Big/ \left(W_d + W_I + W_D \right) \quad (1)$$

The difference in each matching parameter (d, I, and D) is normalized by its maximum possible value between frame one and frame two. A set of variable weighting factors, W_d W_I and W_D, are placed on each pair-matching parameter. In doing so, the relative emphasis on each

parameter can be adjusted to match the image properties. For example, it would be prudent to decrease W_d for a monodisperse particle size distribution as the particle diameter will provide limited information for pair-matching. The opposite would be true when dealing with a broad distribution of particle sizes. For images with abrupt spatial variations in laser intensity, W_I should be decreased. Setting W_d and W_I to zero reduces the pair-matching to a simple nearest-neighbor algorithm. When operating as a nearest-neighbor algorithm with displacement preconditioning, the search radius is set to the theoretical optimal value of $\sqrt{\pi}*d_t$, as defined by Keane et al. [17], where d_t is the imaged particle diameter. Lastly the matching coefficient is normalized by the sum of the weighting factors. This normalization assures a value of C_{12} between zero and one, where zero indicates a perfect match and a value of one implies the worst possible match.

Once computed for all possible particle pairs, the matching coefficients are arranged in ascending order. Pair matching begins with the lowest value of C_{12} and continues until the maximum number of measurable matches is met or the number of possible matches has been exhausted. The maximum number of measureable matches between a given frame pair is equal to the number of particles in either frame one or frame two, depending on which is the lesser value. As each particle in frame two is matched, it is removed from all possible matches with other particles in frame one thus assuring that each particle pairing is unique.

Particle Identification and Segmentation

Previous Particle Identification Methods

The simplest and most commonly utilized method for particle identification is the single-value threshold binarization (SVT). The SVT groups adjacent pixels in the images into a particle, providing the pixel intensity value is above a global threshold level. This method is fast and easy to implement. SVT, however, has serious limitations, notably an inability to cope with overlapped particles and uneven image illumination. Locally varying threshold values, referred to as multiple threshold binarization, can be used to partially correct uneven illumination. This method does not, however, adequately address overlapped particles within the flowfield which is a vital aspect when dealing with simultaneously seeded multiphase flows and at high seeding densities.

The dynamic threshold binarization detection method [20] is an improvement over the single and multiple threshold binarization. The algorithm efficiently handles uneven illumination and overlapped particles by locally adjusting the threshold value of each particle until the mean intensity level (gray level) is less than a preset contrast level. While an enhancement over other binarization methods, the dynamic threshold binarization often truncates the particle image which has implications with regards to particle sizing. A modification to this method has also been proposed [23] that utilizes the maximum particle intensity level instead of the mean for comparison with the preset contrast level. However, we have found this method not to perform robustly when discriminating and separating overlapping particles.

Another particle segmentation technique is the particle-mask correlation [25]. For this method, a cross-correlation of a generic two-dimensional particle profile is performed for all pixels with subareas of high correlation taken as identified particles. This method effectively separates overlapped particles as well as handling uneven illuminations; however, it is sensitive to image noise, which can lead to a high rate of misidentifications. In addition, the method would likely have difficulty operating with a broad distribution of particle diameters, such as during the measurement of multiphase flows.

Erosion/Dilation Thresholding

A method, which we term here as erosion/dilation thresholding (EDT), is proposed for particle identification and segmentation. The EDT is based on two commonly utilized morphological operations related to image processing: erosion and dilation. In the field of mathematical morphology, the intensity profile of a two-dimensional grayscale image is often referred to as an "elevation" above the image plane. Using the elevation analogy, an efficient peak-finding routine can be achieved by eroding the landscape until the peaks are brought down to the base level. For the EDT, this erosion is accomplished by a variable structuring element (SE) which is iteratively subtracted from the image intensity distribution. Initially, the global value of the structuring element is set to one. Once a local peak has been identified, it is shielded from subsequent erosion by setting the SE value to zero at that location. For a global SE value of 1, the number of erosion steps required to identify all particle peaks is equal to the image intensity (256 for an 8-bit grayscale image). Increasing the global SE value beyond a value of

one reduces the number of required erosions steps and, therefore, the computational requirement. Maintaining a value of one, however, assures that all local peaks will be identified.

After the image erosion, an iterative dilation of the eroded image is performed in which adjacent pixels to the peaks are successively added to each peak. The dilation of each identified peak is based upon the following rules:

1. Pixels previously assigned to a peak cannot be reassigned.
2. Expansion of each pixel can only extend by one adjacent pixel in each direction per dilation step.
3. Intensity ratio of the adjacent pixel to the expanding pixel must be less than one.

Rules 1 and 2 allow for a controlled expansion of each peak. Rule 3 prevents an expanding particle from claiming unassigned pixels belonging to an adjacent particle. Particle dilation then continues iteratively until the intensity value of the adjacent pixels falls below a user defined minimum threshold level. This process assures the maximum information is available for subsequent use with the particle sizing algorithms.

Particle Sizing

Six previously presented digital particle image sizing methodologies (DPIS) were assessed within the current study. Two of the methods are classical implementations for sizing particle images: intensity weighted centroid and three-point Gaussian [26]. The four remaining methods are recent implementations that have been shown to reduce the errors associated with DPIS [24]. A short discussion of each method is provided below for completeness. For details and further clarification of these sizing methods, the reader is directed to the work by Brady et al. [24].

Intensity Weighted Centroid (IWC) and Pixel Counting

Both the IWC and pixel counting are fast and easy to implement methods for computing the centroid and diameter, respectively, of an imaged particle. While robust, their measurement accuracy has been shown to be sensitive to the image quality and overly aggressive thresholding can compromise their effectiveness. This issue can be particularly problematic when the SVT identification method is used, since aggressive thresholding is required in order to separate overlapped particles.

Discrete Gaussian Methods

From optical theory it is accepted that the distribution of reflected light for particles imaged by a coherent light source is described by an Airy point spread function [27]. The three-point Gaussian (TPG) fitting scheme makes use of this approximation by fitting a one- or two-dimensional Gaussian curve to the maximum intensity pixel and four adjacent pixels [26]. As with the IWC, the TPG method is fast and easy to implement. It performs poorly, however, when applied to large particle images and over-saturated particles, both of which are common when dealing with simultaneously seeded multiphase flows.

The four-point Gaussian (FPG) is a two-dimensional fitting scheme developed by Brady et al. [24] to overcome limitations with the traditional TPG method, specifically the inability to deal with saturated particle images. This improvement is accomplished through a pixel selection routine that selects only unsaturated pixels. Additionally, the pixel selection for the FPG is governed by a set of rules that assure the solution is non-trivial. The FPG is still limited given that it only utilizes a total of four pixels for particle centroid and diameter measurement.

Brady et al. [24] also presented a least-squares Gaussian fitting scheme (LSG) that utilized all available pixels for the measurement of particle centroid and diameter. Least-squares minimization methods are regularly used for solving overdetermined systems, which correctly describes the fitting of a Gaussian distribution to a noisy particle image. Performance of the LSG method is superior to other least-squares fitting schemes [26] given that it utilizes the maximum amount of information available in the particle image.

Continuous Gaussian Methods

Pixel intensity discretization also contributes to error associated with particle sizing. The previously described sizing methods assume that the measured intensity value at each pixel center is equal to the true intensity reported. In reality, the measured intensity value is equal to the intensity value integrated over the pixel area plus the sensor noise. This difference between measured and true intensity introduces significant errors with regard to particle centroid and size estimation. A continuous four-point Gaussian (CFPG) and continuous least-squares Gaussian (CLSG) fitting schemes [24] are an improvement over the previously described FPG and LSG methods as they compare the integrated intensity value at each pixel location to the measured value. In doing so, the methods compute the “true” intensity value at each pixel location. This is

of particular importance for this study given that the MP3-PTV uses particle intensity as a particle matching parameter.

The work by Brady et al. [24] was focused on determining the accuracy of these methods for particle sizing only and their utility for velocimetry applications was not explored in detail. Therefore, for completeness, the dependence of the MP3-PTV accuracy to the choice of particle position and diameter estimation method was considered herein.

Inter-Frame Displacement Preconditioning

Providing an estimate of the particle displacement increases the likelihood of correctly matching particles between frames, especially for high particle densities. The MP3-PTV method shown here considered three methods for displacement preconditioning, as described below.

Hybrid PTV-PIV

Previous researchers have shown that the use of a PIV-derived estimate of particle displacement greatly increases the allowable measurement density for PTV [16, 17]. Following this methodology, a PIV analysis was performed on the flowfield prior to pair-matching. The accuracy of the PIV analysis is, therefore, very important given that an invalid measurement will cascade into multiple errors during particle pairing. For the work presented here PIV processing was carried out using the robust phase correlation (RPC) [28, 29]. Once the PIV velocity field has been computed, an interpolation is required to provide a displacement estimate for each individual particle. A cubic spline interpolation was performed for each particle centroid, resulting in an estimated particle velocity at that location. This velocity, along with the inter-frame time, provided a displacement estimate for each particle.

Preconditioning using previous particle tracking velocity estimation

The particle velocity distribution measured from a previous image pair by PTV was also utilized as a displacement estimate. It is important to note that utilizing the previously measured particle velocities assumes that the flowfield is temporally well-resolved.

Since the measured particle velocities are irregularly distributed, a distance-weighted average was employed for the neighboring particle velocities. Within a user-defined search radius (r_S), the velocities were weighted with a radially symmetric Gaussian distribution, A(r), centered on the prediction location. The standard deviation of the Gaussian was set such that the

value of the function at r_S matched the user-defined value. Calculation of the particle velocity estimates, u_i and v_i, are shown in Eq. 2

$$\begin{aligned} A(r) &= e^{-r^2/2\sigma^2} \\ \sigma &= \sqrt{-\left(r_s^2\right)/\left(2\ln\left[A(r_S)\right]\right)} \\ u_i &= \sum A(r)*u(x,y)/\sum A(r) \\ v_i &= \sum A(r)*v(x,y)/\sum A(r) \end{aligned} \tag{2}$$

No Displacement Estimation

The presented MP3-PTV algorithm also has the capability to operate without any estimation of particle displacement. This is appropriate when dealing with particle motion that does not locally correlate with the motion of adjacent particles (i.e. random trajectories).

Outlier Detection and Validation

Flowfield measurement by PIV and PTV typically requires a data validation step where each velocity vector is labeled as either valid or invalid and replaced if necessary. Numerous studies have sought to address the validation of planar PIV data [30-33]. The MP3-PTV algorithm makes use of two validation methods, one based on the deviation of each measurement from the local population and one utilizing the pair-matching coefficient (C_{12}).

Statistically comparing each vector to its surrounding velocities is a common method for detecting erroneous measurements for PIV. The MP3-PTV employs the "universal median test" [32, 33] which compares the median deviation of the measured vector to the median absolute deviation (MAD) of the surrounding vectors as defined by the search radius, r_S. Once an outlier has been detected, the displacement estimate (preconditioning) is updated using the median value of the local population. The pair-matching and validation steps repeat iteratively until all prescribed validation steps are completed.

Validation was also performed using the matching coefficient, C_{12}, as a low-pass filter. C_{12} is an ideal parameter for validation given that it represents how well the particles match each other with respect to size, intensity and estimated displacement. An appropriate threshold value for C_{12} can be made through observations of either a single tracking step or the ensemble-averaged results over multiple steps.

Benchmarking Against Previous PTV Algorithms

Images provided by the PIV-STD Project were chosen to initially test the MP3-PTV. The PIV-STD Project, supplied by the Visualization Society of Japan (VSJ) [34, 35], provides simulated PIV image sets for the evaluation and testing of different processing algorithms. This section describes the selected VSJ image set as well as the testing and subsequent performance of the MP3-PTV when employed as a conventional algorithm on a single-phase turbulent flowfield.

Visualization Society of Japan (VSJ) Standard Images

The specific set chosen for evaluation in this study was VSJ#301: transient three-dimensional jet shear flow. This image set has been used by other researchers for the development of PTV algorithms [7, 13, 20-23]. Figure 4.2 shows ten overlapped images from the VSJ#301 to illustrate the particle trajectories. A summary of the image parameters used to generate the VSJ#301 are shown in Table 4.1.

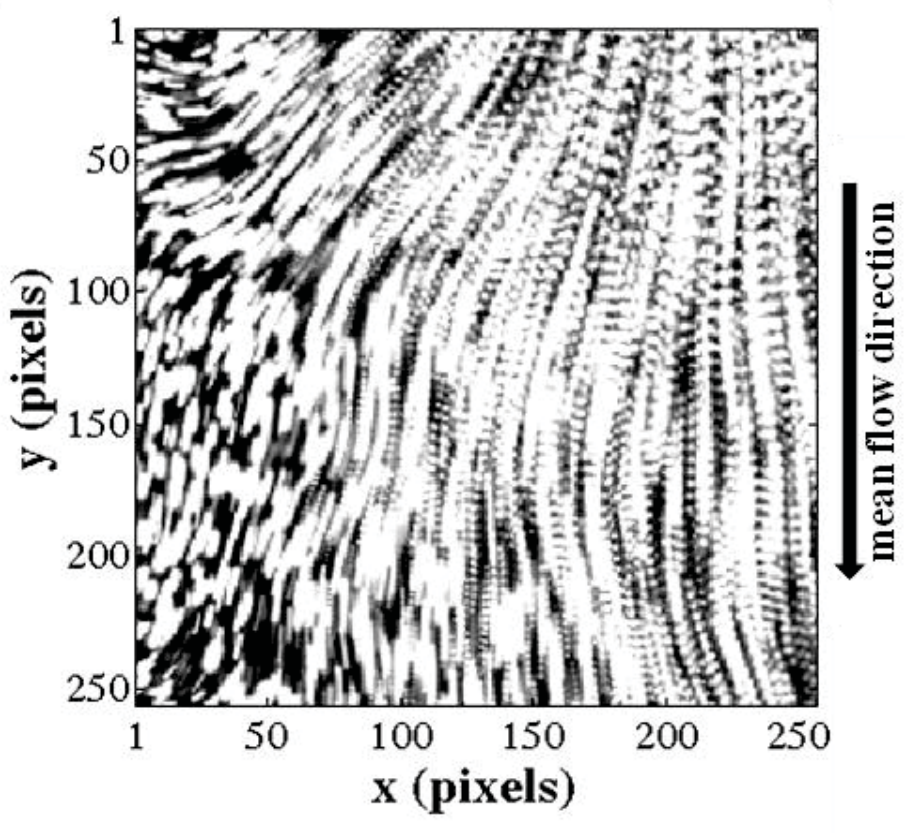

Figure 4.2. Flowfield visualization created by overlapping images 1-10 of the VSJ#301.

Table 4.1. Image Properties for VSJ#301

VSJ#301		(units)
Image Size	256 x 256	pixels
Imaged Area	4 x 4	cm
Laser Thickness	2	mm
Interframe Time	0.005	sec
Max Velocity (in-plane)	10	pix/interval
Max Velocity (through-plane)	1.5	pix/interval
Particle Diameter	about 5	pixels

Results for the Published VSJ#301

The following subsections provide results of an error analysis regarding the different identification, sizing, and tracking modes of the MP3-PTV as applied to the VSJ#301. In addition to calculating measurement yield and reliability, the particle velocity error was also quantified. All presented results were averaged over 10 images of the VSJ#301, contributing over 22,000 measurable particles to the mean statistics.

Particle Identification

Recalling Figure 4.1, the first task is to locate and segment the individual particle images. When using the SVT, the image thresholding was varied from 1-100 to determine the most efficient level for separating overlapped particles, which was I_{th} = 50 counts. This "optimal" thresholding level was chosen as it resulted in the maximum number of identified particles independently identified within a single image. It is important to note the EDT does not require trial and error to determine an "optimal" initial thresholding value. Given that the VJS#301 images were simulated without noise, an initial image thresholding was not applied when using the EDT. Figure 4.3 illustrates the typical results of the particle identification step using both the SVT and EDT algorithms for a cropped region of frame one.

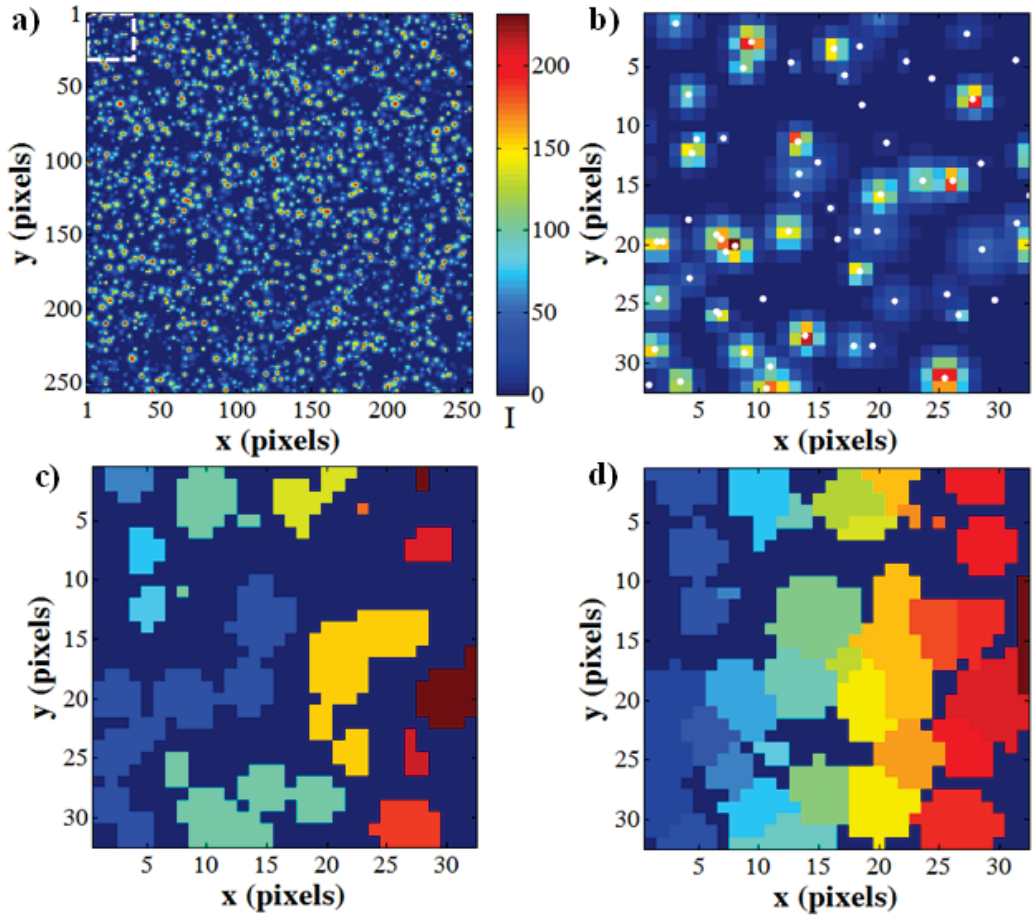

Figure 4.3. Segmentation of IM1 of the VSJ#301: a) original image, b) cropped region with known particle locations marked with white dots, c) SVT segmented particles with I_{th}=10, d) EDT segmented particles with I_{th}=0.

Comparing Figure 4.3c (SVT) and Figure 4.3d (EDT), the superior ability of the EDT to separate overlapped particles is readily apparent. In addition, the EDT preserved more of the particle information as it did not require high threshold levels for particle separation, as did the SVT. For the EDT, the number of identified particles for the first two frames was 2111 and 2099, respectively. The actual number of locatable particles in each image was estimated assuming that a particle will occlude an adjacent particle located within one-half of its diameter. Following this method for the first VSJ#301 image, the number of locatable particles is approximately 2200 out of the 4000 available, compared to 2111 located particle using the EDT. From this result, it was concluded that the maximum number of particles have been extracted from each image using the EDT while in contrast approximately 50% of the maximum were extracted using the SVT.

Particle Sizing

The number of sized particles returned by each method, as described in the previous section, is given in Figure 4.4. Also illustrated in Figure 4.4 are the maximum number of identifiable particles as well as the number of particles identified by the EDT (n_I) and the segmentation by EPTV [23]. The number of identified particles will equal the number of sized particles (n_S) if the sizing method never fails, as is the case with the IWC. All other sizing methods are subject to constraints which can preclude them from successfully sizing all identified particles. After the IWC, the LSG and CLSG sizing methods performed best, particularly when coupled with the EDT. Using the SVT in conjunction with the Gaussian sizing methods resulted in a dramatic drop in the number of sized particles versus the IWC. This drop resulted from the aggressive thresholding that cropped the particle images considerably.

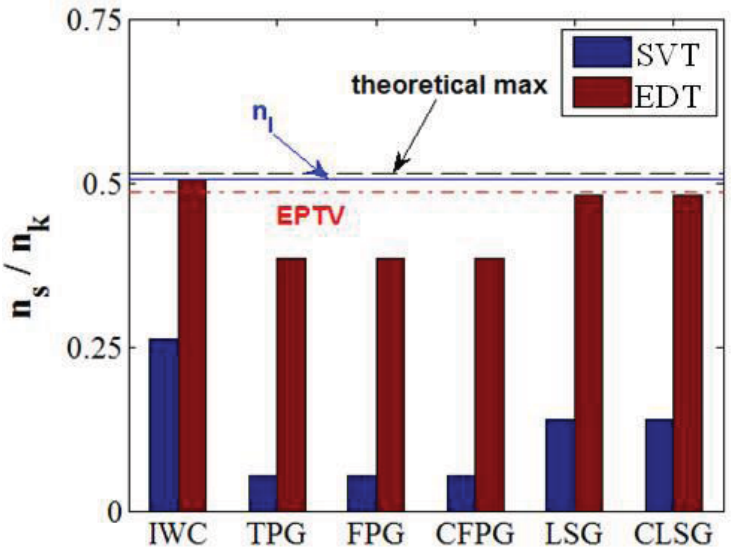

Figure 4.4. Performance comparison of the different particle identification and sizing methods.

Figure 4.5a, showing the particle size distributions for all methods, illustrates the enhanced performance of the EDT identification and LSG/CLSG sizing methods. The IWC showed a measurement diameter bias of ~1.5 pixels as compared to the other methods for the EDT, which was not unexpected given the previously published performance of the IWC. The measured diameter distribution reported for EPTV [23] is also shown in Figure 4.5a. Severe peak locking was observed when using the SVT, especially with the IWC, TPG, FPG, and CFPG sizing methods. Overall, the size distributions for the measured particles found by LSG and CLSG were somewhat insensitive to the particle identification method.

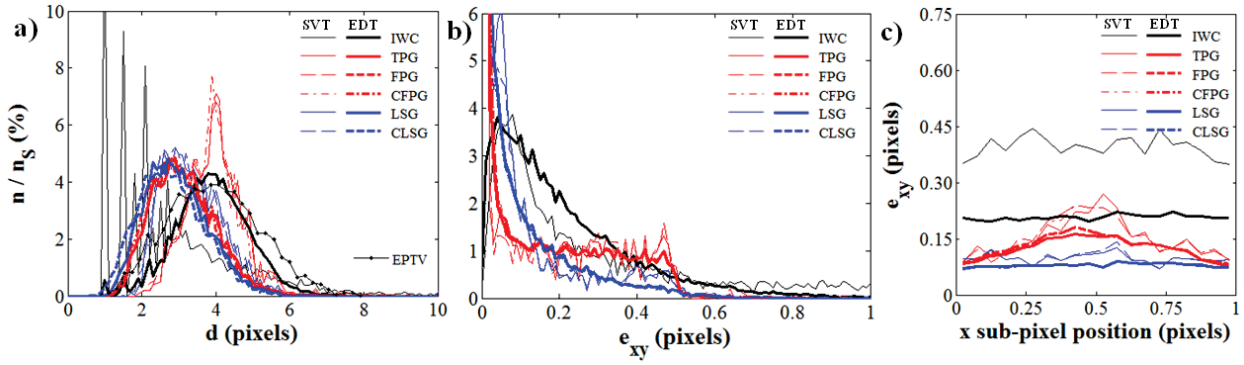

Figure 4.5. Comparison between the SVT and EDT VSJ#301 results for a) measured particle size distributions, b) histogram of position error, and c) position error versus sub-pixel particle position.

The EDT also provided a more accurate measurement of the particle centroid than the SVT, as shown in Figure 4.5b and Table 4.2. The position error, e_{xy}, of the IWC sizing method was the most sensitive to the particle identification method, as evidenced by the 2X decrease in e_{xy} between the SVT and EDT. A decrease in e_{xy} was observed for all sizing methods when utilizing the EDT, a result of the increased available particle information and lower incidence of overlapping. The position error in relation to the sub-pixel location of the known particle is also shown in Figure 4.5c. Peak locking was again observed for the TPG, FPG, and CFPG.

Table 4.2. Average Position Error and Measured Peak Intensity Error for the VSJ#301 (Acronyms Defined in the Nomenclature)

		e_{xy} (pix)	e_I (counts)	$e_{RMS,xy}$	$e_{RMS,I}$
SVT	IWC	0.40	-22.3	0.46	43.1
	TPG	0.15	-13.9	0.21	13.1
	FPG	0.15	-12.6	0.20	14.5
	CFPG	0.15	-6.7	0.20	16.4
	LSG	0.10	-11.3	0.16	14.5
	CLSG	0.10	3.6	0.17	16.7
EDT	IWC	0.21	-26.7	0.18	30.6
	TPG	0.12	-19.0	0.16	20.5
	FPG	0.13	-17.0	0.16	20.5
	CFPG	0.13	-6.2	0.16	22.0
	LSG	0.08	-16.3	0.12	21.3
	CLSG	0.08	0.2	0.12	18.0

The error in measured maximum intensity, (e_I), is also shown in Table 4.2. The intensity error was somewhat insensitive to the particle identification method, indicating that aggressive thresholding does not affect the measurement of maximum particle intensity. The continuous Gaussian sizing methods (CFPG and CLSG) exhibited the lowest e_I, owing to their unique treatment of the particle image.

The results of the previously described error analysis confirmed that the most accurate combination of particle identification and sizing methods was the EDT and CLSG, respectively. The remaining results of the VSJ#301, therefore, are presented utilizing these methods.

Particle Pairing (Velocity Measurement)

Similarly to previous works [20, 23], quantification of particle pairing effectiveness was evaluated through the total measurement yield, E_Y, and reliability, E_R, as shown in Eq. 3. The yield was defined as the ratio of measured particle trajectories (D) to the total number of known trajectories (V) while reliability was defined as the ratio of correctly identified (N) to the total number of measured particle trajectories (D).

$$E_Y = D / V \text{ , } E_R = N / D$$
$$E_F = E_Y \times E_R \tag{3}$$

Also introduced was a new metric, measurement efficiency (E_F), which was defined as the product of the yield and reliability.

Initially, pairing was completed with no displacement preconditioning, the results of which are shown in Figure 4.6, to evaluate the MP3-PTV without *a priori* knowledge of the flowfield. A uniform weighting of the pair matching parameters was utilized along with a second window search radius of 10 pixels, which was greater than the max given displacement for the image pairs.

Without validation (Figure 4.6) the vector yield, E_Y, was uniform across all cases; an expected result since E_Y is a function of the number of identified trajectories. With intermediate validation (Figure 4.6), both E_Y and E_R increased as additional matching parameters were added. For all pair-matching methods, E_Y was lower with validation than without, but this decrease was small for the three-component method. The vector reliability, E_R, was considerably higher with validation than without, with levels approaching 95% for the three-parameter method (NN-d-I). Taking into account both yield and reliability, the vector efficiency, E_F, of the three-parameter method was ~40%. This result was considerable, given that no displacement preconditioning

was provided and the maximum theoretical efficiency was ~50%, based on the number of identifiable particles in each image.

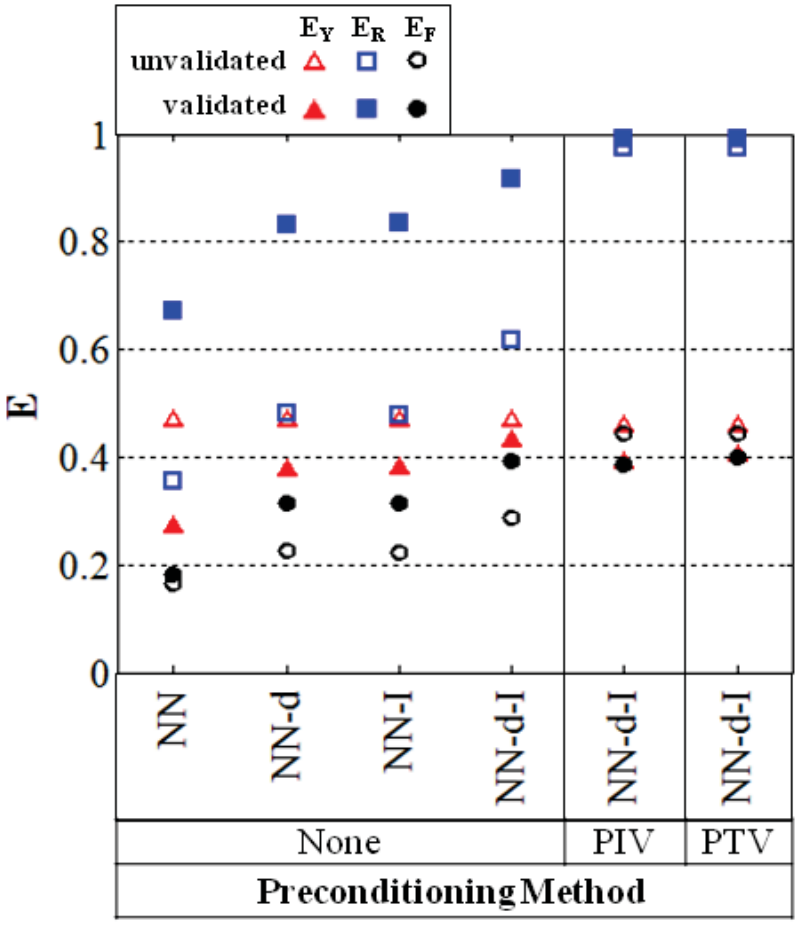

Figure 4.6. Performance of the MP3-PTV algorithm for the VSJ#301 images.

The effect of displacement preconditioning was also investigated using PIV and previous PTV. Processing parameters for the PIV displacement preconditioning are shown in Table 4.3. Only results for the NN-d-I pair-matching method are shown. The vector yield, reliability, and efficiency without intermediate validation are shown in Figure 4.6. Applying a displacement estimate increased E_R by ~54% over the results with no preconditioning. When employing intermediate validation, the increase in E_R was smaller as compared to the unvalidated result. Given that the unvalidated E_R was nearly a value of one, the disproportionately small increase in E_R was understood to be a function of the upper limit of vector reliability for the VSJ#301. No appreciable sensitivity was observed for the different preconditioning methods, indicating a uniform quality between the displacement estimates.

Table 4.3. PIV Displacement Preconditioning Properties for VSJ#301

VSJ#301		(units)
Number of Correlation Passes	2	#
Window Size	64 x 64 , 32 x 32	pixels
Windowing Function (zero padded)	Gaussian	
Grid Resolution	8 x 8	pixels
Number of Validation Passes	2	#

Comparisons with published results of other PTV algorithms for the VSJ#301 are shown in Table 4.4. All published results were taken from the corresponding publications. The methods included in the comparison are: four-frame inline tracking (FIT) [7], binary cross-correlation (BCC) [13], original relaxation method (ORX) [21], new relaxation method (NRX) [20], variation tracking (VAR) [22], and enhanced particle tracking (EPTV) [23]. It should be noted that all these methods employ different validation or preconditioning procedures.

Without displacement preconditioning or validation (^{1}), the MP3-PTV algorithm outperforms all other methods except for EPTV, when comparing the overall performance using vector efficiency, $E_{F,}$ although E_R is less, this is compensated by significant increase in E_Y. Employing intermediate validation (^{2}), the MP3-PTV vector reliability, E_R, was now comparable with other methods and the E_F was 40.5% only marginally less than the EPTV method. Utilizing displacement preconditioning (^{3}) and intermediate validation (^{4}) further improved the performance of the MP3-PTV algorithm in comparison to other algorithms, resulting in the best overall efficiency of 45%. Errors in the velocity measurements were approximately equal to the previously reported position error, e_{xy} as it is determined by the accuracy of the subpixel estimation method. It was concluded that the main source of velocity error resulted from the measurement of the particle location. The previous works listed did not report errors for their velocity estimation so no direct comparisons were possible.

Table 4.4. Comparison of Published Results for the #301 VSJ Image Set

	D	N	V	E_Y	E_R	E_F	e_{uv} (pixels)	$e_{RMS,uv}$
FIT[a]	779	671	4042	19.3%	86.1%	16.6%		
FIT[b]	630	559	4042	15.6%	88.7%	13.8%		
BCC	860	788	4042	21.3%	91.6%	19.5%		
ORX	786	762	4042	19.4%	96.9%	18.9%		
NRX	808	788	4042	20.0%	97.5%	19.5%		
VAR	872	865	4042	21.6%	99.2%	21.4%		
EPTV	1759	1733	4042	43.5%	98.5%	42.9%		
NN-d-I (EDT-CLSG)[1]	1880	1227	4042	46.5%	65.3%	30.4%	0.08	0.13
NN-d-I (EDT-CLSG)[2]	1742	1637	4042	43.1%	94.0%	40.5%	0.09	0.14
NN-d-I (EDT-CLSG)[3]	1833	1777	4042	45.3%	96.9%	44.0%	0.09	0.14
NN-d-I (EDT-CLSG)[4]	1854	1821	4042	45.9%	98.2%	45.1%	0.09	0.13

[1] - no intermediate validation applied
[2] - four passes of intermediate validation
[3] - same as [1] with PIV-driven initialization
[4] - same as [2] with PIV-driven initialization
[a] - search radius ration of 0.2
[b] - search radius ratio of 0.1
D - # of measured vectors
N - # of correct vectors
K - # of known vectors

Benchmarking of MP3-PTV as a Multiphase Algorithm

A simulated data set was generated using an in-house algorithm to replicate a multiphase flow (MPF) having a bi-modal distribution of diameters. The MPF image generation was designed to replicate the imaging conditions of a multiphase flow experiment conducted by the authors and which will be presented in Section 5. The current section of the paper provides information regarding the generation of the MPF image set and subsequent performance of the MP3-PTV when employed on a simultaneously seeded multiphase turbulent flowfield. For the MPF image set, all reported values were averaged over 100 individual images, which assured statistical convergence was achieved.

Generation of the MPF Images

The MPF image set was generated based on the results of the rib-channel multiphase flow experiment (see Experimental Validation and Testing section). The experimental particle concentration and diameter distribution were utilized as inputs for generating each set of images. Particle identification and sizing were performed on the experimental images with both tracer particles only and sand particles only using the EDT and CLSG. For each identified particle in the experimental image, an identically sized particle was randomly placed within the simulated image with no constraints to keep individual particles separate from one other.

For each particle, the Fraunhofer diffraction pattern was represented by a Gaussian distribution, a common approximation when generating PIV images: The particle images include contributions from their diameter and relative distance to the focal plane center as well as effects related to the diffraction limited resolution of the camera/lens arrangement. This model, however, does not account for the interference of particle images produced from the complex wave function. To properly address this issue, the particle images were generated using the integrated form of the Gaussian intensity profile, as shown in Eq. 4,

$$I(x,y) = I_0 \frac{\pi d_p^{\,2}}{32}\left[\mathrm{erf}(\alpha) - \mathrm{erf}(\alpha)\cdot\mathrm{erf}(\beta) - \mathrm{erf}(\beta)\right]$$
$$\alpha = \sqrt{8}\left(x - x_i - 0.5\right)\Big/ d_p \qquad (4)$$
$$\beta = \sqrt{8}\left(y - y_i - 0.5\right)\Big/ d_p$$

where x_i and y_j denote the center particle location and I_0 represents the maximum pixel intensity. This integral form is a truer representation of the digital recording process as the sensors record the integrated light intensity over the individual pixels.

Image noise was added using the built-in MATLAB function “imnoise”. This command added Gaussian noise with a prescribed mean and variance across the entire image. Gaussian noise was added to represent the thermal noise that is common in CCD and CMOS cameras. The level of noise added to the MPF images was varied until a suitable correspondence to the experimental image intensity histogram was found.

Simulated particle displacement was controlled separately for the flow tracers and sand particles. Displacement of flow tracers was described by a Rankine vortex centered at x = 128 and y = 128 pixels, having a radius of 10 pixels and maximum velocity of 10 pixels per framestep. A uniform horizontal velocity of u = 5 pixels per framestep was applied to sand particles along with a randomly distributed vertical velocity ranging from v = ±5 pixels per framestep, representing ballistic particle trajectories unaffected by the motions of the carrier flowfield. The simulated MPF and experimental multiphase flow images are shown in Figure 4.7, along with the MPF displacement velocity fields. The combined MPF image is also shown in Figure 4.7.

To validate the MPF images, particle identification and sizing was performed using the EDT and CLSG. The measured size distribution of the MPF (not shown) matched closely with the size distribution of the original multiphase flow experimental images for all simulated image types (flow tracer, sand, and combined images).

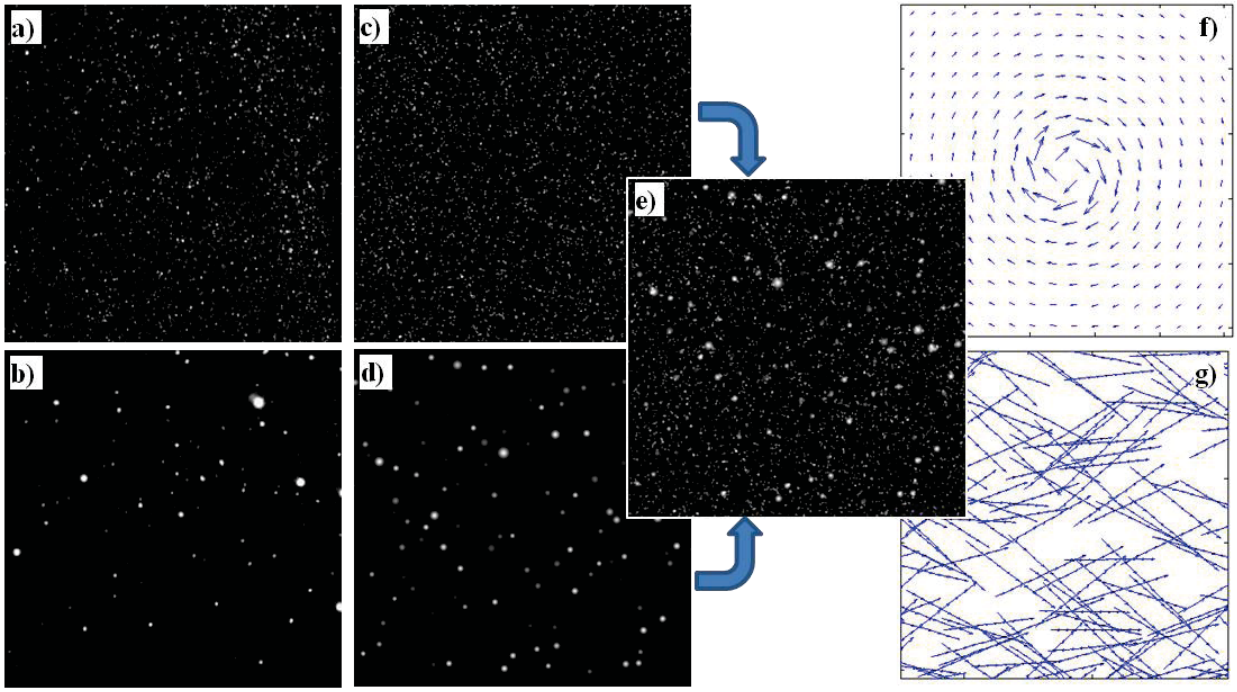

Figure 4.7. Sample experimental a) tracer and b) sand images with the corresponding simulated (MPF) images of c) tracer, d) sand and, e) combined along with the simulated displacements of f) tracer and g) sand particles.

Displacement Preconditioning Methods

Determining an appropriate particle displacement estimate for the MPF images is not straightforward given that two separate particles populations exist, each with their own relative motions. Two preconditioning methods were tested for this study; both based on a PIV correlation of the MPF images.

The first preconditioning method utilized the measured particle size information to segregate each MPF image, which was then reconstructed into two separate image sets each having only flow tracers or sand particles. Previously utilized techniques for segregating simultaneously seeded discrete multiphase flows include median spatial filtering [36] and phase-discrimination by size and measured object intensity [37]. These methods, while effective, did not address the issue of overlapping particles. The results of MP3-PTV segregation process are

shown in Figure 4.8, for a single image. Once separated, the flow tracers and sand particle images were processed independently using the RPC cross-correlation algorithm. This method provided a suitable displacement estimate for both particle populations, as shown Figure 4.9. It is important to note that this method is limited to situations when a suitable particle-related parameter (diameter, intensity, shape) exists to segregate the different populations.

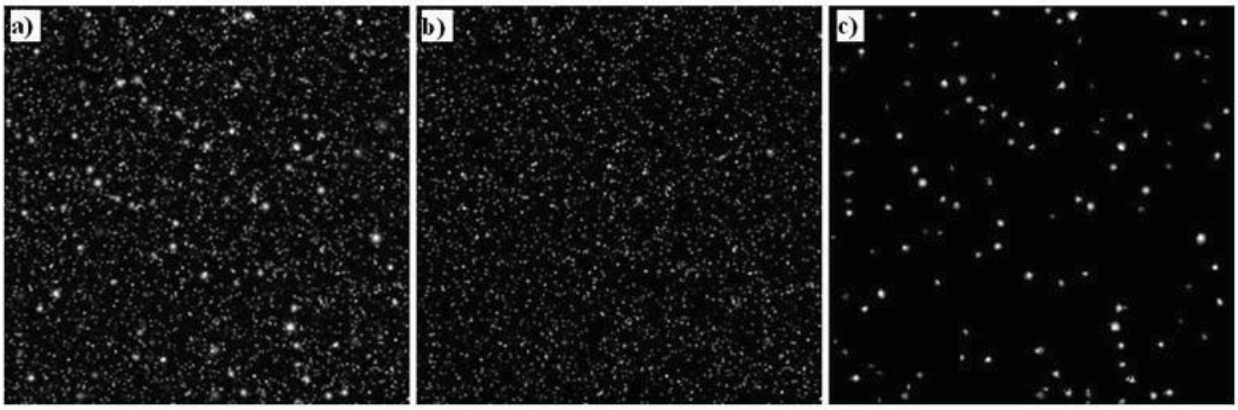

Figure 4.8. Results of the image segregation a) original MPF image b) separated flow tracers c) separated sand particles.

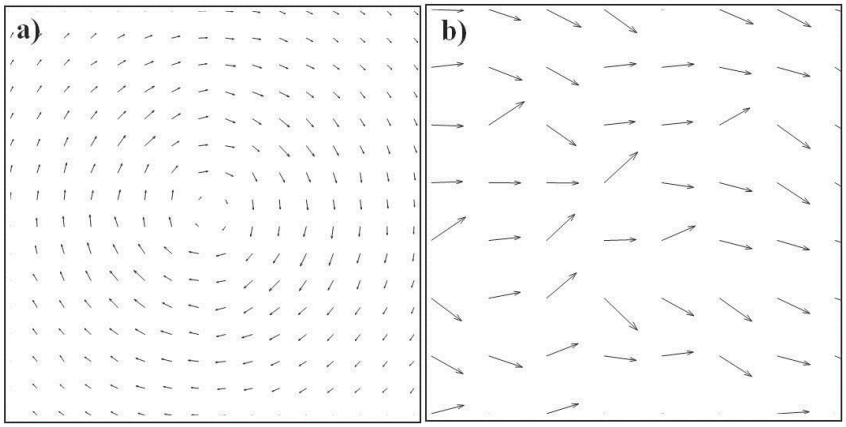

Figure 4.9. Displacement estimate using PIV between the first two MPF images without vector validation for a) separated flow tracers b) and separated sand particles.

The second method was to directly process the MPF images using the previously described RPC cross-correlation algorithm [28, 29]. The resulting vector field is shown in Figure 4.10a. The motions of the large sand particles strongly biased the velocity estimate in their local region. However, it was possible to identify and remove these biased measurements through post-validation of the particle velocities. The validated PIV vector field provided a

suitable displacement estimate of the flow tracers, as illustrated in Figure 4.10b, but no information with regard to the sand particle motions.

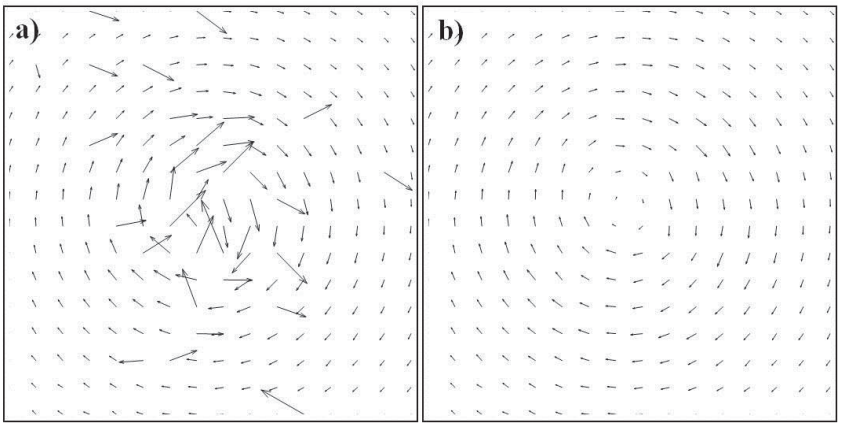

Figure 4.10. Displacement estimate using PIV between the first two MPF images a) without, b) and with vector validation.

Results for the In-House Generated MPF Set

Displacement Estimate from Segmented MPF Images

When the MPF images were segmented prior to computing a displacement estimate, an increase in vector reliability was observed for the MP3-PTV both with and without displacement preconditioning, as shown in Figure 4.11. The vector validation step was omitted, given the dissimilar motions of the two particle populations. Overall vector efficiency for the multi-component algorithm (NN-d-I) with preconditioning was 49% and 46% for the flow tracers and sand, respectively. These values represented a 9% and 44% increase in measured vector efficiency for tracers and sand populations as compared to the nearest-neighbor PIV-hybrid tracking algorithm. It is also important to note that the measured vector reliability of the separated tracers was 98% for the multi-component algorithm with preconditioning, verifying that the detrimental feedback between the two populations had been successfully negated through the particle segmenting process. Separating the populations also served to decrease the diameter range of the tracer population (d_{max}–d_{min}). Recalling equation (2), decreasing the diameter range subsequently increases the effectiveness of the diameter pair-matching parameter as compared to the original image with both sand and tracer particles.

The measured velocity error for the tracers and sand particles was approximately 0.1 pixels/framestep and 0.2 pixels/framestep, respectively. As compared to the mean particle

velocities, 2.2 pixels/framestep for the tracers and 8.1 pixels/framestep for the sand, this corresponded to a 4.5% and 2.5% error in measured velocity for the respective particle populations.

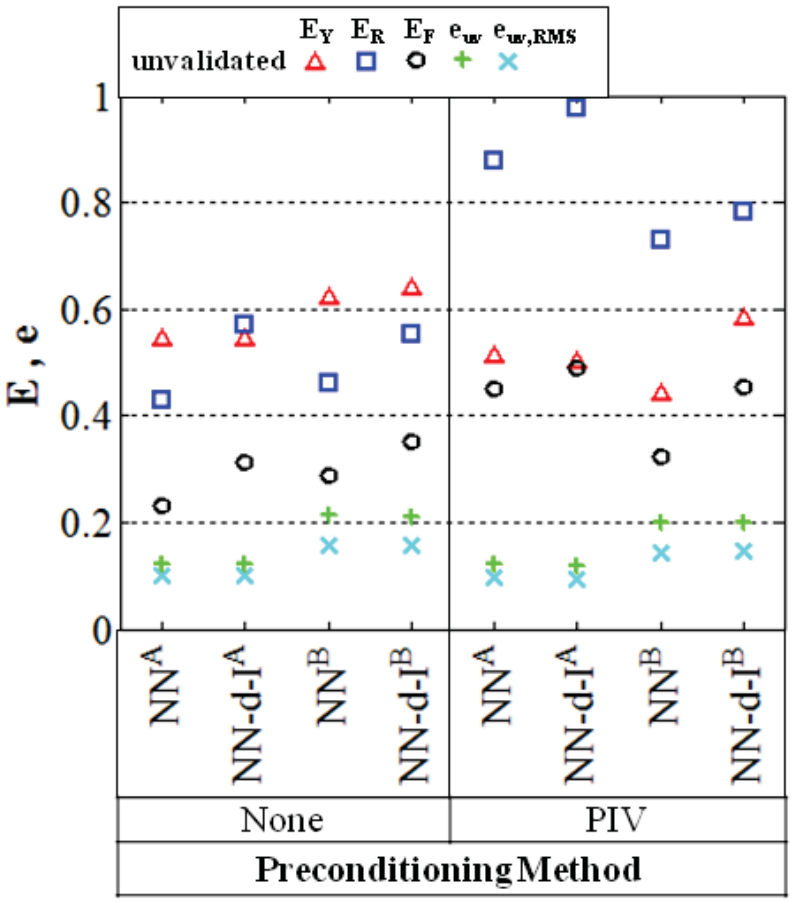

Figure 4.11. Performance of the MP3-PTV algorithm for the segmented MPF images, where "A" and "B" refer to the tracer and sand particles, respectively.

Displacement Estimate from Unsegmented MPF Images

The MP3-PTV performance on the original MPF image set without segregation is shown in Figure 4.12 for both tracer and sand particles. As with the analysis of the VSJ#301 and the segregated MPF images, the addition of multiple pair-matching parameters significantly increased velocity measurement reliability (E_R) both with and without displacement preconditioning. However, a significant drop in reliability was observed for the sand particles when employing the NN algorithm. Sans preconditioning, the overall efficiency for the sand dramatically dropped from 30% to 1% when comparing the segregated and original images.

With preconditioning, the efficiency increased to 9% for the NN, which was still much lower than the 36% efficiency reported for the separated sand particles. In contrast, the multiple pair-matching algorithm retained high levels of vector efficiency for the sand particles both with and without preconditioning.

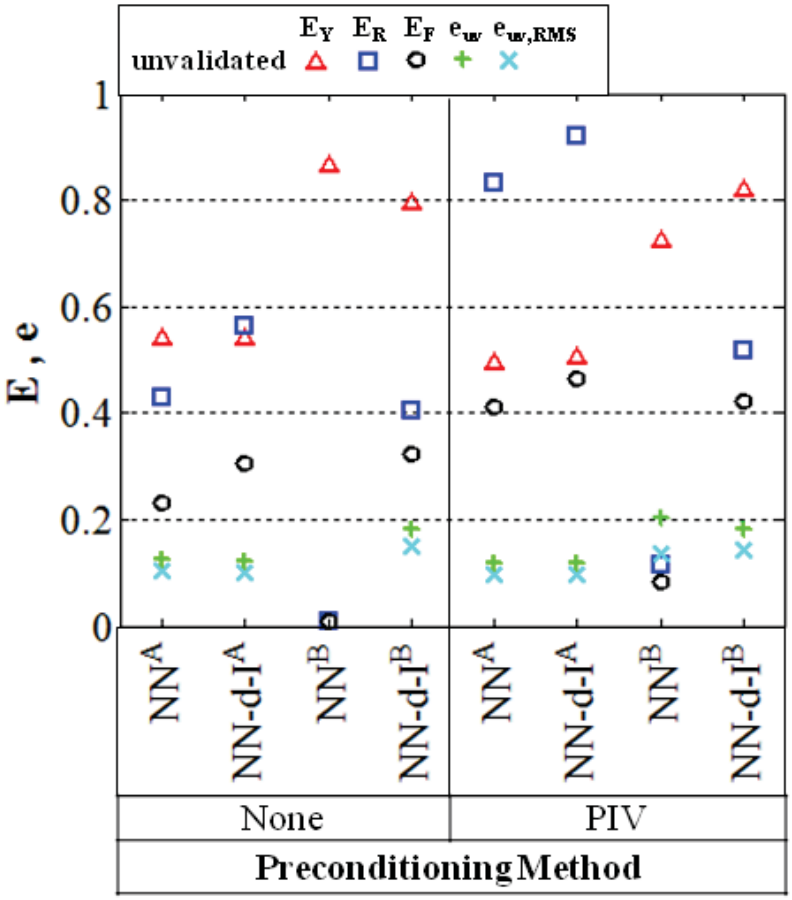

Figure 4.12. Performance of the MP3-PTV algorithm for the original MPF images, where "A" and "B" refer to the tracer and sand particles, respectively.

Experimental Validation and Testing

As referenced previously, a multiphase flow experiment was conducted to provide a baseline for generating the MPF image set. A description of the experimental setup is detailed in this section as well as the performance of the MP3-PTV for experimental data. Results for a single-phase flowfield are presented first followed by results for a simultaneously seeded multiphase flow.

Experimental Setup

The multiphase flow experiments were performed in a fully roughened channel having staggered rib arrays on two opposed walls. Flowfield measurements were achieved using an in-house developed Time-Resolved Digital Particle Image Velocimetry (TRDPIV) system and processing algorithm. An illustration of the test facility is shown in Figure 4.13. The channel Reynolds number was 10k, based on the hydraulic diameter and bulk streamwise velocity. The entrance to the rib-roughed channel region, shown in Figure 4.13, was chosen as the experimental measurement region.

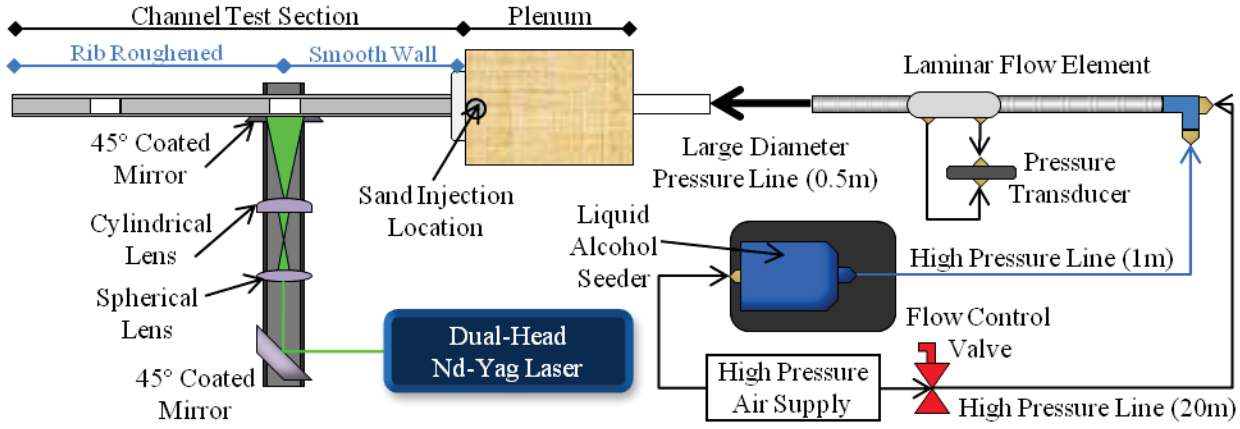

Figure 4.13. Rib channel facility used to acquire experimental multiphase flow images.

A 20W New Wave dual-head Pegasus laser was used to illuminate the flow, as shown in Figure 4.13. Imaging normal to the laser sheet, a 1-megapixel Photron Ultima APX-RS high speed digital camera recorded images of the flow at 3000 fps, corresponding to a 1.5 kHz sampling rate. The camera resolution was 1024x464 pixels resulting in an imaged resolution of 84.7 μm/pixel. Laser and camera settings were kept constant for all tests, thus assuring a consistent image quality for each case. All results presented were averaged over 100 image pairs.

The flowfield was seeded with both tracer and sand particles, resulting in a multiphase flow having a bi-modal distribution of diameters. Tracer seeding was accomplished using an alcohol based liquid atomizer producing ~1μm diameter droplets which were injected upstream of the LFE, as shown in Figure 4.13, to ensure a homogenous particles distribution. Arizona Road Dust (AzRD), a commonly used standardized test sand [38], was introduced upstream of the channel inlet from a sealed gravity feed system. The resulting particle size distributions are shown in Table 4.5. Also shown in Table 4.5 are the Stokes numbers of both the tracer and a sand particle, based on the rib height and bulk channel velocity. The relative differences in particle size and density allowed for a broad range of particle Stokes numbers.

Table 4.5. Particle Properties for the Multiphase Flow Experiment

	sand diameter - μm		
	d_m / St_m	d_{min} / St_{min}	d_{max} / St_{max}
Alcohol Tracers	1 / 0.001		
Sieved AzRD	193 / 1600	77 / 256	517 / 11,540

Performance on Single-Phase Rib-Channel Flow (Tracer Particles Only)

In this section, a comparison of the MP3-PTV to PIV processed results is provided for a rib-channel flow seeded only with tracer particles. The experimental images were processed with the MP3-PTV algorithm using EDT particle identification, CLSG particle sizing, and NN-d-I pair matching methods. PIV processing of the single-phase experimental images was also carried out with the RPC algorithm in a similar manner to the VSJ#301 (see Table 4.3) with three additional post-processing validation passes.

The MP3-PTV measured particle velocities for a single image pair are shown in Figure 4.14b, with the flow direction being from left to right and gray regions representing the rib locations. The PIV-derived velocity measurements are also shown in Figure 4.14a for the same image pair. The MP3-PTV measurement density was considerable higher than for PIV, with 22,065 and 6,853 measurements, respectively. Decreasing the PIV grid spacing to 4 x 4 pixels produced 27,051 measurements. This increase, however, occurred at a window overlap of ~90%, calling into question the independence of each vector. A grid spacing of 8 x 8 pixels, with a window overlap of 75%, can be acceptable given the high shear regions and turbulent nature of the flowfield although typically even less overlap is desired, hence PIV would yield an even smaller number of vectors.

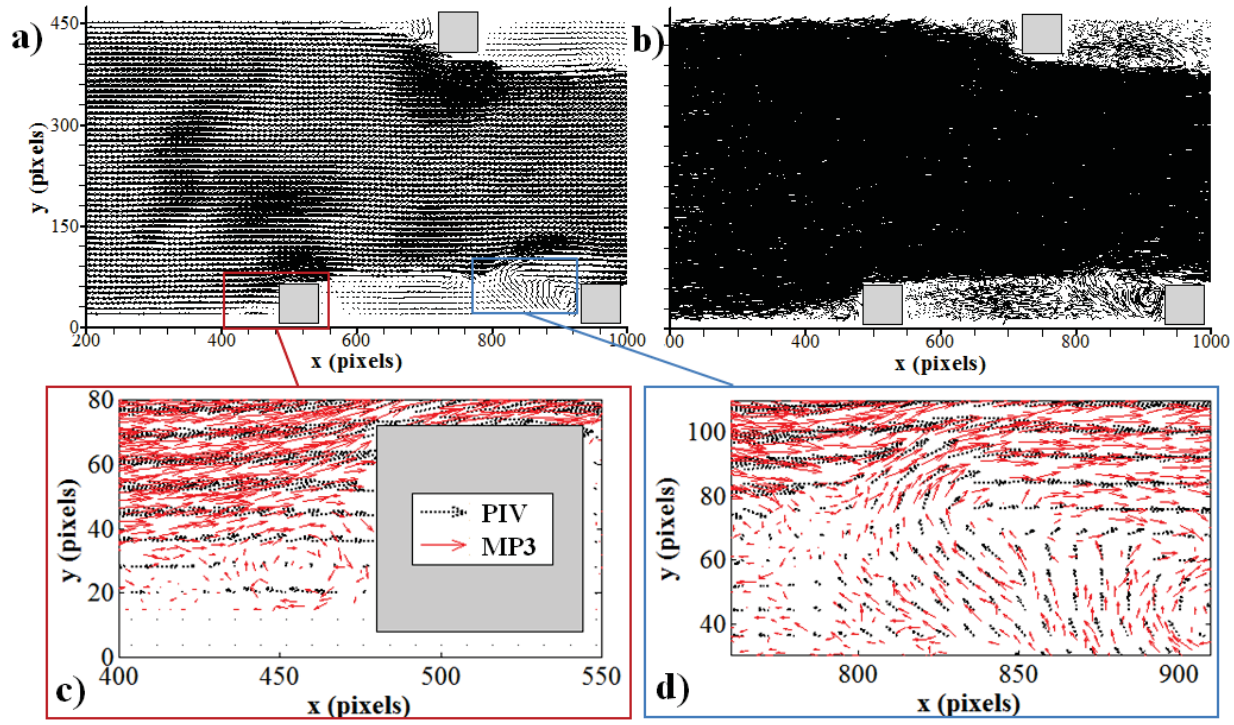

Figure 4.14. Measured velocity field for the experimental images using a) PIV and b) MP3-PTV along with zoomed regions c) and d) comparing PIV (black) and MP3-PTV (red) measured trajectories.

Overall the measured velocity fields were comparable, with similar flow structure and velocities exhibited for both the MP3-PTV and PIV. The absolute velocity difference between the two methods, $\Delta Vel_{PIV\text{-}MP3}$, is shown in Figure 4.15. Comparison of the randomly distributed MP3-PTV measurements and the gridded PIV measurements was accomplished through a bicubic spline interpolation. The mean difference in the velocity measurements was 0.48 pixels with a standard deviation of 0.41 pixels. From the cumulative histogram (Figure 4.15a) it was observed that over 90% of the MP3-PTV velocity measurements were within 1 pixel of the corresponding PIV measurement, indicating that the methods were in close agreement. In addition, a small biasing to integer velocity values was observed in the measured velocity differences, as illustrated in Figure 4.15b. The biasing resulted from the very small imaged tracer particle size which adversely affected the estimation of the particle's sub-pixel location, a phenomenon often referred to as peak locking. Also observed was a strong correlation between the pair-matching coefficient, C_{12}, and the velocity difference between the MP3-PTV and PIV, further confirming the effectiveness of C_{12} as a vector validation parameter.

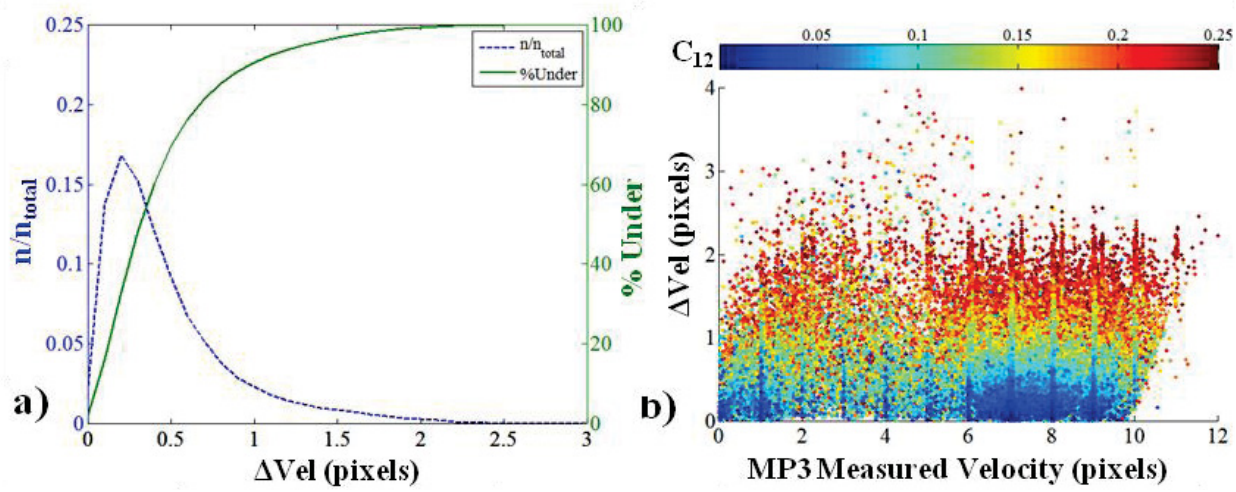

Figure 4.15. a) Histogram and b) scatter plot of the difference in PIV and MP3-PTV velocity measurements.

Performance on Multiphase Rib-Channel Flow (Tracer and Sand Particles)

In this section, results are provided for a rib-channel flow simultaneously seeded with both tracers and sand particles. All images initially underwent a background subtraction, which was equal to the minimum intensity value registered for each pixel over all images within a single test case. This image pre-processing step assured a uniform background level and also equilibrated any intensity variation between the laser pulses. The experimental images were then processed with the MP3-PTV algorithm using EDT particle identification and CLSG particle sizing. After segregating the two particle populations by size (Figure 4.16), as previously described for the MPF image set, the NN-d-I pair matching algorithm was used to measure tracer and sand particle velocities. Given that the motions of both particle populations were simultaneously resolved, the instantaneous slip velocities of the sand particles could be measured directly through a distance-weighted spatial average of the neighboring tracer velocities (see Eq. 1).

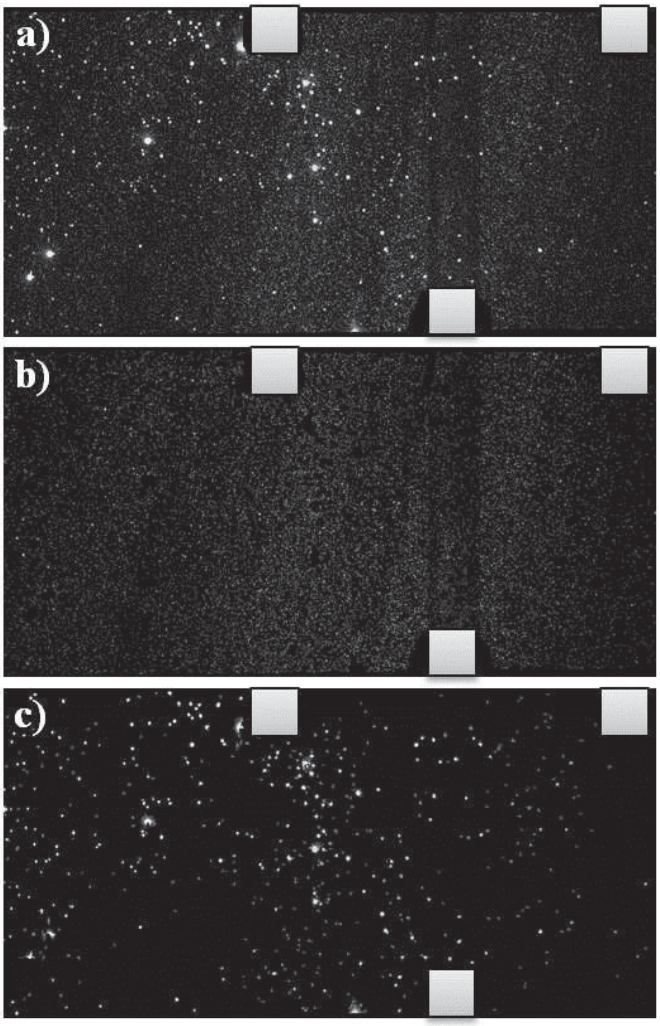

Figure 4.16. Simultaneously seeded experimental image a) original b) separated tracers c) separated sand.

Normalized histograms of the measured slip velocities of the sand particles are shown in Figure 4.17. Given the unsteady and turbulent nature of the rib-channel flow and the high Stokes number of the sand particles, the broad distribution of slip velocities measured was not unexpected. The average particle slip velocity, however, was still ~50% of the bulk velocity indicating that the sand particle trajectories were not completely ballistic.

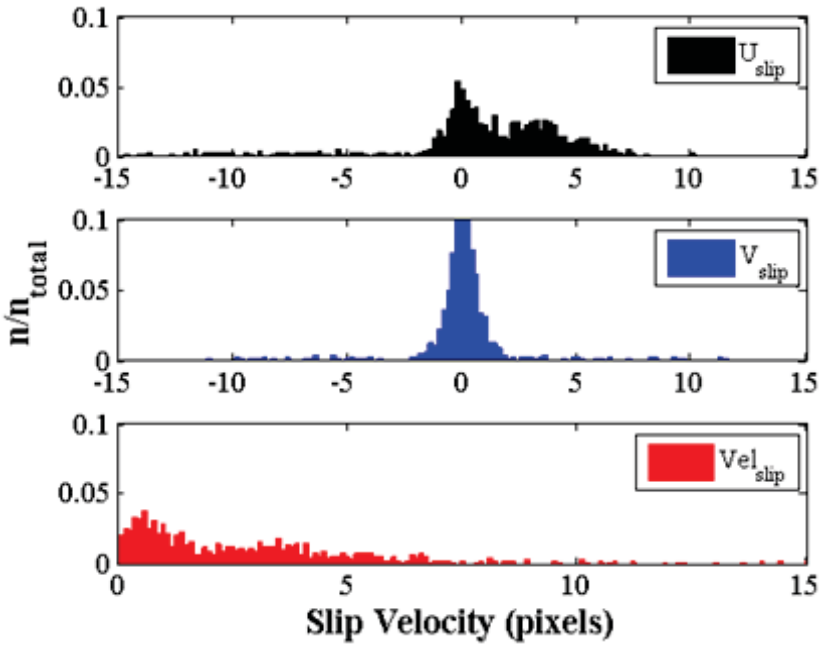

Figure 4.17. Histogram of particle slip velocities of the sand particles as compared to the simultaneously resolved tracer particle velocities.

Conclusions

Systematic testing of the MP3-PTV algorithm on a multitude of data sets illustrated the benefits of combining additional pair-matching parameters, such as diameter and maximum intensity, with traditional PTV. The contribution of each step in the MP3-PTV was also individually evaluated with attention paid to performance and error of the velocity measurements.

Regarding particle identification and segmentation, the presented erosion/dilation threshold (EDT) outperformed the single value threshold (SVT) by a factor of two or more. For the VSJ#301 image set, processing with the EDT resulted in the highest number of correctly identified and segmented particles compared to all other published results.

Of the six sizing methods evaluated, the continuous least squares Gaussian (CLSG) resulted in the most robust estimate of particle centroid, diameter, and true intensity. Identifying particles with the EDT reduced the error of all sizing methods, especially for the intensity weighted centroid (IWC), which was the most computationally efficient method.

Providing a displacement estimate for the particles increased vector reliability. For a single population of particles (i.e. single-phase flow), all evaluated estimation methods performed similarly indicating that the accuracy of the preconditioning method was more important than its application. For a multiphase flowfield, the MP3-PTV method out-performed traditional and hybrid PTV, especially when processing unsegregated images.

Application of the MP3-PTV algorithm on real-world experimental images illustrated the capability of the aforementioned methods to handle both typical and a-typical image conditions. Most importantly, the effectiveness of the MP3-PTV was demonstrated on a simultaneously seeded multiphase flow having a dilute solid-gas mixture of sand particles and dry air. Therein lies the main strength of utilizing the MP3-PTV algorithm, which facilitates the time-resolved measurement of slip velocities and instantaneous Stokes numbers either with or without segregation and separation of the particle populations.

Nomenclature

General

A_p particle area

C_{12} particle matching coefficient

d particle diameter

D number of measured vectors

e_{xy} average position error,

$$e_{xy} = \frac{1}{n_I}\sqrt{\left(x_m(i) - x_a\right)^2 + \left(y_m(i) - y_a\right)^2}$$

$e_{RMS,xy}$ root mean square deviation of position error,

$$e_{RMS,xy} = \sqrt{\frac{1}{n_I}\sum_{i=1}^{n_I}\left(e_{xy}(i) - e_{xy}\right)^2}$$

e_{uv} average vector error,

$$e_{uv} = \frac{1}{N}\sum_{i=1}^{N}\sqrt{\left(u_m(i) - u_a\right)^2 + \left(v_m(i) - v_a\right)^2}$$

$e_{RMS,uv}$ root mean square deviation of vector error,

$$e_{RMS,uv} = \sqrt{\frac{1}{N}\sum_{i=1}^{N}\left(e_{uv}(i) - e_{uv}\right)^2}$$

E_Y vector yield, $E_Y = D / V$

E_R vector reliability, $E_R = N / D$

E_F measurement efficiency, $E_F = E_Y \times E_R$

I pixel intensity value

I_{th} intensity threshold level

n_I number of identified particles

n_k number of known particles

n_S number of sized particles

N number of correct vectors

r_S search radius

U_{slip}, V_{slip}, slip velocity, $U_{slip} = u_{sand} - u_{tracer}$, $V_{slip} = v_{sand} - v_{tracer}$,

Vel_{slip}	resultant slip velocity $Vel_{slip} = \sqrt{U_{slip}^2 + V_{slip}^2}$
V	number of known vectors
W_d, W_I, W_R	pair-matching parameter weights
u, v	velocity variables
x, y	spatial variables

Greek

σ	population standard deviation
ΔVel	velocity difference, $\Delta Vel = \left\lvert \left(\sqrt{u^2 + v^2}\right)_{PIV} - \left(\sqrt{u^2 + v^2}\right)_{MP3} \right\rvert$

Identification Methods

SVT	single value threshold
EDT	erosion/dilation threshold

Sizing Methods

IWC	intensity weighted centroid
TPG	three point Gaussian
FPG	four point Gaussian
CFPG	continuous four point Gaussian
LSG	least squares Gaussian
CLSG	continuous least squares Gaussian

Tracking Methods

NN	single component – nearest neighbor
NN-d	two component – NN and particle diameter
NN-I	two component – NN and max intensity
NN-d-I	three component – NN, particle diameter, and max intensity

References

1. Bachalo, W.D., 1994, "Experimental Methods in Multiphase Flows," International Journal of Multiphase Flow. 20: p. 261-295.
2. Bachalo, W.D. and Houser, M.J., 1984, "Phase Doppler Spray Analyzer for Simultaneous Measurements of Drop Size and Velocity Distributions," Optical Engineering. 23(5): p. 583-590.
3. Nishino, K., et al., 2000, "Stereo imaging for simultaneous measurement of size and velocity of particles in dispersed two-phase flow," Measurement Science & Technology. 11(6): p. 633-645.
4. Black, D.L., et al., 1996, "Laser-based techniques for particle-size measurement: A review of sizing methods and their industrial applications," Progress in Energy and Combustion Science. 22(3): p. 267-306.
5. Jones, A.R., 1999, "Light scattering for particle characterization," Progress in Energy and Combustion Science. 25(1): p. 1-53.
6. Hassan, Y.A., et al., 1992, "Piv Flow Visualization Using Particle Tracking Techniques," Measurement Science & Technology. 3(7): p. 633-642.
7. Hassan, Y.A. and Canaan, R.E., 1991, "Full-field bubbly flow velocity measurements using a multiframe particle tracking technique," Experiments in Fluids. 12: p. 49-60.
8. Adrian, R.J., 2005, "Twenty years of particle image velocimetry," Experiments in Fluids. 39(2): p. 159-169.
9. Westerweel, J., 1997, "Fundamentals of digital particle image velocimetry," Measurement Science & Technology. 8(12): p. 1379-1392.
10. Willert, C.E. and Gharib, M., 1991, "Digital particle image velocimetry," Experiments in Fluids. 10(4): p. 181-193.
11. Kobayashi, T., et al., 1989, "Developemnt of a Real-Time Velocity Measurement System for Two-Dimensional Flow Fields Using a Digital Image Processing Technique," Trans. of JSME (B). 55(509): p. 107.
12. Uemura, T., et al., 1989, "A high speed algorithm of image analysis for real time measurement of two-dimensional velocity distribution," ASME FED-85: p. 129-134.
13. Yamamoto, F., et al., 1993, "Three-Dimensional PTV Based on Binary Cross-Correlation Method," JSME International Journal. 36(2): p. 279-284.
14. Baek, S.J. and Lee, S.J., 1996, "A new two-frame particle tracking algorithm using match probability," Experiments in Fluids. 22: p. 23-32.
15. Wernet, M.P. 1993, "Fuzzy logic particle-tracking velocimetry. " in Proc. of SPIE. San Diego, CA.
16. Cowen, E.A. and Monismith, S.G., 1997, "A hybrid digital particle tracking velocimetry technique," Experiments in Fluids. 22: p. 199-211.
17. Keane, R.D., et al., 1995, "Super-resolution particle imaging velocimetry," Measurement Science and Technology. 6: p. 754-768.
18. Takehara, K., et al., 2000, "A Kalman tracker for super-resolution PIV," Experiments in Fluids. [Suppl.]: p. S34-S41.
19. Kim, H.B. and Lee, S.J., 2002, "Performance improvements of two-frame particle tracking velocimetry using a hybrid adaptive scheme," Measurement Science and Technology. 13: p. 573-582.

20. Ohmi, K. and Li, H., 2000, "Particle-tracking velocimetry with new algorithms," Measurement Science and Technology. 11: p. 603-616.
21. Ohmi, K. and Lam, D.H. 1998, "New particle tracking PIV using an improved relaxation method. " in Proc. 8th International Symposium on Flow Visualization.
22. Ruhnau, P., et al., 2005, "A variational approach for particle tracking velocimetry," Measurement Science and Technology. 16: p. 1449-1458.
23. Mikheev, A.V. and Zubtsov, V.M., 2008, "Enhanced particle-tracking velocimetry (EPTV) with a combined two-component pair-matching algorithm," Measurement Science and Technology. 19: p. 1-16.
24. Brady, M.R., et al., 2009, "Methods for Digital Particle Image Sizing (DPIS): Comparisons and Improvements," Flow Measurement and Instrumentation: p. doi:10.1016/j.flowmeasinst.2009.08.001.
25. Takehara, K. and Etoh, T., 1998, "A Study on Particle Identification in PTV Particle Mask Correlation Method," Journal of Visualization. 1(3): p. 313-323.
26. Marxen, M., et al., 2000, "Comparison of Gaussian particle center estimators and the achievable measurement density for particle tracking velocimetry," Experiments in Fluids. 29: p. 145-153.
27. Adrian, R.J. and Yao, C.-S., 1985, "Pulsed laser technique application to liquid and gaseous flows and the scattering power of seed materials," Appl. Opt. 24(1): p. 44-52.
28. Eckstein, A. and Vlachos, P.P., 2009, "Digital particle image velocimetry (DPIV) robust phase correlation," Measurement Science and Technology. 20(5): p. 055401.
29. Eckstein, A. and Vlachos, P.P., 2009, "Assessment of advanced windowing techniques for digital particle image velocimetry (DPIV)," Measurement Science and Technology. 20(7): p. 075402.
30. Nogueira, J., et al., 1997, "Data validation, false vectors correction and derived magnitudes calculation on PIV data," Measurement Science and Technology. 8: p. 1493-1501.
31. Pun, C.S., et al., 2007, "Mode-ratio bootstrapping method for PIV outlier correction," Measurement Science and Technology`. 18: p. 3511-3522.
32. Westerweel, J., 1994, "Efficient detection of spurious vectors in particle image velocimetry," Experiments in Fluids. 16: p. 236-247.
33. Westerweel, J. and Scarano, F., 2005, "Universal outlier detection for PIV data," Experiments in Fluids. 39: p. 1096-1100.
34. Okamoto, K., et al., 2000, "Evaluation of the 3D-PIV Standard Images (PIV-STD Project)," Journal of Visualization. 3(2): p. 115-123.
35. Okamoto, K., et al., 2000, "Standard images for particle-image velocimetry," Measurement Science and Technology. 11: p. 685-691.
36. Kiger, K.T. and Pan, C., 2000, "PIV Technique for the Simultaneous Measurement of Dilute Two-Phase Flows," Journal of Fluids Engineering. 122(4): p. 811-818.
37. Khalitov, D.A. and Longmire, E.K., 2002, "Simultaneous two-phase PIV by two-parameter phase discrimination," Experiments in Fluids. 32(2): p. 252-268.
38. ISO12103-1, Road vehicles -- Test dust for filter evaluation -- Part 1: Arizona test dust. 1997: Geneve, Switzerland.

Summary of Findings and Future Recommendations

The study of dispersed two-phase flows for both scientific and industrial applications has considerable interest to the many fields. The presence of foreign debris within a gas turbine cooling system, an example of a dispersed two-phase flow, was the primary focus of this research with an emphasis on resolving both the fluid flow and particle trajectories.

In the first paper, the effects of sand flowing through a combined impingement and film-cooling double wall liner were presented for four realistic liner geometries. The pressure ratio across the liner, sand amount, metal temperature, and sand temperature were investigated under ambient and engine representative temperatures. At both ambient and heated conditions, the liner with the largest impingement flow area and least overlap between the impingement and film-cooling holes exhibited the lowest relative blocking. It was determined that the impingement holes were acting as a particle size filter for the film-cooling plate. In addition, the cooling liners with staggered film and impingement holes were found to be less sensitive to sand depositing on the upstream side of the film-cooling plate, which occurred at higher temperatures. Lastly, it was hypothesized that impingement could be used to breakup larger particles thereby reducing their possibility of blocking within subsequent cooling geometries. This method to breakup of particles by impingement was investigated in a separate study by Land et al. [1] and shown to be very effective for the reduction of blockage.

An experimental study on a rib-channel flowfield was conducted for the second paper to verify the TRDPIV method for both single phase and two-phase flows. The main tasks of this study were to benchmark the TRDPIV against other published studies and to provide qualitative insight into the trajectories of sand particles within the channel. The TRDPIV method agreed well with previously published studies using Laser Doppler Velocimetry (LDV) and Large Eddy Simulation (LES) on similar rib-channel flowfields. Regarding the particle trajectories, there was a preferential concentration of wall impacts at the upstream rib surface with more wall impacts being observed as particle size increased. This resulted in a particle rebounding process whereby larger particles traveled in a direction opposite to the mean flow direction, sometimes for several rib pitches. Breakup of particle agglomerations was frequently observed during wall collisions, resulting in a decreasing Stokes number as the smaller diameter particles traveled through the channel. Overall, the observed particle trajectories did not completely concur with

those derived by LES simulations on a two-phase ribbed channel flow. This work indicates the need for a more complete study combining observed experimental findings with improved modeling.

For the third paper, an in-depth TRDPIV study was conducted on the effects Reynolds number and channel location on for a single-phase rib-channel flowfield. Observations of the mean-averaged flowfield showed that the near wall flow was dominated by the separated flows over the ribs. At the channel inlet, a strong dependence to Reynolds number was observed. Within the developed region, the flowfield was less sensitive to changes in the Reynolds number. Measurement of the coherent structures present in the flowfield showed a preferential concentration within the separated mixing layer generated by the ribs at the inlet. The distribution of coherent structures, in contrast, was more homogeneous within the developed region. High strength coherent structures, having been shed by previous upstream ribs, were observed to persist within the bulk channel flow. Turbulence dissipation rate was also estimated from the TRDPIV resolved flowfields, thus providing a baseline of comparison for future computations studies on an oft-investigated internal flowfield.

In the final paper, a method for identifying and tracking particles was presented having the capability to resolve both the fluid and particulate phases. This unique algorithm employed a pair-matching algorithm which utilized displacement preconditioning, particle size, and particle intensity for matching particle pairs between successive images. A new particle identification and segmentation routine was also developed to improve the tracking performance. The new algorithms were validated on both simulated and experimental images, including a published data set specifically designed to test particle tracking algorithms. The presented segmentation and tracking methods were shown to outperform all other published methods, with a significant increase in identified particles and correctly matched particle tracks. When dealing with a two-phase flow situation, the new algorithms effectively segregated the two particle populations and reported a vector efficiency and measurement error equivalent to the results for a single-phase flow. This illustrated the algorithm's capability to robustly and accurately track particles under a variety traditional and nontraditional image conditions.

Recommendations for Future Work

This dissertation, as previously summarized, provides a number of scientific findings related to the fluid and particle dynamics within the turbine cooling system. The measurement methodologies and algorithms have all been successfully validated and implemented on a variety of experimental and simulated data sets. As such, an optimal starting point is provided for any number of studies regarding the ingestion of foreign debris into gas turbine engines as well as any generic study of a dispersed multi-phase flow.

Regarding the particle convection within the turbine cooling system, a comprehensive study of particle trajectories is suggested for a range of particle types and cooling geometries. The main focus of this proposed study will center on the comparison of the measured trajectories with motions predicted using the Basset, Boussinesq and Oseen equation (BBO). In addition to the particle convection, special attention should be paid to particle collisions with the internal surfaces. The quantification of preferential concentrations and collision rates will allow for predictions of surface erosion and deposition.

The investigation of ingested debris need not be confined to the turbine cooling system. The presence of particles within the main gas path results in a number of negative effects, such as the erosion of aerodynamic surfaces and high temperature surface deposition both within and downstream of the combustor. With the appropriate equipment and access to an actual turbine engine, the presented methodologies could be adapted to facilitate ***in situ*** measurement of fluid and particle velocities, an impressive study indeed!

Outside of the gas turbine research community, there is considerable interest in the study of dispersed two-phase flows for any number scientific and industrial applications. Biomedical engineers are investigating the effects of foreign particle inhalation [2], specifically how particle size affects deposition within the lungs. High speed two-phase flow is also of interest to aerospace engineers developing robust ignition and flameout resistant SCRAMJET combustors [3]. Environmental engineers are currently developing tools to predict atmospheric dust and pollutant transport [4]. Despite a broad applicability, there is currently a lack of understanding regarding particle transport in turbulent multi-phase flows.

References

1 Land, C., Thole, K. A., Joe, C., “Investigation of Sand Blocking within Impingement and Film-Cooling Holes,” accepted for publication in the Journal of Turbomachinery.

2 Phalen, R.F., 2008, Inhalation Studies: Foundations and Techniques, Informa Healthcare USA, Inc., New York, NY.

3 Fletcher, E.A., 2007, “Scramjets and Surfboards: Some Forgotten History,” Journal of Propulsion and Power, Vol. 23, No. 1, pp. 15-20.

4 Jickells, T.D., An, Z.S., Andersen, K.K., Baker, A.R., Bergametti, G., Brooks, N., Cao, J.J., Boyd, P.W., Duce, R.A., Hunter, K.A., Kawahata, H., Kubilay, N., Laroche, J., Liss, P.S., Mahowald, N., Prospero, J.M., Ridgwell, A.J., Tegen, I., Torres, R., 2005, "Global Iron Connections between Desert Dust, Ocean Biogeochemistry, and Climate," Science, Vol. 308, No. 5718, pp. 67-71.